MBE Growth of GaAs Nanowires and Nanowire Heterostructures

Dissertation
to obtain the Doctoral Degree of Science
(Dr. rer. nat.)
from the Faculty of Physics
of the University of Regensburg

presented by
Andreas Rudolph
from Garmisch-Partenkirchen

2012

This thesis was supervised by Prof. Dr. Werner Wegscheider, Prof. Dr. Dominique Bougeard and Dr. Elisabeth Reiger.
The thesis was submitted on 19.06.2012. The colloquium was held on 19.07.2012.

Examination board:

Chairman:	Prof. Dr. Jaroslav Fabian
First Reviewer:	Prof. Dr. Werner Wegscheider
Second Reviewer:	Prof. Dr. Dominique Bougeard
Additional surveyor:	Prof. Dr. Dieter Weiss

Contents

Chapter 1

Introduction

During the last century scientific knowledge has increased exponentially. One of the most important inventions was the bipolar junction transistor by John Bardeen, Walter Brattain and William Shockley at Bell Labs in 1947. The discovery initiated a rapid development in the field of microelectronics. This technology has an enormous impact on our modern society and revolutionized our way of life. First and foremost it changes the way we acquire and use information. Through personal computers and the Internet nearly any kind of information is accessible at any time and any place. The effect of this development is not limited to information technology. Medical applications, especially the new imaging techniques like computer tomography and magnetic resonance tomography or modern drug design are unthinkable without this invention. Also our modern transport systems strongly rely on microchips. Airplanes are full of microelectronics, train schedules are optimized using computer systems and any car has dozens or hundreds of micro controllers for engine control, safety systems etc.

The enormous success of microelectronics is dedicated to one fundamental property of microelectronic devices: Scalability. Scalability means that the size of devices like transistors can be reduced without losing their functional properties. As a consequence, more and more transistors can be integrated on a single chip. In 1968 Gordon E. Moore [67] predicted that the number of transistors on an integrated circuit doubles every 12 months. The time frame was expanded to 24 months in 1975 (cf. figure 1.1). Since that, major semiconductor companies like Intel are using Moore's prediction as reference point for their road maps, thereby turning Moore's prediction into Moore's law. For more than 40 years, this law was valid and may stay valid for the years to come. However, at a certain point downscaling will reach physical limitations. Actual problems like the huge heat generation of microchips with more than 100 million transistors can be overcome by reducing the operation

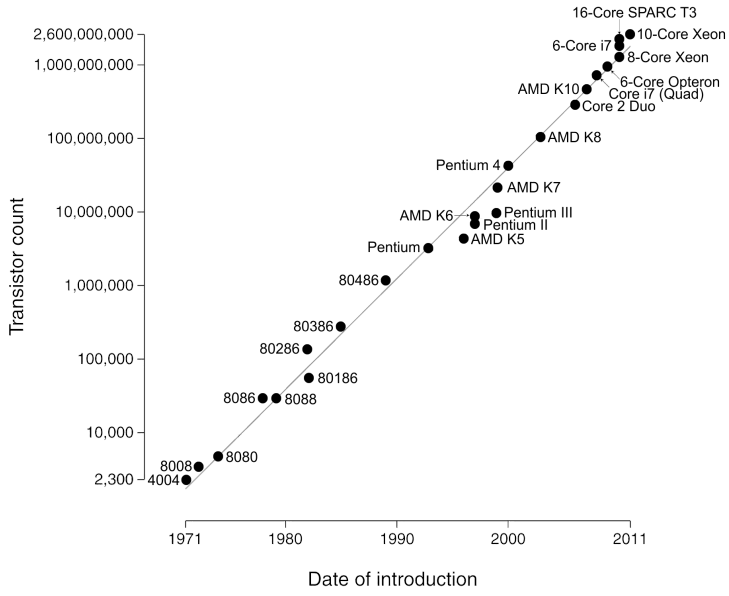

Figure 1.1: Moores's Law from 1971 to 2011. The labels next to the dashed line are CPUs of Intel and AMD. The transistor count doubles every two years. Taken from [116].

voltage and thereby the power consumption. The final frontier is reached when the width of the tracks reaches the dimensions of the coherence length of the charge carriers. Then quantum effects will play a major role and the functionality of the device can no longer be guaranteed.

This development implies the necessity of finding new approaches for future electronics. One promising idea is to take advantage of the quantum effects instead off treating them as a problem. Classical computers work with a binary system where every bit has two well defined states, referred to as 0 and 1. A quantum bit, short qbit, can additionally adopt a third state, which is a superposition of the two states 0 and 1 [102]. Using qbits, algorithms can be applied that solve fundamental computational problems, like the factorization of integer numbers in prime numbers, on polynomial instead of exponential timescales [94]. Despite the fact that a lot of effort is put on this subject and some progress was made in the past few years [109], quantum computing will need some decades before it is ready for the market. In the meantime, other solutions have to be found to fill the gap between the era of classical, silicon based computing and the quantum age.

Spintronic and vertical integration are two possible stopgaps. Spintronic is composed from the words "Spin" and "Electronic". In Spintronics the focus of interest

is shifted from the charge of the electron, which plays the major role in conventional electronics, to its spin [30]. A prominent spin effect is the giant magnetoresistance effect (GMR), which was discovered by Peter Grünberg and independently by Albert Fert in 1988. The effect can be observed in thin multilayer structures, where ferromagnetic and non magnetic layers are alternating. Depending on the magnetization of the adjacent ferromagnetic layer, the resistance is different for the parallel and the anti parallel configuration. Since 1997 the GMR is used for the fabrication of hard disc driver read heads, leading to a dramatic increase in storage density. Both scientists were awarded with the Nobel Price in 2007.

Besides its application in hard disk drivers, spintronic concepts are developed for other semiconductor devices. In 1990 the concept of a spin transistor was proposed by Datta and Das [11]. This concept is very promising with respect to the heat problem of conventional transistors, because a spin current can flow without a charge current [47, 101]. Unfortunately the realization of this concept is very challenging. One major problem is the spin injection into the semiconductor. The spin transistor of Datta and Das was originally proposed with iron contacts. Since semiconductors have a much smaller carrier density than ferromagnetic metals, their resistance is some orders of magnitude larger than that of the ferromagnetic metals. As a consequence, the spin injection efficiency, which is proportional to the ratio of metal and semiconductor resistance, is very small for this type of contacts [31]. This problem is known as the conductivity mismatch problem [92].

One possibility to avoid this problem is to replace the metal contacts with ferromagnetic semiconductor contacts. Ferromagnetic semiconductors like europium chalcogenides [54, 65] or semiconducting spinels [79, 110] have been studied since the late sixties. The research interest in this first generation of ferromagnetic semiconductor decreased since the eighties. The reasons are difficulties in growing single crystalline samples and low ferromagnetic transition temperatures, which made the material systems inappropriate for room temperature applications [30]. Additional problems with respect to the integration of ferromagnetic semiconductors on silicon or III-V semiconductors arise from the huge lattice mismatch of the different material systems. As a consequence, the interface quality between a ferromagnetic and a non magnetic semiconductor is often very poor and the large number of crystal defects, which acts as scattering centers, inhibit an effective spin injection into the non magnetic semiconductor [108].

Fortunately there is a smart way to circumvent the two major problems, conductivity and lattice mismatch using the concept of diluted magnetic semiconductors (DMS). This second generation of ferromagnetic semiconductors is based on nonmagnetic semiconductors which are alloyed with magnetic elements [30]. In 1998 Ohno [75]

applied this concept to the III-V material system Gallium-Arsenide (GaAs), using Manganese (Mn) as magnetic dopant. At that time, GaAs was already a well established semiconductor system. The fundamental work was done by Arthur [1] and Foxon [32, 33] in the late sixties and seventies. The advantage of GaAs is its high electron mobility, making it suitable for high frequency applications and thereby interesting for the integration on silicon (Si) [61]. Considering all these facts, the material system of GaAs/GaMnAs seems to offer a variety of possibilities for future spintronic applications.

Besides spintronic also vertical integration offers a promising approach for the improvement of electronics. Nowadays integrated circuits are fabricated by optical lithography and wet chemical etching. This fabrication technique limits the available space for device components to a two dimensional plane. The idea of vertical integration is to stack and connect these planes in order to increase the total number of device components. First attempts were made by a group of the Fraunhofer-Institut in 2003, which tried to connect the vertical aligned circuit boards at predefined positions using some kind of conductive paste. A much more sophisticated method for vertical integration is the use of semiconductor nanowires (NWs). NWs are quasi one dimensional structures with a huge length to diameter ratio. NWs can be fabricated from the same material than the original substrate (e.g. Si or GaAs), which eliminates the risk of contamination with foreign materials. In addition, not only connections between two circuit boards could be realized, even electronic devices like transistors could be fabricated with NWs [6, 7, 106]. Although the problem of connecting the tip of the NW to the second circuit board is not yet solved, NWs are the most promising approach for vertical integration.

The aim of this thesis is to combine the concepts of spintronics and vertical integration, i.e. to fabricate ferromagnetic GaAs/GaMnAs core shell NWs. In the first part of this PhD thesis the growth of GaAs NWs on GaAs substrates with molecular beam epitaxy is investigated. For the study of the NW morphology and crystal structure, the Au catalyzed growth technique is used. Here, the GaAs substrate is covered with a thin Au layer. After oxide desorption, the Au layer comes in contact with the GaAs substrate and Au/Ga droplets are formed, which act as catalyst for NW growth. To obtain a uniform morphology and crystal structure for all NWs on one sample, the Au/Ga ratio in the catalyst droplets has to be the same for all NWs. Therefore, identical Au discs at equal distances were fabricated on a GaAs substrate. The equal distance ensures that the incoming material from the effusion cells is equally distributed under all NWs.

In the second part of this PhD thesis, the growth of GaAs NWs on untreated and pre-structured GaAs and Si substrates covered by a thin SiO_2 layer is examined.

For the growth on pre-structured SiO_2 layers, the Ga catalyzed growth technique is used. Here, holes in a grid like pattern are fabricated on the SiO_2 layer with e-beam lithography and wet chemical etching. The holes provide nucleation sites for Ga droplets, which work as catalyst during NW growth.
In the third part of this PhD thesis, the growth of GaAs/GaMnAs core shell NWs and their structural and magnetic properties are examined. First, the growth of GaMnAs on (110) oriented GaAs substrates is optimized because (110) is the predominant crystal orientation of the NW side facets. After adapting the growth parameters to the growth conditions on the NW side facets, GaAs/GaMnAs core shell NWs with pure zinc blende, a mixed wurtzite/zinc blende and pure wurtzite crystal structure are grown. The structural properties of the NWs are investigated with transmission electron microscopy (TEM). The magnetic properties of NW ensembles are examined with superconducting quantum interference device (SQUID) measurements and the magnetic properties of single NWs are investigated with magnetotransport measurements.
The thesis is structured as follows. After the introduction, chapter 2 deals with the theory of NW growth and magnetism. In chapter 3 the sample fabrication and characterization techniques are explained. In chapters 4 and 5 the results obtained with the Au and the Ga catalyzed growth technique will be presented. Chapter 6 deals with the growth and characterization of GaAs/GaMnAs core shell heterostructures. In chapter 7 the results are summarized and an outlook is given in chapter 8.

Chapter 2

Basics

The following chapter is a brief introduction in the theory of molecular beam epitaxy (MBE) and magnetism. First, the relevant thermodynamic quantities of MBE will be presented. These quantities will be used to explain the growth of nanowires (NWs), taking into account the special boundary conditions which arise from the NW growth mode. Then the basic concepts of magnetism will be introduced, followed by an explanation of the ferromagnetic phase transition and the magnetic anisotropies of GaMnAs. Finally, we review the state of the art in the field of magnetic and non magnetic NWs at the time I started my thesis.

2.1 MBE growth

In the first section, terms like the Gibbs free energy and the chemical potential are introduced to explain the phase transition of the involved material in MBE. Here, we follow the considerations of Ref. [107]. In the second section, this concept is applied to the growth of NWs.

2.1.1 Thermodynamic fundamentals

The growth of crystals by molecular beam epitaxy means, from a thermodynamic point of view, the condensation of evaporated material on a substrate which is equivalent to a phase transformation of the material from the vapor to the solid phase. If we want to understand this process, we have to answer two fundamental questions.
The first question is: why does the phase transformation occur? The answer to this question is quite simple: the systems, which includes the material in the vapor and the solid phase as well as the substrate, tries to reach its equilibrium state. This is

equivalent to a minimization of the systems energy. Here we have to clarify what the term "system" means and what the "energy" of the system, from a thermodynamic point of view, actually is. We can distinguish between "open" and "closed" systems. A closed system is separated from its environment. The energy of a closed system is called internal energy. According to the first law of thermodynamics, the change in internal energy is equivalent to the heat added to the system minus the work done by the system. An open system can exchange one or more quantities with its environment. According to which quantities are exchanged, it is characterized by a different "free" energy. In case of MBE, the system exchanges material and entropy with its environment. During the growth process, temperature and pressure are typically constant. Therefore we have to add two correction terms to the internal energy, one for the constant temperature and one for the constant pressure. The energy of this open system is called the Gibbs free energy.
The second question refers to the driving force of this phase transition. The driving force is simply the difference of the Gibbs free energy or, what is physically equivalent, the difference of the chemical potential, between the current and the equilibrium state.
We can express this mathematically as follows. The Gibbs free energy can be written as:

$$G^{\alpha}(p,T,N_a) = H^{\alpha}(p,T,N_a) - TS^{\alpha}(p,T,N_a) \tag{2.1}$$

The first term is the enthalpy, which is the free energy at constant pressure

$$H^{\alpha}(p,T,N_a) = U^{\alpha}(p,T,N_a) - pV^{\alpha}(p,T,N_a) \tag{2.2}$$

The second term is the constant temperature correction. Here, α denotes the phase and N_a is the number of moles of a component a. From the Gibbs free energy of phase α we can derive the chemical potential of component a in phase α

$$\mu_a^{\alpha}(p,T,) = \frac{\partial G^{\alpha}(p,T,N_a)}{\partial N_a} \tag{2.3}$$

In the case of MBE, we deal with at least two phases (the vapor and the solid phase) and normally with two or more components (like Ga and As). For such a system, the total Gibbs free energy can be written as

$$G^{tot} = G^{\alpha}(p,T,N_a,N_b) + G^{\beta}(p,T,N_a,N_b) \tag{2.4}$$

To reach its equilibrium state, the total Gibbs free energy of this system has to be minimized with respect to the transfer of atoms from one phase to the other. The

change in the total Gibbs free energy should vanish if N_a^α is increased while N_a^β is decreased and the overall number of a atoms is constant.

$$\frac{\partial G^{tot}}{\partial N_a^\alpha} = \frac{\partial G^\alpha}{\partial N_a^\alpha} + \frac{\partial G^\beta}{\partial N_a^\alpha} = \frac{\partial G^\alpha}{\partial N_a^\alpha} - \frac{\partial G^\beta}{\partial N_a^\beta} = \mu_a^\alpha - \mu_a^\beta = 0 \tag{2.5}$$

The same assumption should be valid for N_b

$$\frac{\partial G^{tot}}{\partial N_b^\alpha} = \frac{\partial G^\alpha}{\partial N_b^\alpha} + \frac{\partial G^\beta}{\partial N_b^\alpha} = \frac{\partial G^\alpha}{\partial N_b^\alpha} - \frac{\partial G^\beta}{\partial N_b^\beta} = \mu_b^\alpha - \mu_b^\beta = 0 \tag{2.6}$$

We can conclude that the system is in equilibrium when the chemical potentials of component a and b equal each other in phase α and β. If they do not, the system is not in equilibrium and the difference in the chemical potentials of the two phases will act as driving force for the transfer of atoms between them.

2.1.2 NW growth model

Since the theory of NW growth is quite new and was modified several times to accommodate for the latest experimental results, a short review will be given to show how the growth model evolved from the beginning to the current version. The theory of NW growth was developed to large parts by the groups of V.G. Dubrovskii and F. Glas [16–26, 36–38, 95]. Starting in 2004, Dubrovskii tried to explain his observations, e.g. the dependence of the NW growth rate on the NW radius [26], by expanding the growth model of Givargizov and Chernov [35]. Due to the fact that this model just accounts for the Gibbs-Thomson (GT) effect and the direct collection of impinging material by the droplet, it could, when related to the growth of GaAs NWs, at first just explain the result achieved at very Ga-rich growth conditions, where the droplet is highly supersaturated and the diffusion contributions to the NW growth rate are negligible. In 2005 an extended growth model included the Ga diffusion from the substrate to the tip of the NW [16]. Besides the group of V.G. Dubrovskii, the group of F. Glas was working on a nucleation theory to explain the appearance of wurtzite and zinc blende crystal structure in NWs [37]. In 2008, both groups joined forces and combined the theories of diffusion and nucleation [23]. This publication will be used for the following section. In 2009, Dubrovskii completed his theoretical work by introducing a term which accounts for the Ga diffusion from the NW side facets to the NW tip [22]. Due to the fact that the Ga diffusion length on the side facets is very large at our growth conditions, this term does not affect the growth kinetic and can be neglected. In 2010, Glas showed that the group V element is the crucial species in the nucleation process. We will refer to this result at the appropriate place.

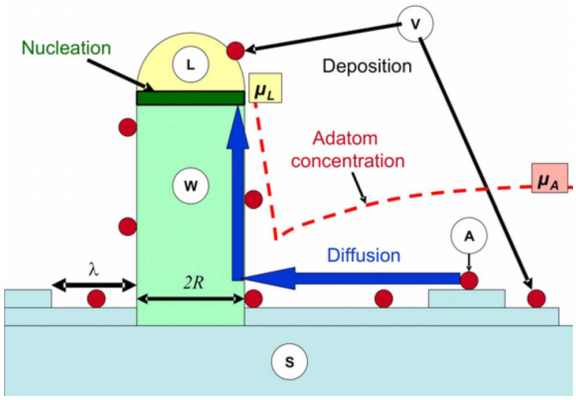

Figure 2.1: Vapor-liquid-solid (VLS) model of NW growth. The atoms from the vapor phase either hit the droplet directly or they impinge on the substrate and diffuse via the side facets to the droplet. The dotted line shows the adatom concentration profile with $\mu_A > \mu_L$. Taken from [23].

Now we will apply the concept of the chemical potentials to the growth of NWs. We have to consider five phases of the semiconductor material: the vapor (V) with chemical potential μ_V, the substrate (S) with chemical potential μ_S, adatoms (A) with chemical potential μ_A, the liquid droplet (L) with chemical potential μ_L, and the NW (W) with chemical potential μ_W. We assume that the material, which is evaporated from the effusion cells, reaches the liquid droplet of the NW on two ways. The first way is the direct impinging of material on the droplet, the second way is the diffusion of the material from the substrate over the side facets to the tip of the NW. The material is incorporated in the NW on the droplet-NW boundary. The model is illustrated in figure 2.1.

To enable the growth of NWs, some basic inequalities have to be satisfied. First, the chemical potential of the vapor phase has to be larger than the chemical potential of the adatoms, $\mu_V > \mu_A$, and the liquid droplet, $\mu_V > \mu_L$, otherwise the material would be re-evaporated from the substrate and the droplet. Second, the chemical potential of the adatoms has to be larger than the chemical potential of the liquid droplet, $\mu_A > \mu_L$, otherwise the diffusion of the adatoms will be directed from the droplet to the surface, which is contradicting to NW growth. These inequalities can be written as $\Delta\mu_{VS} > \Delta\mu_{AS}$, $\Delta\mu_{VS} > \Delta\mu_{LS}$ and $\Delta\mu_{AS} > \Delta\mu_{LS}$ by defining the substrate as reference point. In the following we will examine these inequalities a little closer to get a better understanding of the underlying physics.

We start with the determination of the fact that $\Delta\mu_{VS} > \Delta\mu_{AS}$ at common growth conditions. The reason for the reduced chemical potential of the material in the adatom phase compared to the vapor phase is caused by the nucleation of adatoms at the surface. The difference in chemical potential between the adatoms far away

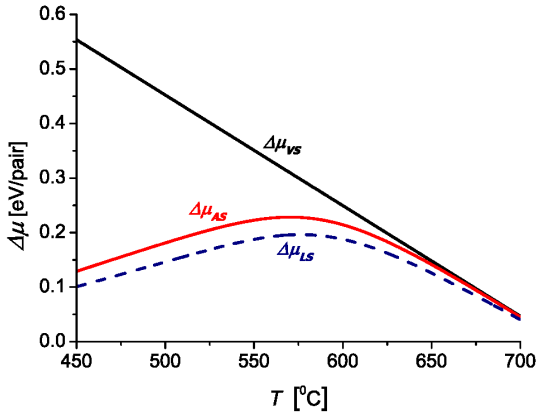

Figure 2.2: Dependence of $\Delta\mu_{VS}$ and $\Delta\mu_{AS}$ on the temperature at a fixed growth rate of 0.6 ML/s. Taken from [23].

from the NW and the substrate is

$$\Delta\mu_{AS} = \mu_A^{\infty} - \mu_S = \Delta\mu_{VS} - 2k_BT\ln\left(\frac{\lambda_0}{\lambda}\right) \tag{2.7}$$

Here, k_B is the Boltzmann constant, T is the temperature of the adatoms, λ is the effective diffusion length when NW growth occurs while λ_0 is the diffusion length at equilibrium conditions (this implies $\lambda \leq \lambda_0$). The term $\Delta\mu_{VS}$ is the difference of chemical potential between the vapor and the substrate and can be written as:

$$\Delta\mu_{VS} = \mu_V - \mu_S = k_BT\ln\left(\frac{V}{V_0^S}\right) \tag{2.8}$$

V is the deposition rate in nm/s and V_0^S is the equilibrium deposition rate at which the deposition equals the desorption from the substrate [16].
Plotting the potentials of $\Delta\mu_{VS}$ and $\Delta\mu_{AS}$ versus the temperature will give us a first insight to the vapor-liquid-solid (VLS) growth mechanism. For the calculation of figure 2.2, MBE parameters for GaAs NWs on (111)B oriented GaAs substrates were used. Atomic Ga and dimer As_2 at a III/V ratio of 3 and a Ga temperature of 550°C were assumed. For further details of the calculation see Ref. [15, 23, 24].
As can be seen from figure 2.2, $\Delta\mu_{VS}$ decreases linearly with temperature. For high temperatures, the growth rate of the substrate tends to zero due to the high reevaporation rate of the impinging material fluxes and decomposition of the crystal. This is equivalent to a convergence of λ to λ_0 and as a consequence the chemical potential of $\Delta\mu_{AS}$ approaches $\Delta\mu_{VS}$. At low temperatures, $\Delta\mu_{AS}$ is smaller than $\Delta\mu_{VS}$ because the effective diffusion length λ is limited by the surface nucleation,

which generally increases with decreasing temperature. We will refer to these results when discussing the temperature dependence of the growth rate at the end of this section.
Next we examine the second inequality, $\Delta\mu_{AS} > \Delta\mu_{LS}$, with respect to the Gibbs-Thomson (GT) effect. The GT effect relates the surface curvature of a droplet to its chemical potential. As a consequence, the chemical potential of a small droplet is elevated, since its surface is large compared to its volume. Therefore we write:

$$\mu_L = \mu_L^\infty + \frac{2\Omega_L \gamma_{LV}}{R_L} \tag{2.9}$$

with γ_{LV} as the liquid-vapor surface energy, Ω_L as the elementary volume in the liquid phase, $R_L = R/\sin\beta$ as the droplet radius and β as the contact angle between NW and droplet [17,34,58]. Using equation 2.7 for $\Delta\mu_{AS}$, the condition for diffusion induced growth with $\Delta\mu_{LS}^\infty = \mu_L^\infty - \mu_S$ can be written as:

$$\Delta\mu_{LS}^\infty < \Delta\mu_{VS} - 2k_B T \ln\left(\frac{\lambda_0}{\lambda}\right) - \frac{2\Omega_L \gamma_{LV} \sin\beta}{R} \tag{2.10}$$

Comparing these results with our first inequality, $\Delta\mu_{LS} < \Delta\mu_{LV}$, we derived two correction terms. One has its origin in the surface nucleation of adatoms, which lowers μ_A^∞ with respect to μ_V (second term of equation 2.10), the other is caused by the GT effect (third term of equation 2.10). This result is crucial for the understanding of the underlying physics, because the terms $\Delta\mu_{LS}^\infty$ and $\Delta\mu_{VS}$ play an important role in the diffusion induced growth model.
Before we start with the calculation of the NW growth rate as a function of the chemical potentials, we make some assumptions to simplify the problem. We consider a prismatical or cylindrical shape of the NWs with a constant NW radius R. The NW radius should equal the radius of the droplet R_L, so that the contact angle β is close to 90°. We assume that all atoms, which arrive at the NW foot, are transferred to the top:

$$\Delta\mu_{AS}(r = R) = \Delta\mu_{LS} = \Delta\mu_{LS}^\infty + \frac{2\Omega_L \gamma_{LV} \sin\beta}{R} \tag{2.11}$$

We ignore the direct impingement, the desorption and the nucleation of atoms on the NW side facets. The adatoms on the substrate can be treated as a diluted gas, so we use the expression

$$\Delta\mu_{AS}(r) = k_B T \ln\left(\frac{n(r)}{n_{eq}}\right) \tag{2.12}$$

where $n_{eq} = J_0^s \tau_0 = (V_0^s/\Omega_s)\tau_0$ is the equilibrium adatom concentration and τ_0 is the mean lifetime of an adatom on the bare substrate [57].

Now we start the calculations of the diffusion induced growth model by using the steady state diffusion equation, which describes the adatom concentration on the substrate:

$$D\Delta n + J - \frac{n}{\tau} = 0 \tag{2.13}$$

D is the diffusion coefficient, $J = V/\Omega_S$ is the impinging flux (Ω_S is the elementary volume in the zinc blende phase), n is the adatom concentration on the substrate surface and τ is the effective lifetime on the substrate surface such that $\lambda = \sqrt{D\tau}$. The solution to equation 2.13 is given by:

$$n(r) = J\tau + CK_0(r/\lambda) \tag{2.14}$$

where C is a constant and K_0 is the modified Bessel function of the second kind. The equation satisfies the boundary condition $n(r) \to 0$ at $r \to \infty$. The adatom concentration at the foot of the NW, $n(R)$, can be expressed by using the simplifications of equation 2.12 in equation 2.11.

$$n(R) = n_{eq} \exp\left(\frac{\Delta\mu_{LS}^{\infty}}{k_B T} + \frac{R_{GT}}{R}\right) \tag{2.15}$$

where $R_{GT} = \frac{2\gamma_{LV}\Omega_L \sin\beta}{k_B T}$ is the characteristic radius describing the GT effect in the droplet. We equalize the values of n(R) from equation 2.14 and 2.15 to get an expression for n(r) as a function of the chemical potentials.

$$\frac{n(r)}{J\tau} = 1 - \left[1 - \exp\left(\frac{\Delta\mu_{LS}^{\infty} - \Delta\mu_{AS}}{k_B T} + \frac{R_{GT}}{R}\right)\right] \frac{K_0(r/\lambda)}{K_0(R/\lambda)} \tag{2.16}$$

The differential equation for the diffusion flux to the base of the NW, which is, according to our simplification, equivalent to the diffusion flux to the droplet, can be expressed by:

$$j_{Diff} = 2\pi R D \left.\frac{dn}{dr}\right|_{r=R} \tag{2.17}$$

We use equation 2.16 in 2.17 and divide the result by $\pi R^2/\Omega_S$. Thus we get the diffusion induced contribution to the NW growth rate

$$\left(\frac{dL}{dt}\right) = V\left[1 - \exp\left(\frac{\Delta\mu_{LS}^{\infty} - \Delta\mu_{AS}}{k_B T} + \frac{R_{GT}}{R}\right)\right] \frac{2\lambda}{R} \frac{K_1(R/\lambda)}{K_0(R/\lambda)} \tag{2.18}$$

where K_1 is the modified Bessel function of the second kind of first order. Next we will determine the contribution to the NW growth rate, which originates from the

direct impinging of atoms on the droplet. For a molecular beam, that is directed strictly perpendicular to the substrate surface, we find

$$\left(\frac{\pi R^2}{\Omega_S}\right)\left(\frac{dL}{dt}\right) = \pi R_L^2 (J - J_{des}^L) \tag{2.19}$$

J is the impinging flux on the droplet while J_{des}^L accounts for the desorption flux from the droplet. For the adsorption of the impinging atoms, the chemical potential between the vapor and the droplet has to be positive, then $J = J_\infty^L \exp(\Delta\mu_{VL}^\infty / k_B T)$ with $\Delta\mu_{VL}^\infty = \Delta\mu_{VS} - \Delta\mu_{LS}^\infty$. The desorption rate of the droplet increases with the curvature of it surface as $J_{des}^L = J_\infty^L \exp(R_{GT}/R)$. Using this result with equation 2.19, we get the contribution of the direct impinging atoms to the NW growth rate

$$\left(\frac{dL}{dt}\right)_{A-D} = \frac{V}{\sin\beta^2}\left[1 - \exp\left(\frac{\Delta\mu_{LS}^\infty - \Delta\mu_{VS}}{k_B T} + \frac{R_{GT}}{R}\right)\right] \tag{2.20}$$

A-D stands for adsorption-desorption. The total NW growth rate is the sum of the two contributions given in equation 2.18 and 2.20 minus the growth rate on the substrate surface. One should be aware that the two dimensional growth on the substrate buries the lower part of the NW and thereby reduces the NW length. Our final equation, which describes the total NW growth rate, is given by

$$\begin{aligned}\frac{1}{V}\left(\frac{dL}{dt}\right) = &\left[1 - \exp\left(\frac{\Delta\mu_{LS}^\infty - \Delta\mu_{VS}}{k_B T} + \frac{R_{GT}}{R}\right)\right] \\ &\times \left[\frac{1}{\sin^2\beta}\exp\left(\frac{\Delta\mu_{AS} - \Delta\mu_{VS}}{k_B T}\right) + \frac{2\lambda}{R}\frac{K_1(R/\lambda)}{K_0(R/\lambda)}\right]\end{aligned} \tag{2.21}$$

This equation enables us to draw some general conclusions concerning the NW growth kinetics. First, we see that the NW growth rate becomes zero at a minimum NW radius, $R_{min} = (2\gamma_{VL}\Omega_L \sin\beta)/(\Delta\mu_{AS} - \Delta\mu_{LS}^\infty)$ when the adsorption and the diffusion contribution disappears. This is due to the GT effect, which elevates the chemical potential of the liquid droplet to the chemical potential of the substrate and the vapor. As a consequence, the driving force for the diffusion flux from the substrate and the adsorption from the vapor disappears and the NW growth is stopped.

Second, the NW growth rate as a function of the NW radius has one maximum, which is in agreement with experiments [34]. The dependence of the NW growth rate on the NW radius for Au assisted MBE growth of GaAs NWs is shown in figure 2.3 (a).

The parameters for the calculation are taken from [23, 59, 121]. For small NW radii, the growth rate is mainly determined by the GT effect, which elevates the chemical

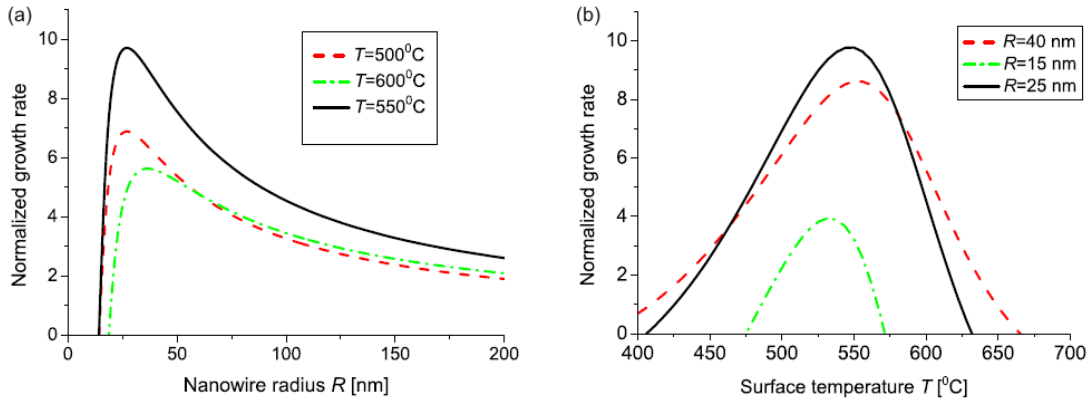

Figure 2.3: (a) Dependence of the normalized NW growth rate on the NW radius for three different temperatures. (b) Dependence of the normalized NW growth rate on the surface temperature for three different NW radii. Taken from [23].

potential of the droplet and thereby reduces the driving force for the material transport from the substrate to the tip of the NW. As a consequence, dL/dt increases with R. At a certain point, dL/dt reaches a maximum. Here we have an optimal ratio of the GT effect and the adatom diffusion contribution. On the one hand, the GT effect is large enough to extend the difference in chemical potential between the droplet and the NW to a point, which allows a fast incorporation of the material from the liquid in the solid phase. On the other hand, the GT effect is small enough to ensure a considerable diffusion flux from the substrate to the droplet. As a consequence, the NW growth rate decreases for further increasing R because the difference in chemical potentials between the droplet and the NW decreases.

Third, as can be deduced from figure 2.3 (b) the dependence of the NW growth rate on the temperature is also a function with one maximum. This observation, which is in agreement with the results of [24, 42, 81, 105], is attributed to the non monotonous behavior of $\Delta\mu_{AS}$ (cf. figure 2.2). The obtained temperature window is close to the experimentally observed values [42], which range from 400°C to 620°C. The growth window is narrow for small NW radii, where also the growth rate is reduced, and increases with increasing R.

2.1.3 NW crystal phase selection

After deriving and discussing the equation for the NW growth rate, we focus on the phase selection in GaAs NWs. In principle, GaAs can adopt two different crystal structures. In bulk material and layer structures, only the zinc blende (ZB) crystal

phase is found due to a 24 meV lower cohesive energy per III-V pair compared to the wurtzite (WZ) phase [120]. This energetic advantage can be canceled by the differences in the number of dangling bonds (4/3 bonds per layer for ZB and 1 bond per layer for WZ). Dangling bonds are not saturated bonds at the surface of the crystal. They play a central role in the case of NWs, because the NW surface to volume ratio is very large. As a consequence, the formation of WZ crystal structure is often observed in NWs. It should be noted that these considerations presume that the crystal structure is controlled only by thermodynamic processes. However, the newer NW nucleation theory predicts that this is not the case and the phase selection is determined mainly by the growth kinetics, e.g. by the differences in chemical potentials. The explanation given above should be taken as a first step toward this topic. For a more precise description we have to examine the nucleation process in detail.

Due to the fact that the cross section of the NW is typically very small, the nucleation process can be assumed to be mononuclear. This means that just one nucleus is formed on the top of a completed monolayer, which acts as starting point for the nucleation of the next monolayer. The nucleation process is assumed to occur in two steps [38]. The first step, in which the nucleus island is formed and the monolayer is completed, is very fast. The second step, which accounts for the time period between two nucleation events, takes much longer. The NW growth rate is therefore determined by the second nucleation step. The physical origin of this behavior can be found for the case of GaAs NWs in the low solubility of As in the Au/Ga droplet. During the nucleation process of one monolayer, the whole amount of As in the droplet is consumed. The waiting time between the nucleation events is needed to refill the droplet with As. As a consequence, the nucleation events are anti-correlated in time, i.e. the probability for a nucleation event is very low if another nucleation event occurred just a short time ago. This effect is known as the nucleation anti bunching effect [38].

The nucleation can occur on two different positions of the droplet-NW boundary. The first nucleation site is the center of the droplet-NW boundary, the second nucleation site is the triple line. The nucleation site may have an influence on the crystal structure. Figure 2.4 shows the two cases schematically.

If we assume that the pressure of the liquid droplet stays constant during the nucleation process, the free enthalpy is the quantity that describes the droplet-island system. Now we have to consider the factors, which change the free enthalpy of the droplet-island system. We find that

$$\Delta G_{wire} = -(\mu_L^{\infty} - \mu_W^{\infty})i + \Gamma_l P h + \gamma_{LV} \Delta S_L \tag{2.22}$$

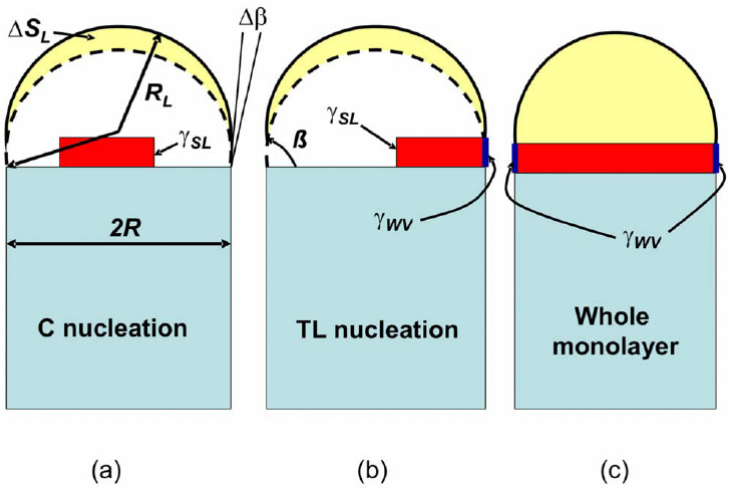

Figure 2.4: (a) The nucleation at the center line, (b) the nucleation at the triple line and (c) of the whole monolayer. Taken from [23].

The first term describes the decrease in chemical potential of i semiconductor particles during the transfer from the liquid to the solid phase. This term does not contain the GT correction, which is comprised in the second term. The second term accounts for the formation of the lateral surface Ph of the nucleus island. The island surface energy $\Gamma_l = (1-x)\gamma_{SL} + x\gamma_{WV}$ depends on the position of the island [37]. γ_{SL} is the liquid-solid surface energy, γ_{WV} is the wire-vapor surface energy and x is the fraction of the island perimeter at the triple line. It should be noted that the values of μ_W^∞, γ_{WV} and Γ_l depend on the crystal structure of the NW. The third term is dedicated to the transformation of the droplet surface ΔS_L due to the island formation. After some straight forward calculations, we find for the change of the droplet surface in case of center (left equation) and whole monolayer (right equation) nucleation:

$$\Delta S_L = \frac{2\sin\beta}{R}(\Omega_S - \Omega_L)i; \qquad \Delta S_L = -\sin\beta\frac{\Omega_L}{\Omega_s}2\pi Rh \tag{2.23}$$

The nucleation on the triple line is the general case and the change of the droplet surface can be written as combination of the two terms derived above:

$$\Delta S_L = \frac{2\sin\beta}{R}(\Omega_S - \Omega_L)i - \sin\beta\frac{\Omega_L}{\Omega_s}xRh \tag{2.24}$$

We only have to replace 2π by x, because the nucleation on the TL only eliminates a part of the vapor-liquid boundary. Using equation 2.24 in equation 2.22, we get the general expression for the change in free enthalpy:

$$\Delta G_{wire} = -\left[\Delta\mu_{LS}^{\infty} - \Psi - \frac{2\gamma_{LV}(\Omega_S - \Omega_L)\sin\beta}{R}\right]\frac{c_1 r^2 h}{\Omega_s} + \Gamma c_2 h \tag{2.25}$$

Here, $\Gamma = (1-x)\gamma_{SL} + x(\gamma_{WV} - \gamma_{LV}\sin\beta)$ is the effective surface energy of the island as introduced in Ref. [37]. Following Ref. [37], we assume that γ_{SL} is identical for both crystal structures due to the close atomic environment on the surface around the two type of nuclei. $\Psi = 0$ stands for the ZB crystal phase and $\Psi = \Psi_{WZ}$ for the WZ crystal phase with Ψ_{WZ} as the difference of bulk cohesive energy between the ZB and WZ crystal structure at zero pressure.
From the change in free enthalpy we can derive the probability for the appearance of the different crystal phases. We maximize equation 2.25 in r and obtain an expression for the nucleation barrier ΔG^*:

$$\Delta G_{wire}^{*} = \frac{c_2^2}{4c_1}\frac{\Gamma^2 h\Omega_S}{[\Delta\mu_{LS}^{\infty} - \Psi - 2\gamma_{LV}(\Omega_S - \Omega_L)\sin\beta/R]} \tag{2.26}$$

Using equation 2.26, we can define the normalized nucleation barrier for ZB and WZ NWs:

$$\begin{aligned} g_{ZB} &\equiv \frac{\Delta G_{ZB}^{*}}{k_B T} = Q\frac{\epsilon^2}{f - (\omega-1)\delta/\rho} \\ g_{WZ} &\equiv \frac{\Delta G_{WZ}^{*}}{k_B T} = Q\frac{(\epsilon\eta)^2}{f - (\omega-1)\delta/\rho - 1} \end{aligned} \tag{2.27}$$

Here, f is the characteristic chemical potential and Q is determined by the island shape. The other parameters can be found in [23]. Due to the fact that both crystal structures can be formed independent of the nucleation site of the island, i.e. whether the nucleation occurs at the center line or the triple line, we define the probability to observe ZB or WZ crystal phase as:

$$p_{ZB} = p_{ZB,C} + p_{ZB,TL} \qquad p_{WZ} = p_{WZ,C} + p_{WZ,TL} \tag{2.28}$$

with $p_k = I_k / \sum_{k=1}^{4} I_k$ as the normalized probability for the different nucleation scenarios of equation 2.28. The growth rates I_k are proportional to $\exp(-g_k)$ where g_k are the nucleation barriers of equation 2.27. Additionally, we will account for the finite size of the top facet of the NW and the critical nuclei. The top facet is the last layer at the droplet-NW boundary. If the critical size of the nuclei is larger than the facet radius, the nucleation is impossible. We write for the growth rate in center and triple line position:

$$I_C = \rho^2 \exp(-g_C)\Theta(k_C\rho - \rho_C^*)$$

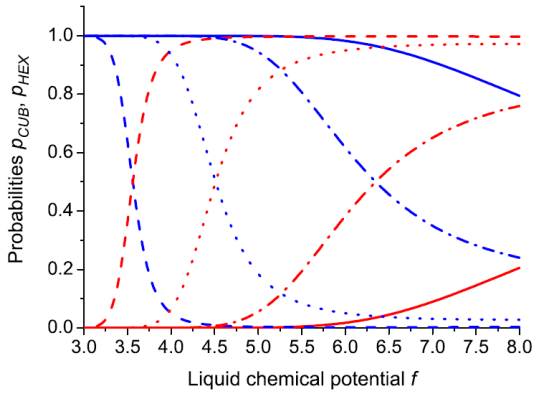

Figure 2.5: Probability to observe the cubic ZB crystal structure (CUB, decreasing blue curve) and the hexagonal WZ crystal structure (HEX, increasing red curve) as a function of the chemical potential of the droplet for different values of τ *(*$\tau = \gamma_{WZ}/\gamma_{ZB}$*).* $\tau = 0.95$ *is the solid line,* $\tau = 0.91$ *is the dash-dotted line,* $\tau = 0.875$ *is the dotted line and* $\tau = 0.83$ *is the dashed line. Taken from [23].*

$$I_{TL} = (2\rho\rho^*_{TL} - \rho^{*2}_{TL}) \exp(-g_{TL})\Theta(k_{TL}\rho - \rho^*_{TL}) \tag{2.29}$$

Here, Θ is the step function with $\Theta(x) = 1$ at $x > 0$ and $\Theta(x) = 0$ at $x < 0$. k_C and k_{TL} are geometrical coefficients such that $k_C\rho$ and $k_{TL}\rho$ are the maximum size of the nucleus on the center line and the triple line, respectively, and ρ is the size of the facet.

Figure 2.5 shows the probability to obtain WZ or ZB crystal structures as a function of the chemical potential of the droplet. The calculations were done for thin NWs. ρ was fixed at a value of 1.14, which yields a NW radius of 20 nm for GaAs NWs. The term τ, which is the ratio of the lateral surface energies of WZ and ZB NWs in contact with the vapor, $\tau = \gamma_{WZ}/\gamma_{ZB}$, influences the characteristic chemical potential f from equation 2.27 by the parameter $\eta_{TL} \cong \epsilon_{TL} - \sqrt{3}(1-\tau)/\epsilon_{TL}$. Due to the fact that γ_{WZ} is unknown, τ is unknown, but its value is assumed to be in the range of 0.75 to 1. The upper boundary is taken from Ref [37], which shows that the transition from WZ to ZB is only possible for $\tau < 1$. The lower boundary is obtained from a simple count of the dangling bonds of the lateral facets (4/3 bonds per layer for ZB and 1 bond for the WZ phase). Therefore, τ is varied between 0.97 and 0.83 for the calculations of figure 2.5. For $\tau > 0.97$, the NW will adopt the ZB phase in the whole growth domain with nearly 100% probability. At $\tau > 0.95$, the WZ crystal phase can be formed only at a very high liquid chemical potential with a probability of $< 20\%$. The curves for $\tau = 0.91$ and $\tau = 0.875$ show phase mixing at an intermediate value of the supersaturation while for $\tau = 0.83$ the ZB phase is observed at very low supersaturation. To summarize these results,

we found that for $\tau < 0.91$ the whole range from pure ZB to pure WZ crystal structure is accessible. The crucial parameter to obtain NWs with a distinct crystal phase is the supersaturation in the catalyst droplet, which has to be adjusted to the appropriate value by carefully tuning the growth parameters. We want to mention that we assumed mononuclear growth at the beginning of our analysis. Due to this constrain the presented model is not applicable for very thick NWs.

2.2 Magnetism

In this section we discuss the physical origin of diamagnetism, paramagnetism and ferromagnetism, following Ref. [2, 56]. We will use the magnetic susceptibility, $\chi = \frac{\partial M}{\partial H}$, with M as the magnetization of the material and H as the applied magnetic field to distinguish the three different types of magnetization. In the next step, the ferromagnetic phase transition in GaMnAs is explained within the framework of the RKKY interaction theory [69] and the Zener model [12, 13]. Finally we will investigate the magnetic anisotropies of GaMnAs with respect to the crystal orientation and to strain relaxation in case of very narrow GaMnAs strips.
The circular motion of the electrons around the core is the origin of the orbital magnetic moment. Besides the orbital magnetic moment, the electron has another magnetic moment due to its spin. The spin is - in a semi-classical picture - the rotation of the electron around its own axis. From the two parts, the orbital moment and the spin moment, the overall magnetic moment of an atom can be calculated. We want to mention that not only the localized electrons contribute to the magnetic properties but also the electrons in the conduction band and the cores of the atoms have a magnetic moment. Due to the fact that the magnetic moments of the conducting electrons, protons and neutrons are much smaller than the magnetic moments of the valence electrons, the magnetic properties are mainly determined by the valence band contribution while the other contributions can be neglected.
We will start our analysis with the phenomena of diamagnetism. In the case of diamagnetism the material, which is exposed to an external magnetic field, creates a magnetic moment which points into the opposite direction of the external magnetic field. Therefore the magnetic susceptibility χ is always < 0. The physical origin of this behavior is the electromagnetic induction, i.e. a changing magnetic field induces an electrical current into a closed circuit. On the atomic scale the electron orbits are the closed circuits. If the electrons are exposed to a changing magnetic field, they start to precess around the direction of the magnetic field vector. The induced current is directed such that the resulting magnetic moment points into the opposite direction of the applied magnetic field. The phenomena of diamagnetism can be

found in every material. In many cases the diamagnetic behavior is superimposed by stronger magnetic effects like para- or ferromagnetism.
In the case of paramagnetism, the material, which is exposed to an external magnetic field creates a magnetic moment which points into the same direction than the external magnetic field. Therefore, the magnetic susceptibility χ is always > 0. Paramagnetism can appear when the electron orbits of the atoms are not completely filled. According to Hund's rules, the resulting magnetic moments of the orbits and the spins are combined to the total magnetic moment of the atom. If an external magnetic field is applied, the magnetic moment of the atom will align in the direction of the external magnetic field. The magnitude of the magnetization depends on the magnitude of the applied magnetic field and on the temperature of the paramagnetic material. Without a magnetic field, the magnetic moments are randomly distributed due to thermal motion. With increasing magnetic field and decreasing temperatures, the magnetic moments are oriented more and more in the direction of the magnetic field vector. At very high fields and very low temperatures, all magnetic moments are directed in the field direction and the magnetization saturates. If the external magnetic field is switched off, the magnetization disappears due to the thermal motion of the atoms. Paramagnetism can be observed in platinum, palladium, magnesium, calcium, aluminium, chrome, molybdenum and manganese. For ferromagnetism a material, which is exposed to an external magnetic field, creates a magnetic moment which points into the same direction than the external magnetic field with $\chi >> 0$. Like in case of paramagnetism, the appearance of ferromagnetism is only possible if the electron orbits of the atoms are not completely filled. In contrast to the paramagnetic case, the crucial quantity for ferromagnetism is not the orbital moment or the total magnetic moment of the atom but the spin moment of not fully filled inner orbits. It should be noted that ferromagnetism is not the phenomena of an individual atom and can only be observed in an ensemble of atoms, which have a crystalline order. To understand how the ferromagnetic phase is developed, we will use the Heisenberg model of magnetism. The Hamiltonian of the Heisenberg model can be written as

$$H = -\sum J_{ij} S_i S_j \tag{2.30}$$

J_{ij} is the exchange integral, which describes the overlap of the wave functions, while S_i and S_j refers to the spins of atom i and j. The exchange integral J_{ij} strongly depends on the distance between the atoms. At large distances, $J_{ij} = 0$ and no ferromagnetism can be observed. If the distance is reduced, the exchange integral adopts positive values and the spins of the electrons are aligned parallel. The regions in which the spins are aligned in one direction are so called Weiss domains. The

Weiss domains are separated from each other by Bloch walls. Without an external magnetic field, the magnetizations of the different Weiss domains cancel each other and the overall magnetization is zero. If a magnetic field is applied, the domains turn into the direction of the applied magnetic field and the magnetization of the material increases significantly. At a certain intensity of the applied magnetic field all Weiss domains are oriented in the same direction and the magnetization saturates. If the direction of the magnetic field is reversed, the magnetization of the material is fully or partly conserved. The remaining magnetization at zero magnetic field is called remanence. At a certain negative value of the external magnetic field, the magnetization of the material switches into the opposite direction. The magnetic field at which the switching in magnetization occurs is called the coercive field. As a consequence, a hysteresis is observed if the external magnetic field is sweeped forward and backward. For the sake of completeness we want to mention that the exchange integral can decrease and show negative values, when the distance between the atoms is further reduced. In this case the spins are oriented anti-parallel and the phenomenon of antiferromagnetism is observed.

2.2.1 Ferromagnetism in GaMnAs

Ferromagnetism in GaMnAs is supposed to be carrier induced [12, 13]. This is indicated by the fact that for fully carrier compensated GaMnAs the formation of an antiferromagnetic phase is observed [75]. Due to the fact that Mn is most likely incorporated on Ga sites in the GaAs crystal (cf. figure 2.6 (a)), Mn works as acceptor and provides one hole. The holes couples antiferromagnetically to the Mn atoms and therefore mediates a ferromagnetic coupling between them. The inner 3d shell of Mn is occupied with five electrons. According to Hund's law, the spins of these electrons are oriented in the same direction. As a consequence, each of the Mn atoms provides a magnetic moment of five μ_B to the overall magnetization. The indirect exchange interaction between the Mn atoms is shown schematically in figure 2.6 (b).

The mechanism of the hole mediated ferromagnetism fits into the framework of the Ruderman-Kittel-Kasuya-Yosida (RKKY) interaction theory [69], which was developed in the middle of the fifties. This theory is based on the ideas of M.A. Ruderman and C. Kittel, who described the long range interaction between nuclear spins using an electron of the conduction band as mediator. The idea was later adapted by T. Kasuya and K. Yosida to explain the formation of a ferromagnetic phase. The form of the Hamiltonian in the RKKY theory is similar to the case of direct ferromagnetism:

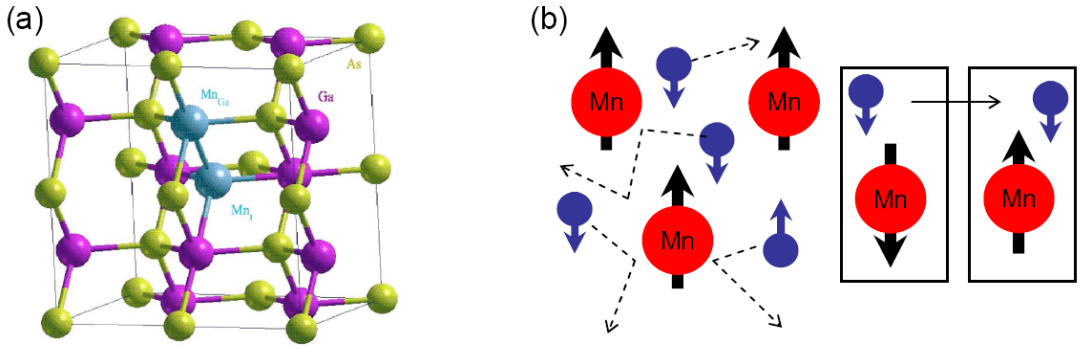

Figure 2.6: (a) The incorporation sites of Mn, (b) the ferromagnetic coupling mechanism between the Mn atoms. Taken from [31].

$$H^{RKKY} = -\sum J_{ij}^{RKKY} S_i S_j \tag{2.31}$$

where

$$J_{ij}^{RKKY} = \frac{g^2 k_F^6}{E_F} \cdot \frac{\hbar^2 V^2}{(2\pi)^3 N^2} F(2k_F R_{ij}) \tag{2.32}$$

and

$$F(x) = \frac{\sin x - x\cos x}{x^4} \tag{2.33}$$

Here, g is the Landé factor, k_F is the Fermi wave vector, E_F is the Fermi energy, $\hbar$ is the reduced Planck constant, V is the volume, N is the number of charge carriers and r_{ij} is the distance between the magnetic ions. From the function F(x) we can derive two characteristics of the RKKY theory. First, the exchange integral $J_{ij}^{RKKY} \sim \frac{1}{r_{ij}^3}$. This means that the RKKY exchange interaction has a very large range compared to the direct exchange interaction, which decays exponentially. Second, the RKKY exchange interaction is oscillating and can change its sign, which means that a ferromagnetic and an antiferromagnetic order could be observed alternately. The fact that such a behavior never showed up in GaMnAs is related to the relatively low hole concentration of GaMnAs [75]. The hole concentration appears as quadratic term in the denominator of the exchange integral. It is assumed that the first zero of the oscillation, beyond which the interaction changes its sign and becomes antiferromagnetic, occurs at a much greater distance between the magnetic ions than the cut-off length of the interaction.

A different approach to explain the ferromagnetic phase transition in GaMnAs is given by the Zener model [12, 13]. This model is, by its own statement, equivalent

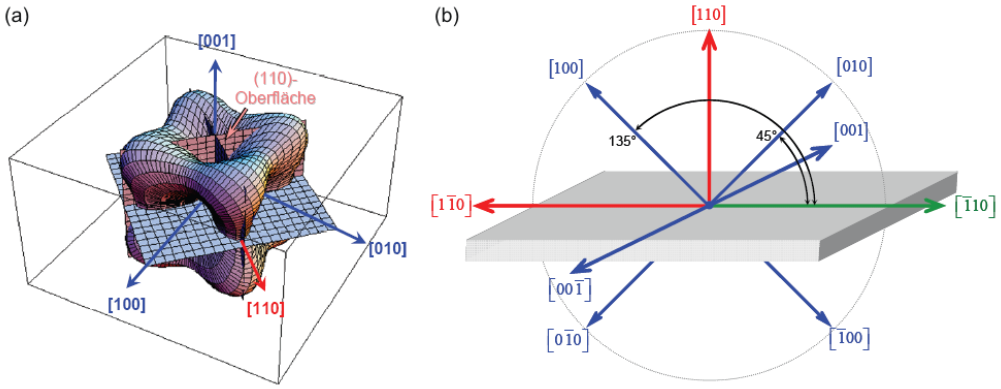

Figure 2.7: (a) The free energy surface of (110) oriented GaMnAs, data obtained by ferromagnetic resonance spectroscopy. (b) Orientation of the three magnetic easy [100] axes on the (110) oriented GaMnAs layer. Taken from [14].

to the RKKY model for the case of semiconductors. The application of the Zener model allows us to find the correlation between Curie temperature, the effective Mn density x_{eff} and the hole density p [113]: $T_C \sim x_{eff} p^{1/3}$. Here we have to note that Mn can not only occupy Ga sites. Depending on the growth parameters and especially on the Mn content, Mn is also incorporated as Mn interstitial defect. In this case, Mn acts as double donor and reduces the effective Mn- and hole density. Additionally, it couples antiferromagnetically the other Mn atoms. A similar effect is caused by As atoms, which occupy Ga sites. These defects, called As antisites, also work as double donors.

2.2.2 Magnetic anisotropies in GaMnAs

The origin of the magnetic anisotropies in GaMnAs is rather complex. A detailed discussion of this subject can be found in [14], where the magnetic anisotropies of three substrate orientations are investigated. For our purpose, the magnetic anisotropies of the (110) and (211) crystal orientations are of interest. As we will see later, these crystal orientations are equivalent with the crystal orientations of the NW side facets. Unfortunately, there is no data available for the (211) crystal orientation. The (110) crystal orientation shows a cubic anisotropy, with three easy axes oriented along the [100], [010] and [001] direction. As a consequence, one of the easy axes is in plane while the other two point out of plane in an angle of 45°. This is illustrated in figure 2.7.

The magnetic anisotropies of GaMnAs can be manipulated using nanopattering. For the case of very narrow GaMnAs strips, i.e. a few hundred nanometer in diameter or

below, the cubic anisotropy is superimposed by a uniaxial anisotropy term, which is directed parallel to the strip. The origin of this behavior is attributed to the strain relaxation of the narrow strip perpendicular to the strip direction [48, 115], which is accompanied by a change in the lattice constant.

2.3 Magnetic and non magnetic NWs: State of the Art

At the beginning of my PhD thesis in April 2008 the field of NW research was just moving in the focus of the public attention. Since that, the number of publications on this topic has increased exponentially. The starting point of the NW research activities can be dated back to the early nineties [45]. After this first attempt, nearly one decade passed by until the idea of NW fabrication was revived. In 2001 the Lund group published a paper which systematically investigated size-, shape- and position control of GaAs nanowhiskers [74]. This paper was followed by two publications from the same group in 2003 and 2006, which deal with the fabrication of NW transistors [7, 106]. In the following, big industrial research companies like IBM and Philips contributed with NW based devices like silicon based tunneling FETs [6] or single quantum dot NW LEDs [66]. All these projects were carried out using chemical vapor deposition or metal organic vapor phase epitaxy for the synthesis of the NWs.

For the case of MBE growth, the NW research activities started much later. In 2006 and 2007 the first systematic studies of Au catalyzed NW growth were carried out [42,83,104]. Also the morphology of the NWs was studied [62]. The Ga catalyzed growth method was developed in 2008 [49, 50]. The theory of NW growth could explain most of the underlying physics, i.e. adatom diffusion was identified as the central point of the growth process [21] and also the rules for the formation of the WZ or ZB crystal phase were specified [37]. A universal theory, which combines both topics as well as a recipe for the growth of WZ and ZB NWs was not developed at this time.

The material system of GaMnAs was already intensively studied in the year 2008. After the first publication of Ohno in 1996 [77], properties like the band structure [76], hole density [93] and the influence of crystal defects on the magnetic properties [113] were investigated. For my project the work of GaMnAs growth on different substrate orientations [87, 118, 119] was of great interest, especially the growth on (110) oriented GaAs substrates [118, 119].

In the field of magnetic NWs, three publications were present before 2008. Martelli

et al. grew GaAs NWs with MBE, using Mn as catalyst material [63]. The obtained nanostructures showed a nonuniform morphology where leaf-like structures are observed as well as wire-like structures. The wire like structures grew undirected and varied in size over a broad range. The NWs were investigated with photoluminescence spectroscopy (PL) and scanning electron microscopy (SEM). Magnetic investigations were not carried out, because the aim of the publication was most likely to test Mn as possible catalyst material and not to create ferromagnetic NWs. Indeed it is very probable that the incorporated amount of Mn in the GaAs NW via the Mn droplet is much too small to achieve ferromagnetic NWs.
Jeon et al. reported the growth of GaMnAs NWs with a Mn-content of 20% and a Curie temperature above room temperature [51]. This publication is rather controversial. First of all the described formation mechanism of the GaMnAs NWs, which assumes the formation of GaMnAs nanoislands due to the lattice mismatch between GaAs and GaMnAs and the creation of catalyst droplets from these nanoislands, is very speculative, which was also mentioned by [90]. Second, the SEM pictures of the NW sample show very inhomogeneous structures which can hardly be identified as NWs. Third, there is no information in the publication, how the SQUID measurements were performed. It is very probable that the "as grown" sample were measured. In this case, the measurement would also include the GaMnAs or MnAs layer, which was grown between the NWs. Kim et al. reported the fabrication of ferromagnetic GaMnAs NWs with a Mn content of 1% and a Curie temperature above room temperature in 2009. This publication is again rather controversial because a ferromagnetic phase transition was observed for GaAs NWs, also above room temperature [55].
Finely, Sadowski et al. reported the growth of GaMnAs NWs at MnAs segregation conditions [90]. Also this paper is slightly controversial. On the one hand, Sadowski claimed that the NW growth is catalyzed by a MnAs droplet, which is formed due to the high growth temperatures between 300°C and 350°C. This is supported by element sensitive energy dispersive x-ray spectroscopy (EDX) measurements, which show a Mn/As ratio close to 1 at the tip of the NWs. On the other hand, Sadowski says that the NWs are GaMnAs- and not GaAs NWs with MnAs inclusions. The second scenario is much more probable, because GaMnAs is usually not created at MnAs segregation conditions. Sadowskis only hint for the existence of a GaMnAs phase is a SQUID measurement, which shows a very complex behavior and can therefore be interpreted in many ways. The obtained NWs are nonuniform in size, strongly tapered and branched. Their suitability for device fabrication is questionable.

Chapter 3

Methods

In this chapter we present the used devices as well as the sample preparation and characterization techniques. First we focus on the preparation techniques which were applied before the growth process. Then we discuss the geometry of the sample holder and the molecular beam epitaxy (MBE) setup. We explain the different components of the MBE system and the reflection high energy electron diffraction (RHEED) system, which is used for flux calibration and diffraction pattern analysis. Next we deal with the post growth annealing oven, which was built to improve the Curie temperature of the ferromagnetic NW samples. At the end of this chapter the two main characterization techniques, scanning electron microscopy (SEM) and transport measurements are presented.

3.1 Sample preparation

The starting material for the Au catalyzed growth method, which is a GaAs wafer with a thin Au film (Au layer thickness between 0.5 Å and 10 Å), was at first provided by A. Petroutchik and L. T. Baczewski from the Institute of Physics, Warsaw. From the second year of my PhD thesis, the Au film was deposited on GaAs substrates in Regensburg, using the metal MBE system of Prof. Dr. Back.
The starting material of the Ga catalyzed growth method, a GaAs wafer with a thin SiO_2 layer, was provided by Prof. Dr. Fontcuberta i Morral from the Walter Schottky Institut in Munich (now École Polytechnique fédérale de Lausanne). The silicon wafers with thermal and native oxide were bought from Silicon Materials.

3.1.1 Deposition of the Au film

For the Au assisted growth method, a thin Au film was deposited on the GaAs substrate using the metal MBE system of Prof. Dr. Back. The substrate was mounted on a special sample holder. The sample holder was introduced in the growth chamber and placed outside the range of the effusion cells. Then the electron vaporizer of the Au effusion cell was switched on. The Au flux was monitored with a quartz crystal microbalance for at least 15 minutes to ensure that the Au flux is constant. After the flux calibration, the sample holder was turned into the Au beam. To make the Au layer deposition as precise as possible, small growth rates between 2.5×10^{-3} Å/s and 3.7×10^{-3} Å/s were chosen. This leads to growth times between 135 s for a 0.5 Å thick Au film and 3000 s for 10 Å thick Au film.

3.1.2 Wet chemical etching

For the Ga assisted growth method, a SiO_2 layer with a thickness of 30-40 nm was sputtered onto the GaAs substrate. To achieve directed NW growth and a high NW density, the SiO_2 layer has to be thinned down below 5 nm. Due to the fact that SiO_2 is a very persistent material, Ammonium fluoride has to be used for the thinning procedure (Riedel-de Haën, Ammonium fluoride etching mixture AF 875-125). The etching mixture with a HF-concentration of 12.5% was diluted to 1.25% with ultra pure water from the clean room in order to reduce the etching rate and thereby make the etching process more reproducible. The obtained etching rate of 1.2 nm/s, which could be determined very precisely (cf. figure 3.1), perfectly fits our requirements.

After the etching procedure, the sample was put in two consecutive water baths for one minute to stop the etching process. The etching process of SiO_2 is highly selective with respect to GaAs, which is not affected until the HF concentration is higher than 50% [122]. Additionally, the etching process is isotropic with respect to the sputtered SiO_2 on GaAs substrates, i.e. the etching rate is the same for all spatial directions. In contrast, the evaluation of the etching procedure for thermal SiO_2 on silicon substrates showed that the etching process is often anisotropic [53]. The reason for this behavior is most likely the non uniform quality of the thermal SiO_2. As a consequence, the fast etching direction can be oriented in the z-direction or in the xy-plane. A prediction of the preferential etching direction is not possible. The native SiO_2 on silicon substrates is ab initio very thin and an etching step is therefore not necessary.

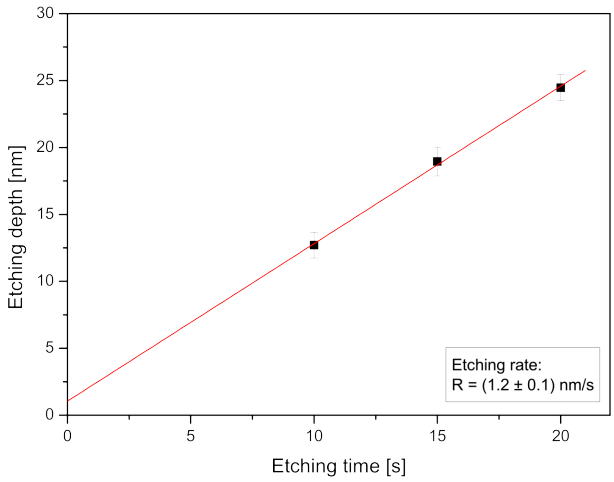

Figure 3.1: The etching rate of Ammonium fluoride with a HF concentration of 1.25%.

3.1.3 Cleaving and chemical cleaning

The two inch (111)B oriented wafers were cleaved to 5x10 mm^2 pieces, which is the appropriate size for the semiconductor MBE sample holders. The size was chosen because the corresponding samples provide a sufficient amount of NWs for characterization. Additionally, a large number of sample pieces - 24 in the best case - can be cut out of a two inch wafer. This is important because only sample pieces, which originate from the same wafer are really comparable with respect to the Au layer thickness and the surface roughness. Both quantities can affect the NW morphology and crystal structure, as we will discuss later.

The scribing was done with a tungsten-carbide needle using a computer assisted scribing system. As reference point, the primary flat of the two inch wafer, which is a $(01\bar{1})$ plane, was used. At first three 10 mm broad strips, which are oriented perpendicular to the primary flat were cut out of the wafer. The strips exhibit a hard breaking (100) plane. To ensure that the wafer will break in the intended direction, the needle was weighted with 20 g. To separate the strips from the each other, two tweezers were placed left and right close to the scribe and carefully twisted into opposite directions. Afterwards, the strips were scribed into 10x10 mm^2 squares and finally into 5x10 mm^2 sample pieces. This is shown schematically in figure 3.2. The sample pieces can be separated from each other by putting them upside down on a lint-free cloth and applying carefully some pressure on the backside.

After cleaving, the sample pieces were cleaned to ensure that no dirt from the scribing

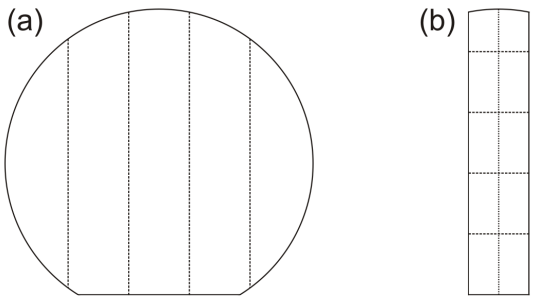

Figure 3.2: The wafer scribing procedure. (a) The wafer is cleaved in strips with a width of 10 mm, (b) the strips were cleaved in 10x10 mm^2 squares and finally in 5x10 mm^2 sample pieces.

procedure is introduced into the semiconductor MBE system. Therefore, the sample pieces were put into two consecutive Acetone baths at 60°C and a Propanol bath at 70°C for 20 minutes, respectively. Finally, the Propanol was blown off with nitrogen and the samples were stored in a desiccator box.

3.2 Sample holder

The following section is dedicated to the sample holders for the semiconductor and the metal MBE system. All sample holders exhibit a special geometry. The sample holder for the metal MBE system and one sample holder for the semiconductor MBE system were designed to host 2 inch wafers. The other two sample holders for the semiconductor MBE system can carry sample pieces of 5x10 mm^2. Both geometries have some advantages and disadvantages, as we will discuss later. Furthermore, the sample holders for the silicon samples exhibit a special system for sample mounting, because the usual method, i.e. using Ga as adhesion agent between the sample holder and the GaAs substrate, is not possible for Si substrates.

3.2.1 Design and geometry of the sample holder

A sample holder for two GaAs samples with a size of 5x10 mm^2 is shown in figure 3.3 (a). The samples are mounted in the middle of the sample holder. If just one sample should be grown, the other sample position is covered by a 5x10 mm^2 dummy wafer. On the left and right side of the sample position, two big semicircular dummy wafers are mounted onto the sample holder. The corridor between the big dummy wafers remains uncovered.
The advantage of this geometry is that RHEED investigations of the samples along

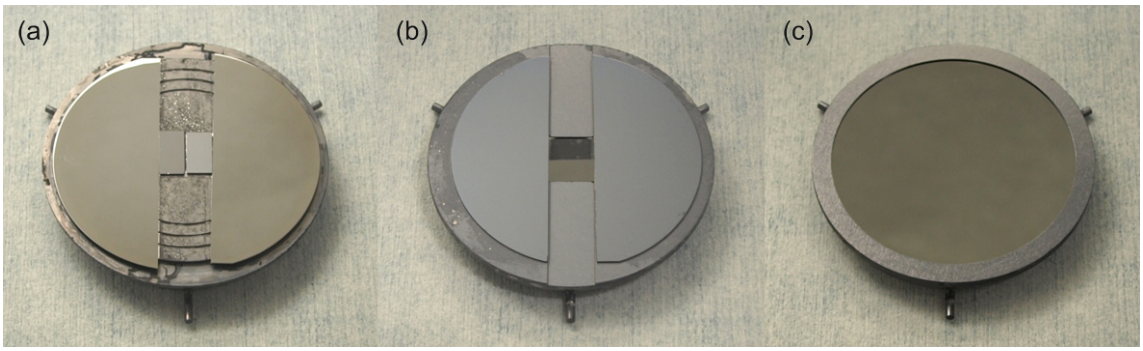

Figure 3.3: Sample holder for the (a) Ga and (b) Si 5x10 mm^2 sample pieces and (c) for a Si two inch wafer.

the uncovered corridor are possible because the electron beam is only reflected from the sample pieces and not from the metallic sample holder. If the free corridor between the two semicircular dummy wafers would be occupied by additional dummy wafers, the RHEED pattern would always be a superposition of the dummy wafers and the sample pieces. The disadvantage of this geometry is that the free corridor becomes rougher with every growth run as GaAs sticks to the metal surfaces. The rougher surface leads to a larger heat emission and thereby to a decreasing substrate temperature at a constant heating power over time. This effect is of the order of 1°C for an amount of 1 μm GaAs 2D growth. To ensure that the growth temperature is constant for a series of samples, the manipulator power has to be adjusted from time to time.

In figure 3.3 (b) and (c), the sample holders for the Si samples are shown. The sample holder in figure 3.3 (b) can be loaded with two 5x10 mm^2 sample pieces, similar to the GaAs sample holder. The sample holder in figure 3.3 (c) can be loaded with a two inch wafer. Due to the fact that Si forms an eutectic with Ga, Ga cannot be used as adhesion agent between the Si wafers and sample holder because the Si samples would most likely slide down when the eutectic is formed. Instead of using Ga as adhesion agent, the Si samples are clamped in the sample holder by a boron nitride plate from the back side. This mounting method works well in case of the two inch wafer sample holder but causes some problems for the 10x10 mm^2 sample holder. In the latter case, the boron nitride plate has a hole with a diameter of approximately 14 mm right behind the sample position, to ensure that the sample heater directly heats the substrate. The sample pieces exhibit small gaps right and left of the sample position. The hole in the boron nitride plate and the gaps between the sample and the sample holder cause serious problems with the temperature measurement, as the pyrometer can ”see” the heating filament and

therefore measures too high temperatures. The fabrication of a continuous boron nitride plate is suggested to eliminate this problem.
A third kind of sample holder was used for the metal MBE system. To avoid an additional cleaning step for GaAs wafers and to enable the use of Si wafers on this sample holder, a clamp based sample mounting system was used.

3.2.2 Temperature behavior of the GaAs sample holder

Next we will discuss the temperature behavior of the 10x10 mm^2 GaAs sample holder, which is very important especially for the low temperature growth of GaMnAs. As mentioned above, the sample holder is heated by a filament, which is separated from the sample holder through a boron nitride plate. The filament is the main but not the only heat source, which affects the temperature of the samples. An additional contribution to the sample temperature is made by the effusion cells. Depending on the number and temperature of the used effusion cells and especially on the heating power of the filament, the contribution of the cells to the sample temperature ranges from 3-5°C for high growth temperatures of 600°C to 40-60°C for low growth temperatures of 200°C. Due to the fact that GaMnAs has to be grown at low growth temperatures, the huge increase in temperature by opening the cells has to be compensated in order to achieve high quality GaMnAs samples.
As a first step, the dependence of the sample temperature on the filament voltage was investigated. Figure 3.4 shows the results for the Bandit bandgap absorption spectrometer in the range of 12 V to 20 V filament voltage.
The increase of the sample temperature with the filament voltage is strictly linear in this temperature regime. An increase of 1 V corresponds to a temperature increase of 20°C. Next, the influence of opening the Ga cell on the sample temperature was monitored for three different filament voltages, which correspond to sample temperatures of 155°C (14 V), 215°C (17 V) and 275°C (20 V). The Ga cell temperature was set to 960°C. From figure 3.5 (a) we deduce two important things. First, we see that the influence of the open Ga cell on the sample temperature increases with decreasing filament voltage. Additionally the time, for which the thermal equilibrium of the sample holder is reached increases with decreasing filament voltage. In case of a filament voltage of 20 V, the sample temperature is nearly stable after 15 minutes while it takes 20 minutes for a filament voltage of 17 V and 25 minutes for a filament voltage of 14 V. These investigations were also performed for the case that the Ga- and Mn cells are opened simultaneously. The results are similar to the results shown above, just the increase in temperature is more pronounced.
In figure 3.5 (b) the total increase in temperature for the three different filament

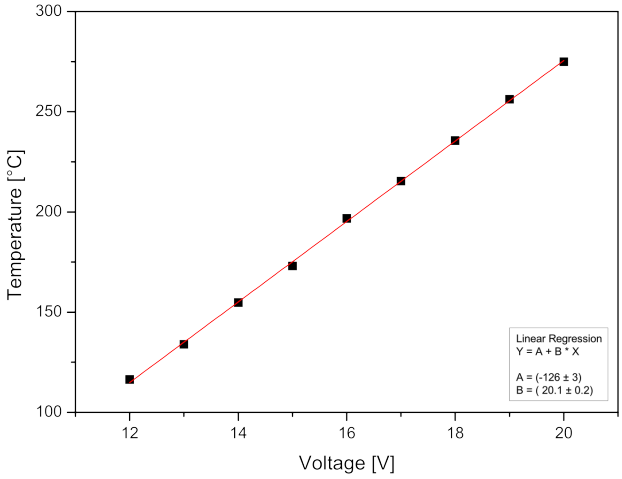

Figure 3.4: Dependence of the sample temperature on the filament voltage.

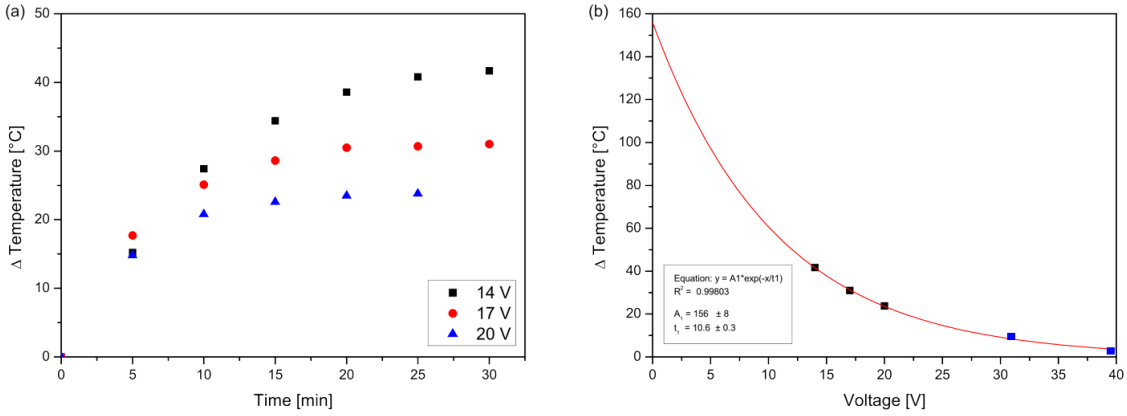

Figure 3.5: (a) Increase of sample temperature as a function of time for three different filament voltages and a Ga cell temperature of 960° C. (b) Dependence of the sample temperature on the filament voltage in the range of 0 V to 40 V for a Ga cell temperature of 960° C. An exponential function is used to fit the data points between 14 V and 20 V (black squares). The data points at 32 V and 40 V were not used for the fit (blue squares).

Sample temp. [°C]	1 step [V]	2 step [V]	3 step [V]	V-diff. [V]
200	-9	+5.7	+1	-2.3
215	-7.5	+4.4	+1	-2.1
220	-7	+4	+1	-2
230	-6	+3.2	+1	-1.8
240	-5	+2.7	+1	-1.3
250	-4	+1.7	+1	-1.3
260	-3.5	+1.2	+1	-1.3
270	-3.2	+1	+1	-1.2
280	-3	+1	+1	-1
290	-2.7	+1	+0.7	-1
300	-2.5	+1	+0.5	-1
310	-2.3	+0.8	+0.5	-1
320	-2	+0.5	+0.5	-1

Table 3.1: The three steps of the temperature compensation procedure for the temperature range of 200° C to 320° C.

voltages is plotted. The data points between 14 V and 20 V, which are obtained from figure 3.5 (a) after the temperature has reached a stable value, were fitted with different types of functions. To clarify, which type of function is most suitable to model the behavior of the sample holder, the results of the fits were compared with data points obtained at high filament voltages. This data points were excluded from the fit because they were measured with a pyrometer and are therefore not absolutely comparable to the data points obtained by the bandgap absorption spectrometer. We find that an exponential decay is the best fitting function, which can predict the increase in temperature for the voltage range between 32 V and 40 V, despite the fact that only the data points between 14 V and 20 V were used for the fit.

With these results at hand, we can start to develop a temperature compensation procedure, which can reduce the increase in sample temperature when one or more effusion cells are opened. We have to take into account that due to the heat capacity of the sample holder, the response to filament voltage changes is delayed. After some experiments, a three step compensation procedure was developed which could reduce the temperature fluctuations from 60°C to ± 3°C. The procedure is summarized in table 3.1.

The numbers in column 2-4 give the change in filament voltage. The first step was

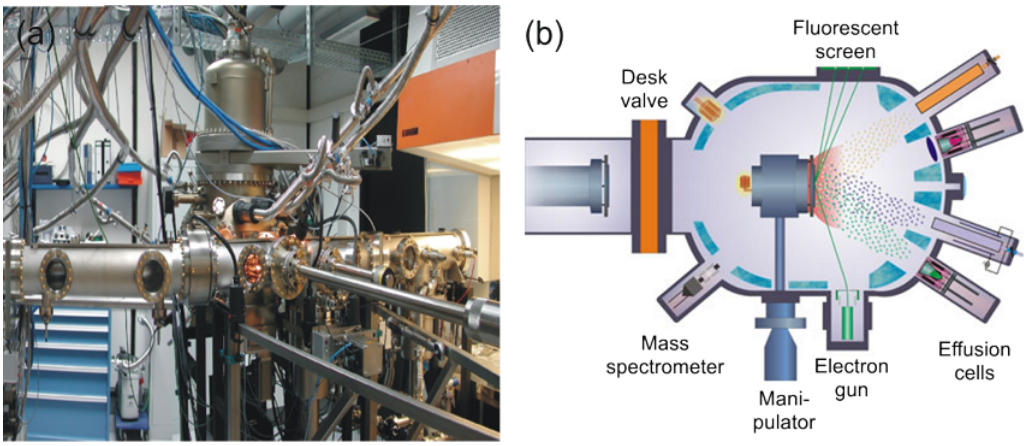

Figure 3.6: (a) Picture of our MBE system, (b) schematic drawing of the MBE growth chamber. Taken from [29].

executed immediately after the growth had started, the second step one minute after the growth had started and the third step 6 minutes after the growth had started. The numbers in column 5 gives the difference of the filament voltage between the beginning and the end of growth.

3.3 Molecular beam epitaxy

Molecular beam epitaxy (MBE) is a procedure for the fabrication of ultra clean samples with atomic precision. The concept of MBE can be applied to different material systems like insulators, semiconductors or metals. MBE is used for fundamental research as well as for industrial applications. A typical MBE growth chamber is equipped with effusion cells, a manipulator which hosts the samples and a monitoring system like reflection high energy electron diffraction (RHEED). Figure 3.6 (a) shows a picture of our MBE system.
To achieve a high degree of sample purity, the growth chamber is evacuated to ultra high vacuum (UHV, 10^{-7} Torr to 10^{-12} Torr). For a typical growth chamber with a diameter of approximately 1 meter a pressure in the 10^{-4} Torr range is needed to ensures that the mean free path of the evaporated materials is larger than the distance between effusion cells and sample, so that the material can reach the sample without being affected by residual gas molecules. The UHV guarantees that almost no residual gas molecules condense on the substrate surface and are unintentionally incorporated in the crystal during the growth process.
The growth process in MBE is usually an epitaxial process, i.e. the grown structure adopts the crystal phase of the substrate. To monitor the growth process and the

sample quality, surface sensitive methods like RHEED are used. Besides the fact that RHEED can provide information about the surface roughness, it can also be used for NW crystal structure investigations.

3.3.1 The MBE system

The MBE system used for the sample fabrication is a modified Veeco Gen-II-system. The MBE system consists of an entry chamber, a buffer chamber and a growth chamber, which are separated from each other by gate valves. The entry chamber is equipped with a heating coil for the degassing of the substrates and a cryogenic pump, which provides a pressure down to 5×10^{-9} Torr. The buffer chamber is equipped with a heating station for a single sample holder. Here, the sample holder is heated to 400°C to remove the last residues of water and other vaporable contaminations. The vacuum in the buffer chamber is generated with a cryogenic pump and can reach pressures below 10^{-10} Torr. The growth chamber is equipped with a heatable manipulator, an ion gauge, several effusion cells, a large cryogenic pump, a titanium sublimator, a pyrometer port and a RHEED system. A schematic drawing of a typical MBE growth chamber is given in figure 3.6 (b).

Manipulator and ion gauge

The manipulator hosts the sample holders, which are fixed on the manipulator with a bayonet lock. The sample holder is heated by a filament heating, which is mounted on the manipulator. The filament heating is separated from the sample holder by a boron nitride plate. The manipulator can be rotated by 360° around two axes and also a continuous rotation around one axis is possible. The hot filament ionization gauge is mounted behind the manipulator. It is used for the determination of the beam fluxes, especially for the fluxes of As and Mn. The Mn flux measurement is of special interest, as the magnetic properties of GaMnAs strongly depend on the Mn concentration. Due to the fact that the Mn pressure is very small, the Mn flux measurement should be performed when the As cell is cold. Otherwise, the background pressure of As is of the same order of magnitude as the Mn pressure, which causes a big uncertainty in this measurements. Additionally, the Mn cell should be opened several times for at least 30 second before the Mn flux is measured, to ensure that the Mn flux is constant.

The effusion cells

Different kinds of effusion cells are used. We can distinguish between the regular Knudsen Cells, which contain Gallium (two cells), Indium, Aluminium and Manganese. The materials are placed in crucibles of pyrolytic boron nitride (PBN) and heated with a resistance heating. The material fluxes are adjusted over the cell temperatures and controlled by shutters, which are located at the front end of the cells. For the supply with Arsenic, a valve-cracker cell is used. This kind of cell has a needle valve, which allows a very precise regulation of the As flux. Additionally, the cell is equipped with an As cracker which converts As_4 molecules into As_2 molecules at a cracking temperature of 850°C. The two other cells, which contain Silicon and Carbon, are doping cells. Due to the fact that the temperature, which has to be applied for the sublimation of Si and C is very high, no PBN crucibles are used to host these materials. Instead, high currents between 6 A and 14 A for Si and 45 A to 60 A for C were applied directly to filaments of the corresponding materials to evaporate these species.

The pumps

The biggest pump in the growth chamber is the cooling shroud. The cooling shroud, which is fed with liquid nitrogen from a phase separator encloses large parts of the growth chamber and has therefore a huge surface. The pump effect is generated by adhesion of gas molecules on the cold shroud surface. Additionally, a cryogenic pump is mounted on top of the growth chamber. Due to its large diameter, which meets the diameter of the growth chamber, the cryogenic pump in combination with the cooling shroud provides a pressure down to 2×10^{-11} mbar. A titanium sublimator pump is located opposite to the cryogenic pump on the bottom of the growth chamber. This pump, which uses titanium to getter molecules from the gas phase, is only used after a chamber opening.

Determination of the sample temperature

For the determination of the sample temperature, two pyrometers and a band gap absorption spectrometer are available. The two pyrometers are calibrated for different temperature regimes. The low temperature pyrometer is calibrated for a temperature range between 100°C and 700°C while the high temperature pyrometer is calibrated for a temperature range between 400°C and 800°C. For the temperature measurement, the pyrometer detects the emitted black body radiation of the substrate in a specified wavelength range, e.g. 0.91-0.97 μm for the high temperature pyrometer. Due to the fact that the substrate is no ideal black body, the measured

data is multiplied with a correction factor which depends on the material properties, i.e. on the surface roughness of the substrate. From the measured intensity of the radiation and the correction factor, the temperature is calculated.
The band gap absorption spectrometer, in the following called Bandit, is calibrated for low temperatures up to 560°C. The Bandit uses a bright lamp, which is focused on the substrate and a spectrometer, which detects the reflected light. Due to the fact that the band gap in GaAs is temperature dependent, the substrate temperature is obtained by simply comparing the reflected wavelength spectrum with the wavelength spectrum of the calibration file. This method is very trustworthy and precise, because other heat sources like the open effusion cells or the sample holder do not affect the Bandit measurement.

3.3.2 The RHEED system

The RHEED system consists of an electron gun and a fluorescent screen. The electron gun emits electrons, which are accelerated by a voltage of 15 kV. The electrons hit the surface of a sample under a very small angle of approximately 3°. As a consequence of the small angle of incidence, the electrons are diffracted by the first few monolayers of the wafer and reflected to the fluorescent screen, where the diffraction pattern becomes visible. RHEED can be used for the determination of the element III-fluxes and for the investigation of the NW crystal structure.

Flux calibration

For the flux calibration, the electron beam is directed on a 5x5 mm^2 sample of (001) oriented GaAs, which was smoothed before by growing a GaAs buffer layer followed by an AlGaAs/GaAs super lattice. To concentrate the intensity on the central spot of the diffraction pattern and thereby improving the intensity of the RHEED oscillations, the wafer is tilted by 1-2°. The origin of the RHEED oscillations is the electron scattering, which depends on the roughness of the substrate surface. This is illustrated in figure 3.7.
The electron scattering is minimal when the surface of the wafer is flat. Therefore, the intensity of the reflected electron beam is maximal. If a new monolayer is started, the waver surface becomes rougher and the electron scattering increases. As a consequence, the intensity of the reflected electron beam is reduced. When the new monolayer is half-finished, the surface roughness reaches its maximum and the intensity of the reflected electron beam is minimal. As the monolayer is filled up, the surface becomes smoother again and the intensity of the reflected electron

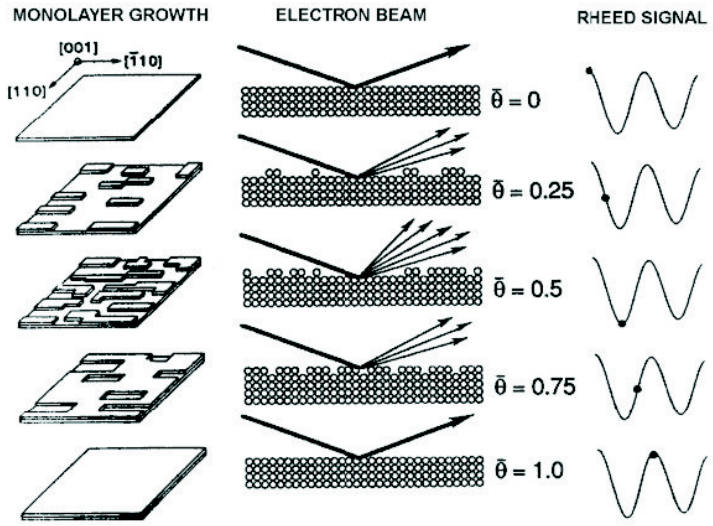

Figure 3.7: Electron scattering and the corresponding RHEED oscillations with respect to the surface roughness. Taken from [114].

beam increases. Finally, the intensity of the reflected electron beam reaches again its maximal value when the monolayer is completed.
To achieve good RHEED oscillation, the As flux has to be adjusted properly. Nearly undamped oscillations can be observed for As fluxes of 1.2×10^{-6} Torr for a Ga rate of 0.2 Å/s, 2×10^{-6} Torr for a Ga rate of 0.4 to 0.8 Å/s and 5×10^{-6} Torr for a Ga rate of 2.8 Å/s.

Diffraction pattern

Due to the fact that the edges of the NW samples grown on (111)B oriented substrates are oriented along the [011] and [112] crystal direction, the electron beam of the RHEED system has to be aligned parallel to the corresponding edge to obtain the appropriate diffraction pattern. Note that the [112]/[011] crystal direction in ZB is equivalent to the [0110]/[0112] crystal direction in WZ crystal phase, respectively. Figure 3.8 shows the RHEED diffraction pattern of WZ (figure 3.8 (a)/(b)) and ZB (figure 3.8 (c)/(d)) NWs for the [011]/[0112] and [112]/[0110] direction, respectively. Figure 3.8 (e)/(f) shows the RHEED diffraction pattern for the ZB NWs after the GaMnAs shell growth along the [011]/[112] direction. The diffraction pattern of WZ NWs after GaMnAs shell growth look very similar to the diffraction pattern of ZB NWs after GaMnAs shell growth. Due to the inferior quality of these images they are not shown here.

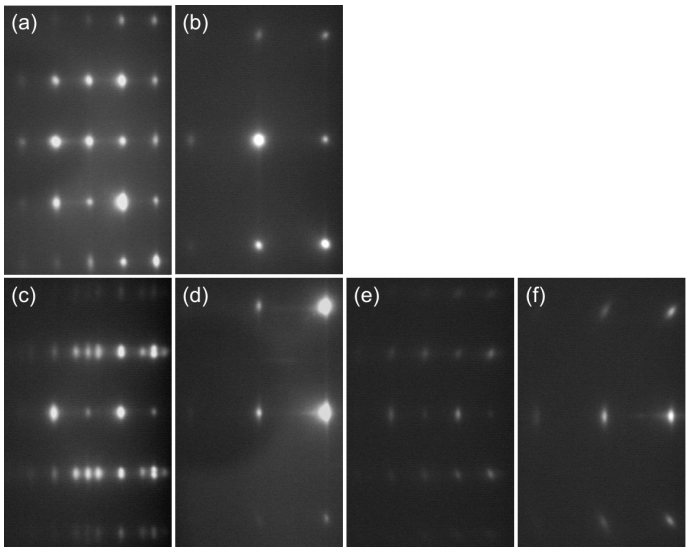

Figure 3.8: RHEED diffraction patterns for WZ NWs along (a) the [0112] direction and (b) the [0110] direction, for ZB NWs along (c) the [011] direction and (d) the [112] direction and for a ZB GaAs/GaMnAs core shell NWs along (e) the [011] direction and (f) the [112] direction, respectively.

If we compare the RHEED diffraction pattern with diffraction patterns from the textbook [117], we can draw the following conclusions. As can be seen in figure 3.9, the ratio N/L (1.587) in figure 3.9 (b) is very close to the ratio of M/N (1.633) in figure 3.9 (d) for the two equivalent crystal directions of ZB [112] and WZ [0110]. A distinction between the ZB and WZ crystal phase in these crystal directions is therefore not possible, which is also confirmed by [99]. The situation is different for the ZB [011] and WZ [0112] crystal directions. Here, the ratio of L/M for ZB (1.155) differs significantly from the WZ (0.55) crystal phase. Unfortunately, a pure ZB diffraction pattern was never observed in RHEED, even if TEM investigations revealed that the crystal structure of the investigated NWs was predominantly ZB.

The reason for this behavior is most likely the crystal phase mixing zone with alternating ZB and WZ segments below the tip of the ZB NWs (cf. chapter 4.2.5). The origin of the crystal phase mixing can be attributed to the growth termination procedure, which yields a decrease in Ga supersaturation of the catalyst droplet and thereby causes a change in the crystal structure. ZB NWs have the peculiarity that due to their special growth mode, they are very homogeneous is size. Assuming a high NW density, the diffraction pattern of the ZB NWs originates to large parts from the crystal phase mixing zone below the NW tips. As a consequence, a mixed WZ/ZB diffraction pattern (cf. figure 3.8 (c)) appears even if the NWs are predominantly ZB.

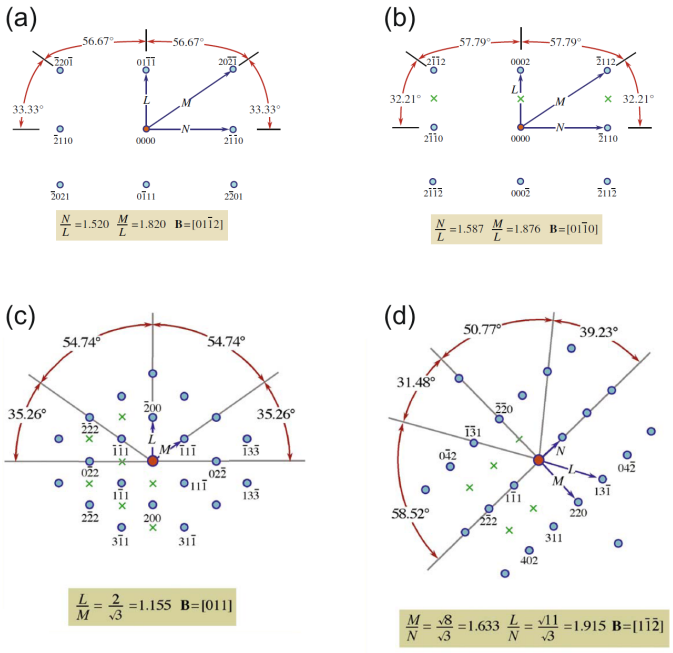

Figure 3.9: Diffraction pattern for WZ along (a) the [0112] direction and (b) the [0110] direction and for ZB along (c) the [011] direction and (d) the [112] direction, respectively. Taken from [117]. By rotating around 90°, figures 3.9 (a) and (b) are congruent with figures 3.8 (a) and (b).

We concluded that RHEED diffraction patterns cannot be utilized to distinguish between WZ and ZB NWs. However, RHEED can be used to investigate the crystal phase purity of the NWs. A mixture of WZ and ZB crystal structures shows up as a convolution of both diffraction patterns. The corresponding pattern, which was calculated in Ref. [99], is shown in figure 3.10. It is in agreement with the observed pattern in figure 3.8 (c) and can clearly be distinguished from a pure WZ diffraction pattern.

3.4 Post growth annealing oven

During the growth process, Mn is not only incorporated into the crystal on Ga sites but also as Mn interstitial defects. These defects can be reduced after the growth process by an annealing procedure. Therefore, the sample is heated to a temperature which is in the range of 50% to 95% of the growth temperature for several hours in air. At these conditions, the Mn interstitial defects become mobile and diffuse to the GaMnAs surface, where they react with oxygen to manganese oxide. The manganese oxide, unlike the Mn interstitial defects, has no negative influence on the

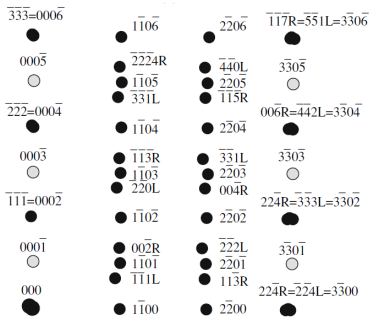

Figure 3.10: Calculated RHEED pattern of a mixed WZ/ZB crystal phase (the right upper quadrant is shown). By rotating around 90° the calculated RHEED pattern is congruent with the upper half of figure 3.8 (c). Taken from [99].

magnetic properties of the sample.

For the annealing of thin GaMnAs films, a hotplate annealing oven is used. Here, the samples are put on the hotplate and contacted with copper spires to monitor the change in sheet resistivity, which indicates the decrease of Mn interstitial defects. This setup works well for thin films but is not appropriate for the annealing of GaAs/GaMnAs core shell NWs, because the NWs show a cylindrical six fold cross section and an oxide shell in the order of several tens of nm. As a consequence of this symmetry, the part of the NW, which is in contact with the hot plate, is very small. A uniform temperature profile over the whole GaMnAs shell could therefore not be guaranteed. Additionally, the change in resistivity could not be monitored because the NWs cannot be contacted with the copper spires. As a consequence, a post growth annealing oven was developed which fits the special requirements of GaAs/GaMnAs core shell NWs.

To ensure that the whole NW is on the same temperature, a tube oven was built. The tube oven consists of a hot air fan, two concentric tubes and a sample holder as shown in figure 3.11. The hot air fan is attached to the top of the setup. From there, the hot air streams down the inner tube, heats the sample holder and flows through the openings on the bottom to the outer tube. In the outer tube, the hot air streams upwards, thereby heating the inner tube from the outside and escapes through the outlets on top. This setup ensures that the air in the lower part of the inner tube, which contains the sample holder, is always on a constant temperature. The small gap between the bottom of the outer tube and the frame of the oven thermally isolates the tubes and suppresses an unwanted heat transfer to the frame.

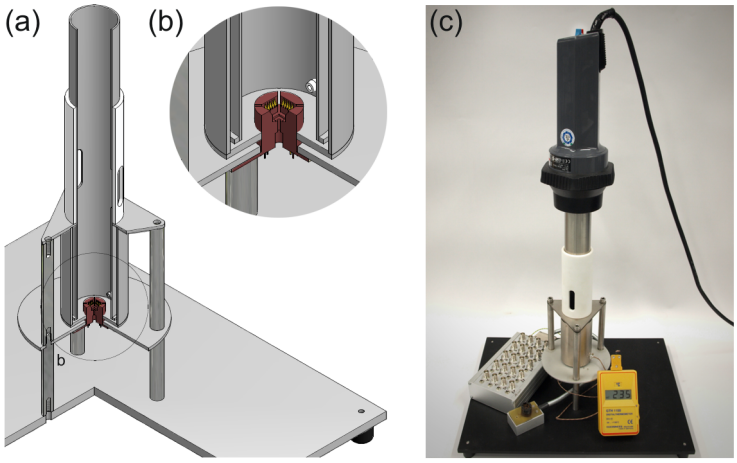

Figure 3.11: (a) Schematic drawing of the annealing oven. The hot air fan, not shown here, is mounted on top of the oven. (b) Blowup of the region around the sample holder. Here, the inner and outer tube, the feed-through for the thermocouple and the sample holder are shown. (c) Picture of the annealing oven with the hot air fan and the thermocouple.

3.5 Characterization Techniques

For the characterization of the grown samples, different methods were used. For the investigation of the NW morphology, the samples were characterized with scanning electron microscopy (SEM). To estimate the Curie temperature of 2D GaMnAs films, transport measurements were applied in a dewar based measurement setup. The NW crystal structure was examined by transmission electron microscopy (TEM) and magnetotransport measurements in a cryostat were used to estimate the magnetic properties of single NWs before and after annealing. Here, only the setup for SEM and transport on 2D GaMnAs films will be discussed because the TEM and single NW magnetotransport measurements were performed by the groups of Prof. Dr. Zweck and Prof. Dr. Weiss, respectively.

3.5.1 Scanning electron microscopy

For SEM investigations, the samples were cleaved with a scalpel in two ore more pieces and mounted on different SEM sample holders. One type of sample holder was used to take top view images of the NW samples. From these images, quantities like the droplet diameter, the NW- and cluster density could be derived. The second type of sample holder was used to take side view images of the samples. Here, the NW diameter and length as well as the NW tapering could be investigated.

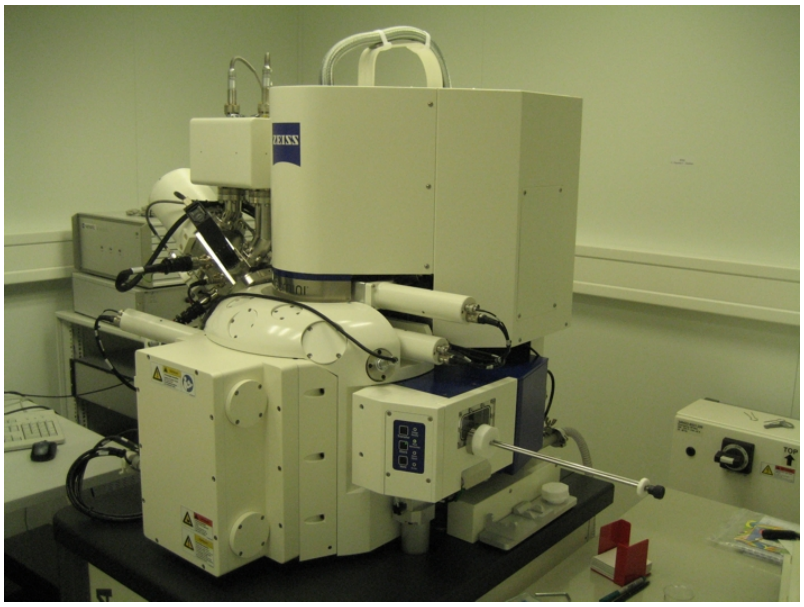

Figure 3.12: The Auriga SEM.

The SEM is a microscope which uses a beam of high energetic electrons to image the sample. The electrons are emitted from an electron gun, which is a field emission cathode in our case, and accelerated towards a ring anode. The energy of the electron beam is typically in the order of 1 to 30 keV. To focus the electron beam, condenser lenses are used. The spot size of the focused electron beam is of the order of several nm. To achieve spatial resolution, the focused electron beam has to scan the sample surface. The necessary deflection of the electrons is caused by scanning coils, which deflect the beam in x- and y-direction. To further improve the quality of the electron beam, several apertures are installed between the different coils. The whole SEM is evacuated to UHV in order to avoid scattering of the electrons with molecules from the gas phase. Figure 3.12 shows a picture of our Auriga SEM.

When the electron beam hits the sample surface, the electrons loose their energy as they are randomly scattered or absorbed by the sample material. As a result of the scattering events, some of the electrons are reflected from the sample. This process is known as elastic scattering of the primary electrons. Another part of the electron beam causes the emission of secondary electrons by inelastic scattering or the emission of electromagnetic radiation. Each of the emissions carries a special type of information. The reflected primary electrons and the high energetic electromagnetic radiance (X-rays) are very sensitive to the material contrast whereas the secondary electrons carry information about the sample surface. The primary and secondary electrons as well as the electromagnetic radiation can be collected by

special types of detectors. The signals are amplified and displayed on a cathode ray tube as variations in brightness. Due to the fact that the scanning of the cathode ray tube is synchronized with the scanning of the electron beam, the resulting SEM image is an intensity distribution map of the scanned sample. In modern SEMs, the signals are processed digitally and displayed on a computer monitor.

In order to tune the properties of the SEM pictures, the SEM user can adjust several basic quantities like the electron beam current, the electron beam energy and the working distance [39]. The beam current is regulated over apertures of different size. If a large aperture is used the number of electrons, which reach the sample, increases. As a consequence, also the signal intensity goes up. Due to enhanced Coulomb repulsion caused by the higher electron density, the electron beam is widened. This reduces the resolution of the SEM. The electron energy is regulated over the acceleration voltage, which is applied to the anode. A high electron energy reduces the number of electron scattering events and thereby the spot size of the electron beam. This is an advantage especially for e-beam lithography. Additionally, the penetration depth of the electrons increases. As a consequence, the electrons are scattered deeper inside or fully absorbed by the sample. This reduces the information content, which is obtained from the sample surface and the signal intensity. The working distance, which is the distance between the last lens and the sample, can be adjusted by moving the stage in z-direction. A large working distance enhances the distance in which the Coulomb repulsion can influence the electrons. This leads to a broadening of the electron beam. Additionally, the focus depth is increased, which makes it easier to obtain sharp pictures. A small working distance has the opposite effect.

To obtain high quality SEM images, an aperture of 30 μm was used. The acceleration voltage was set to values between 5 kV and 10 kV and the working distance was between 2 mm and 6 mm for side view and between 7 mm and 10 mm for top view images.

3.5.2 Transport measurements

For transport measurements, the samples were cleaved with the scalpel or a needle to a size of approximately 4x4 mm^2. To attach ohmic contacts to the GaMnAs films, small scratches were made on the edges of the samples, four in the corners and four on the flat sides. A thin gold wire was soldered to the scratches with an indium-zinc mixture (zinc content: 4-6%). The contacted sample was fixed in an eight pin chip carrier using vacuum grease. Finally, the open ends of the gold wires were soldered to the chip carrier pins with pure indium.

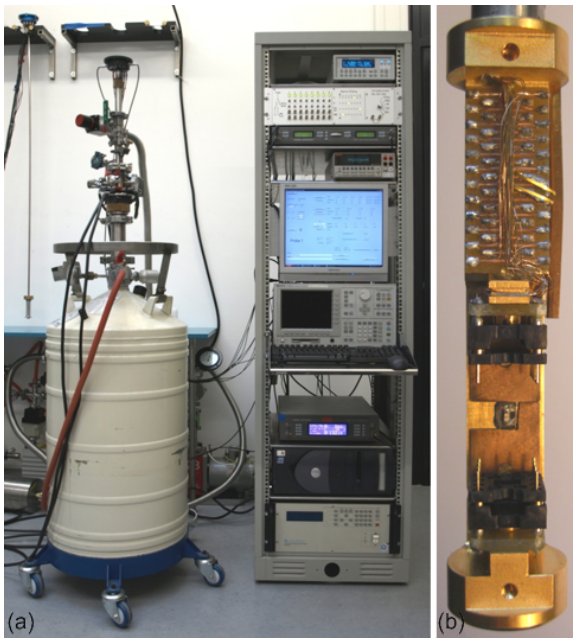

Figure 3.13: (a) The dewar setup, in the left upper corner also a measuring stick is visible. (b) The lower part of the measuring stick with the sample holder sockets and the temperature diode.

The transport measurement on GaMnAs films were carried out on our dewar measurement setup. The dewar measurement setup consists of a vacuum isolated storage vessel for liquid helium, a magnet measuring stick, a sample stick and a rack which contains the measuring instruments. The magnet stick is equipped with a superconducting coil which can provide a magnetic field up to six Tesla. Furthermore, the magnet stick has a separated sample chamber which can be filled with liquid helium via a needle valve. The sample stick provides a light emitting diode, a diode for temperature measurements and the sample socket. For the measurement of the contact and sheet resistivity as well as for the determination of the Currie temperature, a lock in amplifier, a voltmeter and the diode for temperature measurements were used. Figure 3.13 (a) shows a photograph of the whole measurement setup, figure 3.13 (b) show the lower part of the sample stick.
For the estimation of the Currie temperature, the magnet measuring stick is inserted slowly into the helium dewar. The sample stick is inserted into the magnet measuring stick, until the sample is in contact with the liquid helium in the sample chamber. Next, the sample stick is pulled out of the magnet measuring stick very slowly. This leads to a uniform increase in sample temperature from 4 K to room temperature. The resistivity of the sample is measured during the warm up process.
We like to add that that the sample stick can also be introduced into the helium dewar without the magnet measuring stick. The advantage of this modus operandi is

that the amount of helium, which is evaporated during the measurement procedure, is much smaller compared to the case when the magnet measuring stick is used. However, the warm up of the sample is not so well controlled, because the sample is in contact with the whole helium bath of the dewar and not only with the helium bath of the sample chamber of the magnet measuring stick. As a consequence, the obtained warm up curves look much better if the magnet measuring stick is used. The temperature-resistivity curves can also be acquired during the cool down process of the sample instead of during the warm up process. For this case the obtained T_C value is always too high, because the sample, which is mounted below the temperature diode on the sample stick, is always at a lower temperature than the temperature diode. This can be confirmed by replacing the sample by another temperature diode or by measuring T_C of the sample with a SQUID. Therefore the use of the magnet measuring stick during the warm up procedure is strongly recommended for the estimation of the Currie temperature.

Chapter 4

The Au technique: Morphology and crystal structure of GaAs NWs

In this chapter the results achieved with the Au technique will be presented. For the Au technique, a substrate covered with a thin Au layer is used. During oxide desorption, the Au layer comes in contact with the GaAs substrate and Au/Ga droplets are formed. The Au/Ga droplets work as catalysts for NW growth. The subject of our investigation is the morphology and the crystal structure of GaAs NWs.
In the first part of this chapter, different growth parameters and their influence on the NW morphology will be investigated. The obtained results provide the knowledge for the tuning of the NW morphology and reveal that also a tuning of the NW crystal structure from pure WZ to pure ZB is possible.
In the second part of this chapter, the conditions for the tuning of the NW crystal structure are systematically investigated. The Ga concentration in the catalyst droplet is found to be the crucial parameter for the appearance of the WZ or ZB crystal phase. These findings are used to grow NW with a distinct crystal structure.
In the third part of this chapter, the position controlled growth of Au catalyzed NWs is examined. NW crystal phase control for all NWs on one sample can only be achieved if all catalyst droplets have the same Au/Ga ratio. Therefore, uniform Au discs are fabricated on GaAs and Si substrates in a gird like pattern. The equal distances between the Au discs ensure that the incoming material from the effusion cells is equally distributed under all NWs.

4.1 Morphology of GaAs nanowires

To tune the morphology of the NWs, different sample series were grown where only one parameter was changed while the other parameters were kept constant. In this thesis, the influence of the Au layer thickness, the oxide desorption procedure, the surface treatment procedure, the growth temperature, the total As_4 and Ga fluxes and the As_x/Ga beam equivalent pressure ratio [52], short As_x/Ga ratio for the As_2 as well as for the As_4 species on the NW morphology were systematically investigated. Due to the fact that the investigations on the oxide desorption procedure and the surface treatment procedure are of technical nature and do not provide further insight into the physics of NW growth, both topics are discussed in the appendix. The investigations of the As_2/Ga ratios are also shifted to the appendix because the obtained results did not contribute to the purpose of this chapter, which is the evaluation of the crucial parameters for the formation of the WZ or ZB crystal phase. Unless otherwise stated, a Ga flux of 0.8 Å/s, an As_4 pressure of 1.2×10^{-6} Torr and a growth temperature of 540°C were used for NW growth, which we will refer to as standard growth parameters. The amount of Ga deposited on the substrate is equivalent to a 600 nm thick 2D GaAs layer. While most of the Ga is used for the formation of regular NWs, a certain amount is used for the formation of very long and inhomogeneous NWs, called whiskers. Besides that, also the formation of a parasitic two dimensional (2D) GaAs layer on the GaAs substrate is observed. The numbers for the NW density is obtained from a top view SEM image by counting all NWs in a 3x3 μm^2 area. For the estimation of the NW length, diameter and tapering ten NWs are evaluated from SEM side view images, which is a sufficient number for a qualitative analysis. Tapering means the ratio between the diameter at the tip of the NW and the diameter at the foot of the NW. The contact angle β of the catalyst droplet is the angle between the NW-droplet boundary and the catalyst droplet. The number for the fraction of small NWs is derived by counting all NWs from one SEM side view image and dividing the number of small NWs by the total number of NWs. Here, small NWs are NWs below 1 μm in length which have a proper shape and an intact catalyst droplet. To address a certain NW sample, the sample number, which consists of a C (for C-chamber) and the date of growth or the crucial sample parameter are used, depending on the context.

4.1.1 Influence of the Au layer thickness

For the investigation of the Au layer thickness seven samples with different Au layer thicknesses were prepared. The samples with 0.5 Å, 1 Å, 1.5 Å and 3 Å Au were

Sample number	C101011A		C100308A		C090514A	C090728B	C090423A
Au layer thickness [Å]	0.5	1	1.5	3	5	10	18
NW density [μm^{-2}]	12	8	9.5	8	14.5	16	7
NW length [μm]	2.4	2.6	2.5	2.9	1.7	2.9	2.7
Standard dev. [μm]	0.3	0.7	0.5	0.8	0.4	0.4	0.5
NW diameter [nm]	44	53	46	58	50	50	55
Standard dev. [nm]	11	10	11	13	22	11	6
Small NWs [norm.]	0	0	0	0	0	0.38	0.62

Table 4.1: NW properties with respect to the Au layer thickness. The NW density and the size of the long NWs is almost independent of the Au layer thickness. The fraction of small NWs increases with increasing Au layer thickness.

fabricated in the metal MBE system of Prof. Back in Regensburg. The samples with 5 Å, 10 Å and 18 Å Au were provided by A. Petroutchik and L. T. Baczewski from the Institute of Physics, Warsaw. The NW samples with 0.5 Å and 1 Å as well as the NW samples with 1.5 Å and 3 Å Au layer thickness were mounted on the same sample holder during one growth run, respectively. The NWs were grown using the the standard growth parameters. The results are summarized in table 4.1.

As can be seen from table 4.1, the NW density is from the same order of magnitude for all samples and varies at most by a factor of two, while the Au layer thickness varies by a factor of 36 for the thinnest and the thickest Au layer. Also the NW length and diameter are very close together for the samples with 0.5 Å to 3 Å Au and an influence of the Au layer thickness is not measurable. In case of thicker Au layers the appearance of small NWs can be observed. The small NWs have a length below 1 μm and a diameter larger than 100 nm. NWs with this size can also be observed on samples with an Au layer thickness smaller than 3 Å, however their appearance can be ascribed to irregularities during growth, resulting in crooked NWs which are very inhomogeneous in morphology. In contrast, the small NWs of the samples with an Au layer thickness larger than 3 Å are very homogeneous in size. Their fraction is increasing with increasing Au layer thickness as illustrated in figure 4.1.

We conclude that the variance in NW density is not correlated with the Au layer thickness. The observed variance can be explained by the statistical nature of the droplet formation, where parameters like the surface roughening of the GaAs substrate and the homogeneity of the Au layer come into play. Both parameters can be different for different substrates and different metal MBE systems. Instead of an increase in Au/Ga droplet density, an increase in size and presumably in the Au concentration of the catalyst droplets was observed for increasing Au layer thicknesses.

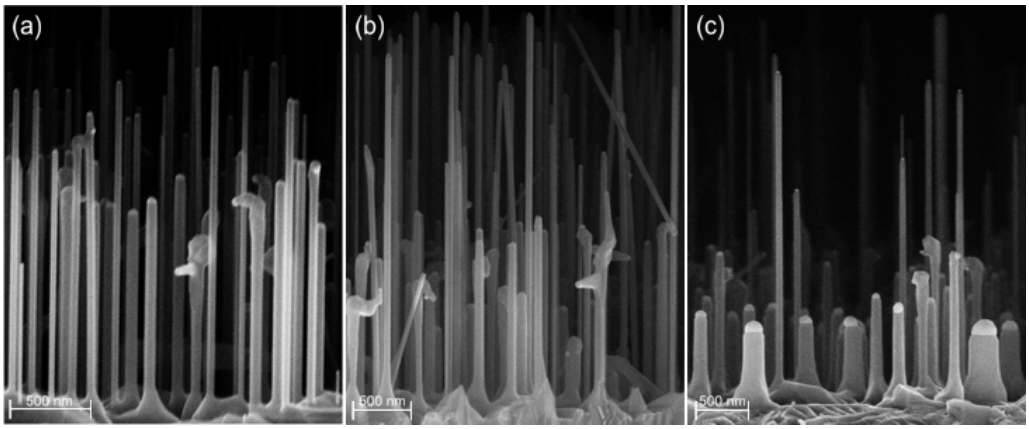

Figure 4.1: SEM side view images of (a) sample C090514A (5 Å Au), (b) sample C090728B (10 Å Au) and (c) sample C090423A (18 Å Au). The ratio of small and thick NWs increases with increasing Au layer thickness.

The increase in droplet size results in an increased number of thick and small NWs while the increase in Au concentration promotes a change in NW crystal structure. While ZB segments can be found in the WZ crystal matrix for NWs grown with a thin Au layer, the NW crystal structure is pure WZ for the short NWs grown with a thick Au layer. This indicates that according to chapter 2.1.3, the chemical potential of the catalyst droplet and thereby the NW crystal structure can be changed by changing the Au layer thickness.

4.1.2 Influence of the growth temperature

For the investigation of the growth temperature five samples were studied. The samples were grown at approximately 510°C, 520°C, 530°C, 540°C and 580°C. Standard material fluxes were used for NW growth, the equivalent amount of Ga deposited on the substrate was reduced to 150 nm 2D GaAs. For sample C080902A (530°C) the material fluxes were doubled, yielding the same As_4/Ga ratio as the other samples. The applied growth temperatures as well as the statistical evaluation of the NW samples are summarized in table 4.2.
At 583°C the NW growth is almost completely suppressed and only catalyst droplets can be found on the GaAs substrate. From theory ([23], see chapter 2.1.2) we know that the growth rate of GaAs NWs is temperature dependent. At a certain growth temperature the growth rate below the catalyst droplet equals the growth rate of the substrate and the formation of NWs is suppressed. For GaAs NWs with a diameter of 80 nm the maximum growth temperature is predicted to be 670°C. For our setup the temperature threshold value is obviously much lower. To ensure that 580°C is

Sample number	C080901B	C080827A	C080902A	C080901A	C080827B
Growth T [°C]	512	520	532	541	583
NW density [μm^{-2}]	12	8	9.5	8	-
NW length [nm]	600	374	(1406)	206	-
Standard dev. [nm]	415	161	(920)	66	-
NW diameter [nm]	41	48	(54)	68	-
Standard dev. [nm]	21	15	(21)	21	-

Table 4.2: Influence of the NW growth temperature on the NW morphology. Sample C080902A (T_{growth}=532° C) was grown with different total material fluxes and is therefore not comparable with the other samples. The best NW homogeneity is achieved at 540° C, the maximum growth temperature for Au assisted NW growth is approximately 580° C.

the upper limit for the growth of GaAs NWs in our MBE system, another sample (C100317B) was grown at 572°C. This sample is not listed in table 4.2 as the used substrate and the applied growth parameters (Ga flux: 0.8 Å/s, equivalent amount of Ga: 600 nm), differ from the other samples. However, C100317B showed a normal NW morphology for the used substrate and growth parameters which implies that 580°C is the upper limit for Au catalyzed GaAs NW growth in our MBE system.
After evaluating the maximum growth temperature, we want to find the growth temperature which gives the most homogeneous NW samples. Theory [23] predicts suitable growth rates in the temperature regime between 470°C and 610°C, with a growth rate maximum at 550°C. As we found in the previous investigation that 580°C is the upper limit for NW growth in our MBE system at our standard growth parameters, we focus our investigations on the temperature regime between 510°C and 540°C. For the statistical analysis, we have to exclude sample C080902A (530°C) due to its higher material fluxes and higher equivalent amount of 2D GaAs, which was 300 nm.
From table 4.2 we see that the NW length as well as the fluctuation in NW length is decreasing while the NW diameter is increasing with increasing growth temperature. The decrease in NW length fluctuation leads to a more homogeneous NW morphology. The best NW homogeneity was reached for a growth temperature of 540°C. Therefore, this growth temperature was used for further experiments.

4.1.3 Influence of the total As_4 and Ga fluxes

For this experiment, the Ga flux was increased in three steps from 0.6 Å/s to 0.8 Å/s and finally to 1 Å/s while the As_4 pressure was adjusted in a way that the As_4/Ga ratio was 1.7 for all samples. The NWs were grown on a substrate with 18 Å Au,

Sample number	C090423B	C090423A	C090416A
Ga rate [Å/s]	0.58	0.79	1
As pressure [10^{-6} Torr]	0.85	1.16	1.47
As_4/Ga ratio	1.7	1.7	1.7
NW density [μm^{-2}]	6	7	5
NW length (long NWs) [μm]	2.6	3.0	3.4
Standard dev. [μm]	0.4	0.5	0.3
NW diameter (long NWs) [nm]	45	57	58
Standard dev. [nm]	12	9	7
NW length (short NWs) [μm]	0.8	0.8	0.8
Standard dev. [μm]	0.15	0.13	0.16
NW diameter (short NWs) [nm]	142	155	136
Standard dev. [nm]	27	48	47
Small NWs [norm.]	0.65	0.61	0.50

Table 4.3: NW properties with respect to the total As_4 and Ga fluxes. The NW length increases and the fraction of small NWs decreases with increasing Ga and As_4 fluxes.

yielding a large number of small NWs. The results of this investigation are summarized in table 4.3.

The increase in total fluxes is not changing the NW density, but the number of small NWs is decreasing for increasing total fluxes. The size, i.e. the length and diameter of the small NWs is not significantly affected by the change in total fluxes, indicating that they are cut off from the material supply as the surrounding long NWs collect the incoming material over the side facets. Unlike the short NWs, the long NWs are affected by the change in total fluxes which is revealed by the increase in NW length and diameter with increasing total fluxes. This shows that the NW growth rate increases with increasing material fluxes at a constant As_4/Ga ratio. As the amount of deposited Ga was constant for all samples, the increase in NW size has to be accompanied by a reduction in parasitic 2D layer growth. This is reasonable because the faster nucleation at the NW-droplet boundary, which is caused by the higher total As_4 pressure, yields a reduction of the catalyst droplet supersaturation. As a consequence, the difference in chemical potential between the adatoms on the GaAs substrate and the catalyst droplet increases, which leads to an increased Ga diffusion to the catalyst droplet and a decreased Ga nucleation rate on the GaAs substrate. To verify this assumption, samples with different As_4/Ga ratios at a constant Ga flux are investigated.

Sample number	C090218B	C090416B	C090304A
Ga rate [Å/s]	1.06	1.00	1.13
As pressure [10^{-6} Torr]	0.65	1.18	2.07
As_4/Ga ratio	0.7	1.4	2.2
NW density [μm^{-2}]	<1	5	8.5
Tapering [norm.]	1.4	0.9	0.9
NW length (long NWs) [μm]	-	2.9	3.1
Standard dev. [μm]	-	0.5	0.5
NW diameter (long NWs) [nm]	-	59	76
Standard dev. [nm]	-	10	16
NW length (short NWs) [μm]	1.1	0.7	0.8
Standard dev. [μm]	0.06	0.05	0.1
NW diameter (short NWs) [nm]	106	160	117
Standard dev. [nm]	12	25	23
Small NWs [norm.]	1	0.64	0.35

Table 4.4: NW properties with respect to the As_4/Ga ratio. The NW length and the NW diameter increases while the NW tapering decreases with increasing As_4 pressure.

4.1.4 Influence of the As_4/Ga ratio

For this series of samples, the Ga flux was kept constant at 1 Å/s and the As_4 pressure was varied in three steps, yielding an As_4/Ga ratio of 0.7, 1.4 and 2.1. It has to be noted that the sample with an As_4/Ga ratio of 1.4 was grown on a substrate with 10 Å Au while the other two samples were grown on a substrate with 18 Å Au. Therefore we will not discuss the NW density of the three samples as this quantity depends on the used substrates. The other quantities are in good approximation independent of the Au layer thickness and can be evaluated. The results are summarized in table 4.4.

As a consequence of the low As_4/Ga ratio Ga puddles with a diameter of 1-2 μm can be observed on the substrate of the sample with an As_4/Ga ratio of 0.7 in top view SEM images. The NWs are short, extremely homogeneous in size and inversely tapered, which means that the diameter at the top of the NWs is larger than the diameter at the bottom of the NWs. All NWs show a hexagonal cross section with a large catalyst droplet. The contact angle β of the droplets is about 120°. The Ga puddles disappear for the sample with an As_4/Ga ratio of 1.4. Despite the fact that long and thin NWs can be found, the ratio of small NWs is still large. In contrast to the short NWs of the sample with an As_4/Ga ratio of 0.7, here the short NWs are not tapered, their cross sections are hexagonal and polygonal and the contact

angle β of the catalyst droplet is close to 90°. On the sample with an As_4/Ga ratio of 2.2 the amount and also the diameter of the long NWs is increased compared to the sample with an As_4/Ga ratio of 1.4. The NW size distribution is broader than the NW size distribution of the other two samples.

The increase in droplet size, contact angle β and tapering of the sample with an As_4/Ga ratio of 0.7 is attributed to the small As_4/Ga ratio, which leads to an increasing Ga concentration in the catalyst droplet during NW growth. The observed NW crystal structure is pure ZB with stacking faults [98]. This indicates that according to chapter 2.1.3, the chemical potential of the catalyst droplet and as a consequence the NW crystal structure can be changed by changing the As_4/Ga ratio and thereby the effective Ga supply of the catalyst droplet. The increasing amount of long NWs as well as the increase in NW length with increasing As_4 pressure at a constant Ga rate explicitly shows that the NW growth rate is determined by the As_4 pressure and not by the Ga flux. The increase in NW length, which was found in the section above can now definitely be assigned to the increase in As_4 pressure. This result is in agreement with the observations made by Glas et al. [38] in 2010.

4.1.5 Conclusion

In this chapter we investigated the influence of the Au layer thickness, the growth temperature, the total As_4 and Ga fluxes and the As_4/Ga ratio on the NW morphology. We found that the Au layer thickness did not systematically influence the catalyst droplet density. The formation of bigger catalyst droplets with a presumably increased Au concentration was observed for increasing Au layers thicknesses. The appearance of NWs with pure WZ crystal structure on substrates with a thick Au layer is attributed to the presumably increased Au concentration in the catalyst droplets. By investigating different growth temperatures between 510°C and 580°C we found that the best growth temperature with respect to the NW homogeneity was 540°C and the maximum growth temperature for the applied As_4 and Ga fluxes was 580°C. The investigation of the total As_4 and Ga fluxes at constant As_4/Ga ratio showed that an increase in Ga and As_4 fluxes leads to a proportional increase in NW size. The investigation of different As_4/Ga ratios at a fixed Ga rate showed that NW growth is As_4 determined as an increase in As_4 pressure leads to an increase in NW length. For a very low As_4/Ga ratio of 0.7 the formation of NWs with pure ZB crystal structure was observed. This observation is attributed to an increased Ga concentration in the catalyst droplet.

4.2 Crystal structure of GaAs nanowires

We know from nucleation theory (cf. chapter 2.1.3) that the NW crystal structure depends on the supersaturation of the catalyst droplet. However, it is not clear how the growth parameters have to be adjusted to obtain a certain supersaturation value. TEM investigations of different NW samples indicate that a broad range of the droplet supersaturation is accessible if certain growth conditions are met. For example, energy disperse x-ray spectroscopy (EDX) measurements of short and thick NWs, which preferentially grow on substrates with a large Au layer thickness, show that the catalyst droplets contain a large amount of Au while TEM diffraction patterns indicate that the crystal structure of these NWs is pure WZ. In contrast NWs, which were grown with an As_4/Ga ratio of 0.7 reveal catalyst droplets which contain nearly pure Ga while TEM diffraction patterns indicate that the crystal structure of these NWs is pure ZB. These observations prove that pure WZ and pure ZB NWs can be grown with the Au catalyst technique. To find the crucial growth parameters, a quantitative investigation of the catalyst droplet composition and the crystal structure of the corresponding NWs was needed. This investigation, which was performed in close cooperation and under the direction of Marcello Soda will be subject of the following chapter. The findings of this analysis will be used to grow NWs with a distinct crystal phase.

4.2.1 TEM analysis of the catalyst droplet and NWD ratio

In a TEM post growth analysis of five different NW samples (cf. table 4.5) we observe that the catalyst droplets and the tips of the NWs can have significantly different shapes, even for NWs originating from the same sample. In figure 4.2 TEM images of the tips of four different NWs are depicted originating from sample A (figure 4.2 (a/b)), sample D (figure 4.2 (c)) and sample E (figure 4.2 (d)). The catalyst droplet diameter either equals approximately the diameter of the NW or is smaller in size. Only for very Ga-rich growth conditions (sample E) a phase separation during growth termination can be observed leaving a small Au/Ga droplet within a large Ga droplet (figure 4.2 (d)).

It is commonly accepted that during growth the size of the catalyst droplet equals at least the size of the NW. We attribute the reduced size of the post growth catalyst droplet to a partial incorporation of Ga dissolved in the catalyst droplet into the NW crystal during growth termination [41]. Since for all samples the As_4 cell is kept open until the substrate temperature cools down below 400°C and since Ga is present in the catalyst droplet as well as on the side facets of the NWs, NW

Sample	Au layer [Å]	As_4 flux [10^{-6} Torr]	Ga rate [Å/s]	As_4/Ga ratio	Temp. [°C]
A	10	1.28	0.38	3.90	534
B	10	2.07	1.13	2.20	540
C	10	1.22	0.85	1.70	534
D	1.5	1.21	0.80	1.77	539
E	10	0.65	1.06	0.70	543

Table 4.5: Au layer thickness and the applied growth parameters for sample A to E. The growth temperature was kept constant at approximately 540° C.

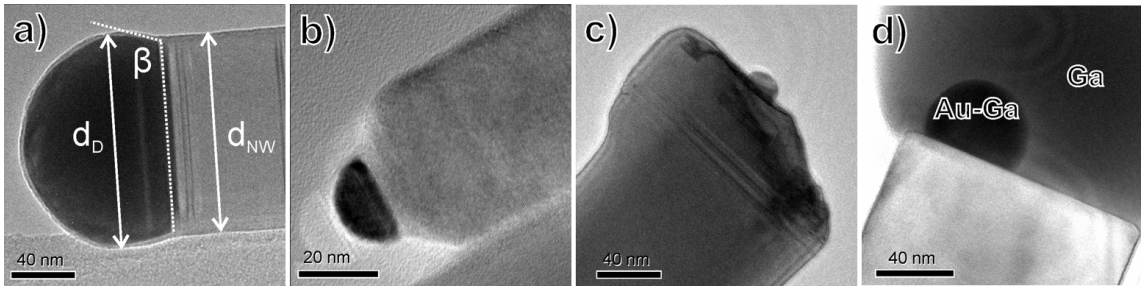

Figure 4.2: TEM images of the tips of four different NWs. The diameter of the post growth catalyst droplet, d_D, either equals the diameter of the NW d_{NW} (a), or is considerably smaller in size ((b) and (c)). For very Ga rich growth conditions a phase separation within the catalyst droplet can be observed (d). The NWs shown in (a) and (b) are from sample A, whereas the NWs in (c) and (d) are from sample D and sample E, respectively. Taken from [98].

growth can continue until the As_4 supply is stopped or the substrate temperature decreases below a critical value. EDX measurements (not shown) prove that only Ga is incorporated as no measurable amount of Au is detected in the NW close to the catalyst droplet. Due to the shrinking catalyst volume during growth termination, the NWs exhibit a characteristic tapered shape (cf. figure 4.2 (b)). In literature this specific form of the tip of the NW is often referred to as cooling neck [82, 84].
To quantitatively describe how strongly this cooling neck is developed, we introduce the NWD ratio, defined as

$$\text{NWD ratio} = (d_{NW} - d_D)/d_{NW} \tag{4.1}$$

with d_{NW} and d_D as the diameter of the NW and of the post growth catalyst droplet, respectively. In figure 4.2 (a) the NW diameter d_{NW} as well as the post growth catalyst diameter d_D and the post growth contact angle β is sketched. As

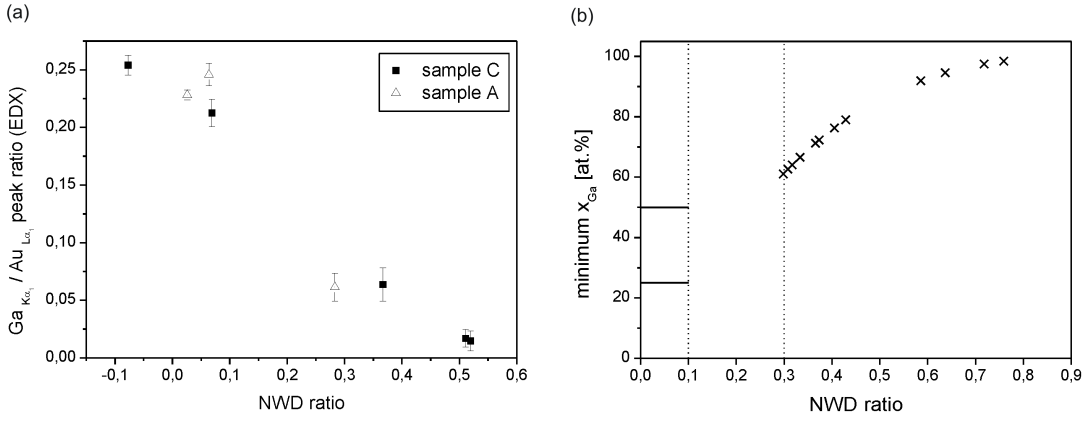

Figure 4.3: (a) EDX Ga/Au peak ratio of the post growth catalyst droplet. NWs with a NWD ratio ≥ 0.3 show a lower Ga/Au peak ratio compared to NWs with a NWD ratio <0.1. (b) Ga concentration of the catalyst droplet ***during*** *growth. Solid lines are values taken from literature, crosses give a lower boundary for the Ga concentration calculated for experimentally observed NWD ratios. Taken from [98].*

here the contact angle is slightly larger than 90°, the NWD ratio of -0.07 is negative. The NWs shown in figure 4.2 (b) and 4.2 (c) exhibit NWD ratios of 0.48 and 0.84, respectively.

With EDX we study the chemical composition of the post growth catalyst droplets. In figure 4.3 (a) the ratio of the Ga_{K_α} and the Au_{L_α} peak is plotted versus the NWD ratio for different NWs originating from sample A and sample C. Interestingly, the data points are distributed into two regions. NWs with a NWD ratio < 0.1 exhibit a significantly higher Ga/Au peak ratio than NWs with a NWD ratio ≥ 0.3. Or in other words, for NWs which show a pronounced cooling neck (cf. figure 4.2 (c/b)) the Ga concentration of the post growth catalyst is smaller than for NWs whose catalyst droplet volume does not change significantly (cf. figure 4.2 (a)). From the correlation between the Ga/Au peak and the NWD ratio we deduce the following: For NWs with NWD < 0.1 the post growth catalyst droplet contains approximately the amount of Ga as during growth. In contrast, for NWs with NWD ≥ 0.3 the Ga concentration of the catalyst droplet was larger during growth than in the probed post growth analysis. The EDX measurements thus support the picture of the (partial) incorporation of Ga stemming from the catalyst droplet during growth termination. Note that the obtained values for the Au/Ga ratio by EDX are not an absolute measure because the element and TEM specific Cliff-Lorimer factors, which are needed for the determination of the absolute concentration, are affected by large errors and were therefore not utilized. However, for our study the comparison of the uncorrected Au/Ga peak ratio is sufficient.

4.2.2 Relating the NWD ratio to the droplet composition

For the formation of a distinct crystal phase of the NWs the essential parameter is the Ga concentration, x_{Ga}, of the catalyst droplet *during* NW growth. As we will show, the NWD ratio is linked to the Ga concentration of the catalyst droplet during growth. From the post growth EDX (cf. figure 4.3 (a)) and TEM analysis we estimate x_{Ga} as follows:
For NWs with NWD < 0.1, as we cannot extract absolute Ga concentrations from the EDX measurements, we have to go back to values from literature. From the binary Au-Ga phase diagram a theoretical lower boundary of ≈ 25 at.% can be derived as only for Ga concentrations higher than 25 at.% the AuGa alloy is liquid at typical NW growth temperatures [9]. Calculations of the Au-Ga-As ternary phase diagram at a low pressure of 10^{-5} bar and a temperature of 590°C show that the As concentration within the catalyst droplet is negligible with an As concentration lower than 0.2 at.% for Ga concentration higher than 30 at.% [9]. To our knowledge the only experimentally obtained Ga concentrations are reported by Harmand et al. who determined Ga concentrations of 0.37 and 0.50 of the catalyst droplet using an abrupt growth termination process [41].
To obtain a lower boundary of x_{Ga} for NWs with NWD ≥ 0.3 we use the following assumptions. The shape of the catalyst droplet is assumed to be hemispherical. The post growth catalyst droplet is supposed to have no Ga or As contributions. The number of Au atoms in the catalyst droplet can then be calculated from the volume of the post growth catalyst. During growth a contact angle of 90° is considered, i.e. the volume of the AuGa catalyst during growth is determined by the nanowire diameter - giving a lower boundary for the estimated Ga concentration. From the difference of both volumes the number of Ga atoms and hence the Ga concentration can be calculated.
In figure 4.3 (b) the results of our estimate are summarized. For NWs with NWD < 0.1 values from literature are drawn as solid lines giving a lower and upper boundary. For NWs with NWD > 0.3 the calculated minimum x_{Ga} value increases with increasing NWD ratio from approximately 60 at.% at a NWD ratio 0.3 to values larger than 90 at.% for NWD ratios larger than 0.6.

4.2.3 Relating droplet composition to NW crystal structure

We investigated 22 NWs originating from samples A-D (cf. table 4.5). The crystal structure of the NWs was determined by analyzing TEM diffraction patterns. All investigated NWs were scanned taking TEM diffraction patterns along their entire length. For a detailed explanation of the diffraction pattern analysis see [98]. The

dominant crystal structure of all NWs is the WZ crystal phase. The NWs are divided in two classes, pure WZ NWs (WZ) and NWs which show both crystal structures (WZ+ZB). The NWs are classified according to the observed diffraction patterns. Only if a mixed diffraction pattern was observed, HRTEM images were taken to clarify if a high density of stacking faults or if segments of ZB crystal structure are present. If the observed ZB segments consists of at least 7 monolayers which corresponds to a length of approximately ≥ 2 nm, the NWs are labeled as (WZ+ZB). Otherwise they are assigned to (WZ) NWs.

Our analysis shows that the number of NWs with a NWD ratio smaller than 0.2 crystallize in pure WZ crystal structure. There exists an intermediate regime ($0.2 \leq$ NWD ratio ≤ 0.4) where (WZ) as well as (WZ+ZB) NWs are observed. For NWD ratios higher than 0.4 all NWs form ZB segments.

Comparing the estimated Ga concentrations (figure 4.3 (b)) with the observed crystal structure of the NWs we conclude that a high Ga concentration of the catalyst droplet during NW growth favors the formation of ZB segments. NWs with a NWD ratio larger than 0.4 - which corresponds to a Ga concentration higher than 75 at.% - exhibit ZB segments. Lower Ga concentrations leads to the formation of pure WZ NWs with NWD ratios smaller than 0.2. In the intermediate NWD ratio regime we observe (WZ) as well as (WZ+ZB) segments.

Our conclusion is supported by comparing the different NW samples (cf. table 4.5) which are grown with different As_4/Ga ratios. If we compare the data obtained within each NW sample, we observe the same trend. For sample A, grown with the highest As_4/Ga ratio of 3.9, only WZ NWs are detected. Decreasing the As_4/Ga ratio to more Ga-rich growth conditions increases the probability to find (WZ+ZB) NWs. For sample B (As_4/Ga ratio: 2.20) two out of four NWs are (WZ+ZB) and for sample C (As_4/Ga ratio: 1.70) two out of five NWs are (WZ+ZB). The very thin Au layer of 1.5 Å of sample D (instead of 10 Å for all other samples) leads probably to an enhanced Ga concentration of the catalyst droplets during catalyst formation as well as during growth resulting in the formation of only (WZ+ZB) NWs. In addition, calculations of the difference in formation enthalpy of the nucleus at different positions of the droplet-NW boundary, $\Delta\gamma$, support the experimental results [98]. In the next step, we will use these results to grow pure WZ and ZB NWs.

4.2.4 Wurtzite nanowires

To obtain NWs with a pure WZ crystal structure, a low Ga concentration in the catalyst droplet is needed. Therefore, a substrate with a thick Au layer of 10 Å and a

Sample number	C110225B	C110302B	C110328B	C110309B
Ga rate [Å/s]	0.4	0.4	0.4	0.4
As pressure [10^{-6} Torr]	3.0	4.53	6.95	9.74
As_4/Ga ratio	8.8	13.1	20.0	28.4
NW density [μm^{-2}]	7	10	10	10
Tapering [norm.]	0.8	0.7	0.7	0.2
NW length (long NWs) [μm]	3.0	3.2	6.6	5.6
Standard dev. [μm]	1.1	0.9	1.6	0.8
NW diameter (long NWs) [nm]	72	70	52	72
Standard dev. [nm]	11	17	11	10
NW length (short NWs) [μm]	1.0	0.8	0.5	0.7
Standard dev. [μm]	0.2	0.3	0.1	0.2
NW diameter (short NWs) [nm]	129	136	114	145
Standard dev. [nm]	28	15	27	32
Kinked NWs [norm.]	0.13	0.12	0.69	0.33

Table 4.6: Influence of the As_4/Ga ratio on the NW morphology. The fraction of kinked NWs was strongly increased for an As_4/Ga ratio of 20 and 28.4. Additionally, the NW tapering was very pronounced for an As_4/Ga ratio of 28.4.

low Ga flux of 0.4 Å/s was used. To find the best parameters, a series with different As_4 fluxes at high As_4/Ga ratios was grown. The results are summarized in table 4.6.

The NW length of the long NWs increases with increasing As_4/Ga ratio. At an As_4/Ga ratio of 20 a saturation of the NW growth rate is observed. A pronounced NW tapering is observed for high As_4/Ga ratios. Also the amount of kinked NWs is strongly increased for an As_4/Ga ratio of 20. The short NWs are not significantly affected by the change in As_4/Ga ratio. Their length and diameter is almost constant for all four samples.

The increased length of the long NWs with increasing As_4/Ga ratio is dedicated to the As_4 determined NW growth, which was discussed in chapter 4.1.4. At an As_4/Ga ratio of 20 the NW growth rate is limited by the available amount of Ga. The increased NW diameter at the lower part of the long NWs as well as the decreasing size of the NW tips with increasing As_4/Ga ratio is attributed to the reduced diffusion length of the Ga adatoms with increasing As_4 pressure. The strongly increased number of kinked NWs for an As_4/Ga ration of 20 is attributed to the high NW growth rate, which leads to the formation of crystal defects and thereby to the appearance of kinked NWs.

As the whisker density at an As_4/Ga ratio of 20 is very high, the samples with an

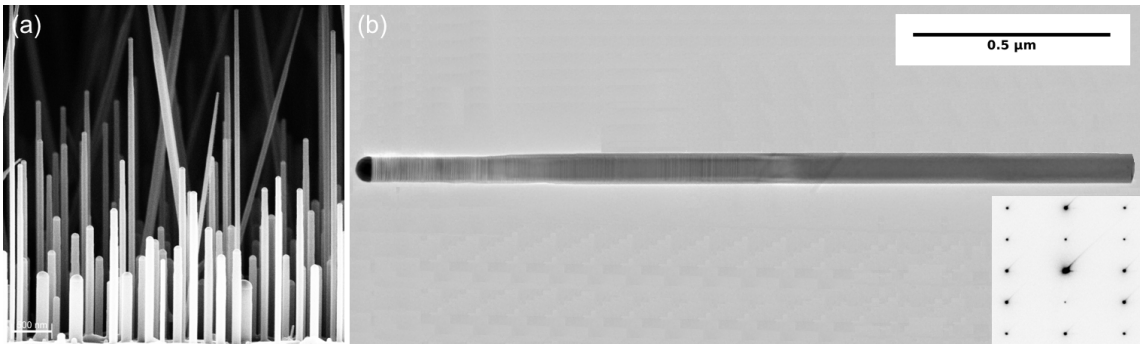

Figure 4.4: (a) SEM side view image of sample C110225B (As_4/Ga ratio 8.8), (b) TEM overview image of a single NW, the inset of (b) shows the corresponding TEM diffraction pattern for the WZ crystal structure.

As_4/Ga ratio of 20 and 28.8 are regarded as being not suitable for the fabrication of core shell NWs. Hence, only the samples with an As_4/Ga ratio of 8.8 and 13.1 were investigated with TEM to evaluate their crystal phase. It showed that the NWs of both samples are of pure WZ crystal structure with a high number of stacking faults. The stacking fault density was approximately 100 μm^{-1} along the whole NW for all investigated NWs of both samples. Due to the less pronounced tapering, an As_4/Ga ratio of 8.8 was chosen for the further fabrication of pure WZ NWs.

4.2.5 Zinc blende nanowires

To achieve NWs with a pure ZB crystal structure, a high Ga concentration in the catalyst droplet is needed. Therefore, a substrate with a very thin Au layer of 0.5 Å and small As_4/Ga ratios of 1.0 and 1.3 were used. To find the best parameters, a sample series with different Ga fluxes was grown. The results are summarized in table 4.7.

The NWs of all four samples are very homogeneous in size. The NW length and diameter is increasing at a fixed As_4/Ga ratio with increasing As_4 flux. The NWs of sample C110328A, C110217B and C110225A are inversely tapered and the catalyst droplets are clearly visible at the tip of the NWs. The NWs of sample C110302A are not tapered and the catalyst droplets are much smaller compared to the catalyst droplets of the other three samples. Ga puddles are visible on the substrate of sample C110328A and C110217B. Their size is decreasing from approximately 750 nm for sample C110328A to approximately 350 nm for sample C110217B.

The increase in NW length and diameter is again attributed to the increase in the total As_4 flux at a fixed As_4/Ga ratio (cf. chapter 4.1.3). The inversely tapering of the samples C110328A, C110217B and C110225A as well as the appearance of

Sample number	C110328A	C110217B	C110225A	C110302A
Ga rate [Å/s]	0.7	1.44	2.1	2.76
As pressure [10^{-6} Torr]	0.61	1.21	1.82	3.13
As_4/Ga ratio	1.0	1.0	1.0	1.3
NW density [μm^{-2}]	9	7	9	11
Tapering [norm.]	1.5	1.5	1.4	1.0
NW length [μm]	1.3	1.3	1.7	2.5
Standard dev. [μm]	0.1	0.1	0.2	0.35
NW diameter [nm]	63	79	66	61
Standard dev. [nm]	10	10	10	10
Kinked NWs [norm.]	0.18	0.10	0.14	0.09

Table 4.7: Influence of the total Ga flux on the NW morphology. Due to the pronounced inversely NW tapering for the samples with an As_4/Ga ratio of 1.0, the As_4/Ga ratio was increased to 1.3 for sample C110302A.

Ga puddles on the samples C110328A and C110217B originates from the small As_4/Ga ratio of 1.0. The decrease in size and number of the Ga puddles from sample C110328A to sample C110217B and their disappearance on sample C110225A is attributed to the increased Ga diffusion to the catalyst droplet with increasing As_4 pressure, as discussed in chapter 4.1.3 and to the sticking coefficient of As_4 on the GaAs substrate, which depends on the Ga rate [32]. To avoid the NW tapering, the As_4/Ga ratio was slightly increased to 1.3 for sample C110302A.

As the samples C110328A, C110217B and C110225A were grown with the same As_4/Ga ratio of 1.0, their crystal structure should be comparable. Therefore, only sample C110328A with an As_4/Ga ratio of 1.0 and sample C110302A with an As_4/Ga ratio of 1.3 were investigated with TEM. Both samples reveal predominantly ZB crystal structure. The investigated NWs of sample C110328A show (from NW top to NW bottom) a short segment of 30 nm ZB below the droplet, 60 nm with a high density of stacking faults (100 μm^{-1}), 100-200 nm with an increased number of stacking faults (50 μm^{-1}), approximately 1 μm with only a few twin defects and finally a region with an increased stacking fault density (50 μm^{-1}) at the foot of the NW. The three investigated NWs of sample C110302A show (from NW top to NW bottom) a short segment of 10-20 nm of ZB below the droplet, then approximately 300 nm of WZ crystal structure followed by a crystal mixing zone of approximately 500 nm with a high density of stacking faults. The rest of the NWs, approximately 2.2 μm, is pure ZB with a very low stacking fault density of approximately 4 μm^{-1}. The crystal mixing zone as well as the WZ segments are attributed to the growth

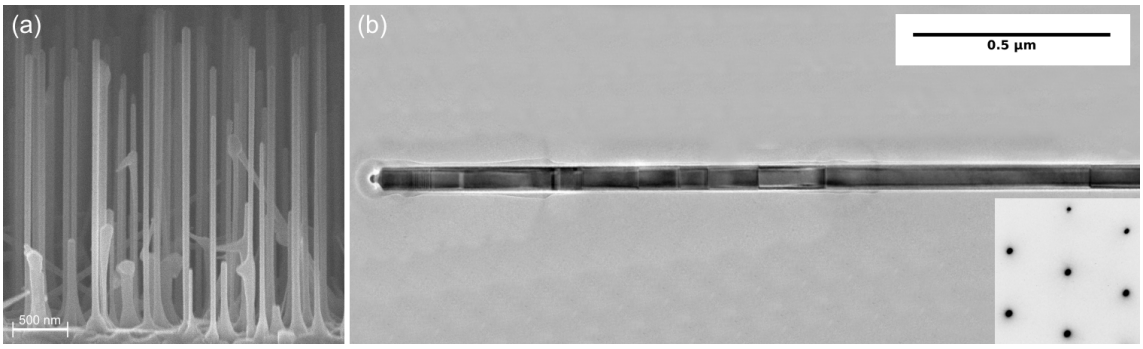

Figure 4.5: (a) SEM side view image of sample C110302A (As_4/Ga ratio 1.3), (b) TEM overview image of a single NW, the inset of figure 4.5 (b) shows the corresponding TEM diffraction pattern for the ZB crystal structure.

termination sequence, although the segments are very long compared to the relatively short growth termination procedure. As a consequence of the absence of tapering, Ga puddles and the good crystal quality, the growth parameters of sample C110302A were chosen for the further fabrication of ZB NWs.

4.2.6 Conclusion

In this chapter we investigated the correlation between the catalyst droplet composition and the NW crystal structure. First, the size and the composition of the catalyst droplet were evaluated by TEM and EDX. The ratio of the NW diameter and the droplet diameter, called NWD ratio was introduced to give a quantitative description of the droplet state after NW growth. From the size of the post growth catalyst droplet, the Ga concentration during growth was estimated either by referring to publications for NWs with a small NWD ratio or by calculations for NWs with a large NWD ratio. By comparing the NWD ratio with the crystal structure, the correlation between the catalyst droplet composition and the NW crystal structure could be revealed. It showed that a Ga concentration below 50 at.% leads to the formation of WZ NWs while a Ga concentration above 60 at.% favours the appearance of ZB segments in the WZ crystal matrix under the applied growth conditions.
The findings were used to grow NWs with a distinct crystal phase. For WZ NWs, which require a low Ga concentration in the catalyst droplet, a substrate with a thick Au layer of 10 Å, a small Ga flux of 0.4 Å/s and a high As_4/Ga ratio of at least 8.8 was used to keep the Ga concentration of the catalyst droplet below 50 at.%. For ZB NWs, which require a high Ga concentration in the catalyst droplet, a substrate with a very thin Au layer of 0.5 Å, a high Ga flux and a small As_4/Ga ratio of 1.0 or 1.3 was used to reach a Ga concentration of at least 60 at.%. As a consequence,

the ZB crystal phase is formed in a pseudo Ga catalyzed growth mode [98].
The crystal quality of the obtained NWs is not completely satisfying. The ZB NWs show a region with high density of stacking faults which is located in the upper third of the NWs. The origin of this stacking fault rich region is ascribed to the growth termination sequence. For WZ NWs, the stacking fault density in the whole NW is quite high. Here, the high stacking fault density is dedicated to the high As_4/Ga ratio, which favours the formation of crystal defects. To enhance the quality of the crystal structure, investigations of the growth termination procedure and the As_4/Ga ratio are recommended.

4.3 Position controlled growth of GaAs NWs

In chapter 4.2 we found that the NW crystal structure is determined by the ratio of Au and Ga in the catalyst droplet. The tuning of this ratio for a single catalyst droplet seems to be very difficult because the amount of Au, which is accumulated in the droplet, depends on local parameters like the Au layer thickness and the substrate surface roughening. These parameters are not necessarily constant over the whole sample. In addition, also the amount of accumulated Ga depends on the local surrounding of the catalyst droplet. If the droplet is surrounded by a high number of other droplets, the incoming Ga from the effusion cell is shared amongst the droplets and the Au/Ga ratio of each single droplet will be large. In contrast, if no other droplets are in the vicinity of the droplet, the incoming Ga from the effusion cell can be collected by the droplet alone and the Au/Ga ratio will be small. As a consequence, NWs with different crystal structures are observed on the same NW sample [97,98]. To achieve a uniform crystal structure for all NWs on the same sample, both, the amount of Au and the amount of Ga has to be well defined for each single catalyst droplet.

4.3.1 Pre-structuring of the substrates

To ensure an equal amount of Au in each droplet, Au discs with a uniform diameter and thickness were fabricated onto the sample substrate. The equal distribution of the incoming Ga from the effusion cell was guaranteed by arranging the Au discs in a grid like pattern with equal distances between the Au discs. For the growth on GaAs substrates, an e-beam resist layer was put on the substrate. Four hole grids with different hole diameters were fabricated on the resist layer by e-beam lithography. After developing, a 15 Å thick Au layer was evaporated on the hole grid mask using the metal MBE system of Professor Back. Next, the e-beam resist was removed by

a lift off process and the sample was chemically cleaned with Acetone and Propanol. Finally, Au discs with a diameter comparable to the diameter of the e-beam resist mask remain on the substrate. The catalyst droplets are formed when the sample is heated to oxide desorption temperature in the MBE system. An exact description of the sample preparation procedure can be found in [3].

For the growth on Si substrates, the procedure was slightly different. The Si substrates are covered by a thin thermal SiO_2 layer. Again, e-beam resist was put onto the SiO_2 layer and hole grids with different hole pitches were defined by e-beam lithography. After developing, the hole grid mask was transferred to the SiO_2 layer by wet chemical etching. Next, Au was sputtered onto the hole grid mask using the sputter system of Professor Weiss. After the lift off process, the samples were first cleaned in a plasma oven and then chemically with Acetone and Propanol. Finally, Au discs remain in the pre-defined holes of the SiO_2 layer. Before the sample was transferred to the MBE system, a HF dip was performed to remove any adhesions from the SiO_2 surface. At the beginning of the NW growth, the Au discs alloys with Ga from the effusion cells and Au/Ga catalyst droplets are formed. For further information about the sample preparation procedure see [53].

4.3.2 Growth on GaAs substrates without SiO_2 layer

For these experiments, Au discs were defined on bare GaAs substrates. The Au discs were very thin to ensure that the native oxide of the GaAs substrate can be properly desorbed before the NW growth is started. As a consequence, the Au disc diameter has to be in the order of 100 nm, a size which can be reproducibly fabricated by e-beam lithography, to ensure that a sufficient amount of Au is available for the Au/Ga droplet formation. Here, two samples with four different hole grids per sample were used. The hole diameter was 50 nm, 75 nm, 100 nm and 125 nm for sample C090220A and 125 nm, 150 nm, 175 nm and 200 nm for sample C090317A, the hole pitch was 2 μm for all hole grids on both samples. Standard growth parameters with a Ga rate of 0.4 Å/s and a As pressure of 1.2×10^{-6} Torr were used, the growth temperature was 540°C for both samples.

On sample C090220A NW growth could just be observed for the hole grid with the largest hole diameter of 125 nm (cf. figure 4.6 (a)). The NW density, which is the ratio of the grown NWs and the pre-defined Au discs, could not exactly be determined because not all grown NWs are aligned in the regular hole grid. The deviation from the regular pattern is caused by surface migration of the Au/Ga catalyst droplets. However, a rough estimation can be made, yielding a NW density below 0.3. The NW length is approximately 4 μm and the NW diameter (45 ± 10)

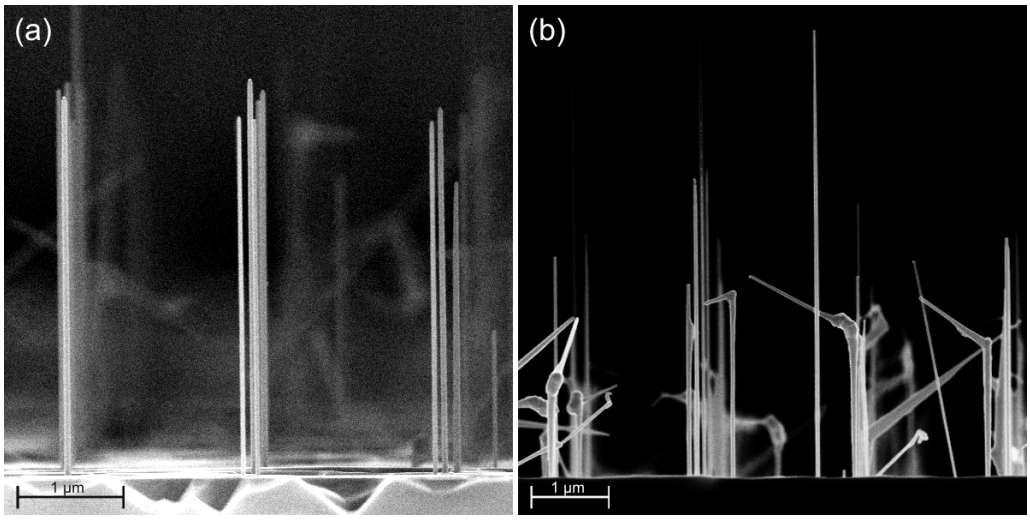

Figure 4.6: SEM side view image of (a) sample C090220A (small hole diameter) and (b) sample C090317A (large hole diameter). The NW morphology is very homogeneous for sample C090220A. However, not all NWs are grown in the predefined positions. In contrast, the NW morphology is very inhomogeneous and the sample quality was strongly reduced for sample C090317A. Here, the amount of kinked and tapered NWs is very high.

nm. On sample C090317A NW growth was observed for all hole grids. Figure 4.6 (b) shows a SEM side view image of a hole grid with 250 nm hole diameter. Especially for the hole grid with large hole diameters more than one NW was grown out of one Au disc. In contrast to sample C090220A most of the NWs are kinked after a length of 1-2 μm. The NW density could again not exactly be determined but a rough estimation gives a value larger than 0.8.

The increase in NW density on sample C090317A with respect to sample C090220A is attributed to the increased Au disc diameter. For the small Au discs of sample C090220A the amount of Au was obviously too small to initiate the Au/Ga catalyst droplet formation. The growth of more than one NW out of one Au disc on sample C090317A can also be explained by the increased Au disc diameter. Here, the amount of Au per Au disc is large enough to facilitate the formation of more than one Au/Ga catalyst droplet. The growth of kinked NWs on sample C090317A is most likely caused by a contamination of the GaAs substrate. Residues from the e-beam resist may have stuck to the Au discs after the lift off process and the chemical cleaning procedure. As a consequence, the Au/Ga droplets are contaminated with these residues, which may have caused the NW misalignment.

4.3.3 Growth on Si substrates with SiO_2 layer

To solve the problems of migrating Au/Ga droplets, multiple NW growth out of one Au disc and possible surface contamination caused by residues from the e-beam resist, the sample layout was changed. Instead of a bare GaAs substrate, a Si substrate covered by a thermal SiO_2 layer was used for further experiments. The SiO_2 layer was structured by e-beam lithography and wet chemical etching with different hole grids. The hole grids have a hole pitch between 1 μm and 4 μm and a hole diameter between 50 nm and 200 nm. The Au discs, which were previously fabricated on the bare GaAs substrate are now fabricated in the pre-structured SiO_2 holes. Due to the new sample layout, the Au layer thickness is not restricted to a few nm on the Si substrate, because the Ga for the formation of the Au/Ga droplets is now provided by the Ga effusion cell and not by the substrate. As a consequence, the native oxide of the Si substrate has not necessarily to be removed, a fact which restricts the Au disc thickness on GaAs substrates. Additionally, the SiO_2 holes prevent the Au/Ga droplets from migrating. This ensures that the NWs grow only in the predefined positions. Finally, a sample with a SiO_2 layer can be cleaned more effectively because a plasma cleaning step can be applied to oxidize any remains of the e-beam resist. As a result, carbon residues are created which are persistently attached to the surface. The carbon residues can be removed by a short HF dip, which is performed before the sample is transferred to the MBE system. The HF dip removes the first few monolayers of the SiO_2 layer and thereby any adhesions, which may stuck to it.

Influence of the Au pre-deposition

In this section we investigate the catalyst droplet formation at the beginning of the NW growth process for Au catalyzed growth on Si substrates. The Si substrates were heated to high temperatures to remove any adhesions from the SiO_2 surface before the NW growth is started. If the Au is in contact with the Si substrate, an Au/Si eutectic can be formed at an eutectic temperature of 363°C with an Au content of 18.6% [78]. To investigate if the Au discs are present in the pre-defined holes and alloy with Si from the substrate, two samples were fabricated. The first sample, C110727D, was heated to 640°C for 15 minutes and then removed from the MBE system. The second sample, C110808B, was also heated to the same temperature for the same time and NW growth was performed for 3 minutes subsequent to the heating procedure with a Ga rate of 0.8 Å/s, an As_4 pressure of 1.2×10^{-6} Torr and a growth temperature of 540°C.
For sample C110727D Au discs or Au/Si droplets were found in approximately 90%

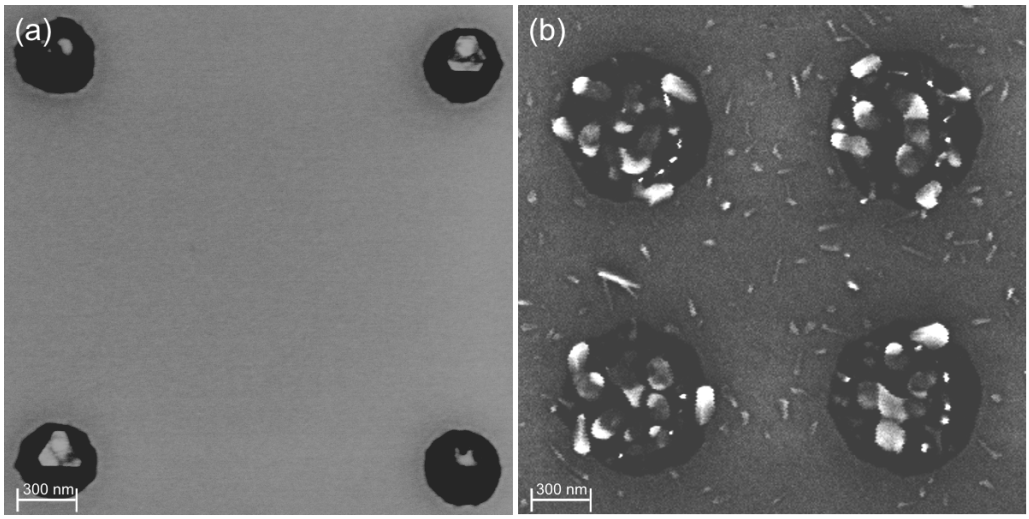

Figure 4.7: SEM top view image of (a) sample C110727D (no growth) and (b) sample C110808B (3 min. growth). On sample C110727D, the Au discs in the lower left and the upper right hole are preserved while an Au/Si eutectic was formed in the upper left and lower right hole. On sample C110808B the growth of clusters and multiple NWs out of one predefined hole could be observed.

of the predefined holes. As shown in figure 4.7 (a), the Au disc diameter is much smaller than the hole diameter in the SiO_2 layer. An investigation of the Au disc thickness with atomic force microscopy revealed that the thickness is 70% smaller than expected, in particular 3 nm instead of 10 nm. Approximately 55% of the Au discs are not alloyed with Si while the other 45 % formed small Au/Si droplets. For sample C110808B, the onset of NW growth in the predefined holes was observed. As shown in figure 4.7 (b), more than one NW was grown out of one predefined hole and also the growth of GaAs clusters in the predefined holes was observed. Additionally, the onset of cluster formation was found on the SiO_2 layer.

The fact that no Au discs or Au/Si droplets can be found in 10% of the predefined holes is attributed to the high Au flux in the sputter system. As a consequence of the high flux, the time for which the sample is exposed to the Au beam is very short. This implies that the distribution of Au is not absolutely homogeneous over the whole sample and as a result some of the predefined holes did not get the necessary amount of Au. The reduced Au disc thickness is attributed to inaccuracies in the Au flux calibration of the sputter system. The reduced Au disc diameter with respect to the predefined SiO_2 holes is attributed to the isotropic wet chemical etching procedure, which is applied to create the predefined holes in the SiO_2 layer. Due to the fact that the SiO_2 layer is etched isotropically in all three spatial dimensions during the etching procedure, the hole diameter of the SiO_2 layer is bigger than the hole diameter of the etching mask. The diameter of the sputtered Au disc is

still determined by the hole diameter of the etching mask and as a consequence the diameter of the Au discs and the diameter of predefined holes in the SiO_2 layer differ significantly from each other. The observation that nearly half of the Au discs is not alloyed with Si from the substrate indicates that a thin SiO_2 layer is formed in some of the predefined holes immediately after the second HF dip. The thin SiO_2 layer prevents the contact between the Au discs and the Si substrate and inhibits the formation of Au/Si droplets. Sample C110808B shows that NWs can be grown on pre-structured Si substrates with the Au catalyzed growth technique. The growth of more than one NW out of one hole and the additional GaAs cluster formation in the predefined holes is caused by the large hole diameter. The problem could be solved by a short latency time before the NW growth is started. Even if several Au/Ga droplets are formed, the latency time would lead to a coalescence of the Au/Ga droplets due to Ostwald ripening [80]. The origin of the cluster formation on the SiO_2 layer is the low diffusion length and the high sticking coefficient of Ga on SiO_2 in this temperature regime [44, 60]. The cluster growth on SiO_2 is a fundamental problem because it changes the surface properties of the SiO_2 layer. A change in the surface properties leads to a change in the Ga diffusion length and thereby influences the Au/Ga ratio of the catalyst droplet. Due to the fact that the primary goal of pre-structured NW growth is to obtain constant growth conditions for all NWs during the whole NW growth process, the problem of cluster formation on the SiO_2 surface has to be solved.

Influence of the growth temperature

One approach to solve the problem of GaAs cluster formation on the SiO_2 layer is to increase the NW growth temperature. An increase in growth temperature results in an increasing diffusion length [60] and a decreasing sticking coefficient [44] of Ga on the SiO_2 layer. To investigate the influence of different growth temperatures on the GaAs cluster formation and the NW morphology, three samples with different growth temperatures were grown. Standard growth parameters with a Ga rate of 0.8 Å/s and an As_4 pressure of 1.2×10^{-6} Torr were used. The properties of the NW samples are summarized in table 4.8.

It should be noted that the temperature measurement is not absolutely reliable for the pre-structured Si samples. This is caused by the layout of the Si substrate sample holder. Here, the samples are mounted from the back side through a notch in the middle of the sample holder and secured with a clamp based system because the use of Ga as adhesion agent is not possible for Si substrates. As a consequence of the notch, the heater is not separated from the sample by the sample holder. If two 5x10 mm^2 samples are mounted on the sample holder, which is the usual case,

Sample number	C110624C	C110706B	C110701B
Growth temperature [°C]	544	564	591
Manipulator power [W]	59	63	94
Hole occupation number [norm.]	1	1	1
NWs in [111] dir. [norm.]	0.69	0.47	0.24
NWs not in [111] dir. [norm.]	0.10	0.03	0.10
Cluster density [norm.]	0.21	0.50	0.66

Table 4.8: Results of the temperature series for the Au catalyzed growth on pre-structured Si substrates. The NW density is decreasing with increasing growth temperature. The numbers for NWs in [111] direction, NWs not in [111] direction and cluster density sum up to 1. The cluster density refers to the clusters in the predefined holes.

a small slot right, left and between the samples can appear because the samples do not line up precisely with the sample holder and with each other. Through these slots radiation from the heater directly reaches the pyrometer and thereby distorts the temperature measurement. To ensure that the temperature measurement is reliable, the heating power of the sample holder, also called manipulator power is used as a second parameter to compare different samples with respect to their growth temperature.

The growth temperatures of this series are reliable with respect to the applied manipulator voltages. For the samples C110624C and C110706B, a closed GaAs layer is grown on the SiO_2 layer. However, the NW density in the predefined holes is quite high for sample C110624C (cf. figure 4.8 (a)) and decreases with increasing growth temperature. For sample C110701B, the SiO_2 layer is free of GaAs clusters but the cluster density in the predefined holes is quite high (cf. figure 4.8 (b)). Also the morphology of the single NWs is changed. The fraction of NWs with large pseudo Ga catalyst droplets is strongly increased for increasing growth temperatures while the fraction of NWs with a small Au/Ga droplet tends to zero for sample C110701B.

The reduced cluster formation on the SiO_2 layer with increasing growth temperature is attributed to the increased Ga diffusion length and the reduced Ga sticking coefficient at high growth temperatures. The increased cluster formation in the predefined holes and the change in NW morphology with increasing growth temperature can be explained by an exceedance of the maximum growth temperature for Au catalyzed NW growth. As determined is section 4.1.2, the maximum growth temperature for the Au catalyzed growth technique is approximately 580°C. We conclude that samples C110624C and sample C110706B are grown in the Au catalyzed growth mode while sample C110701B is grown in the pseudo Ga catalyzed growth

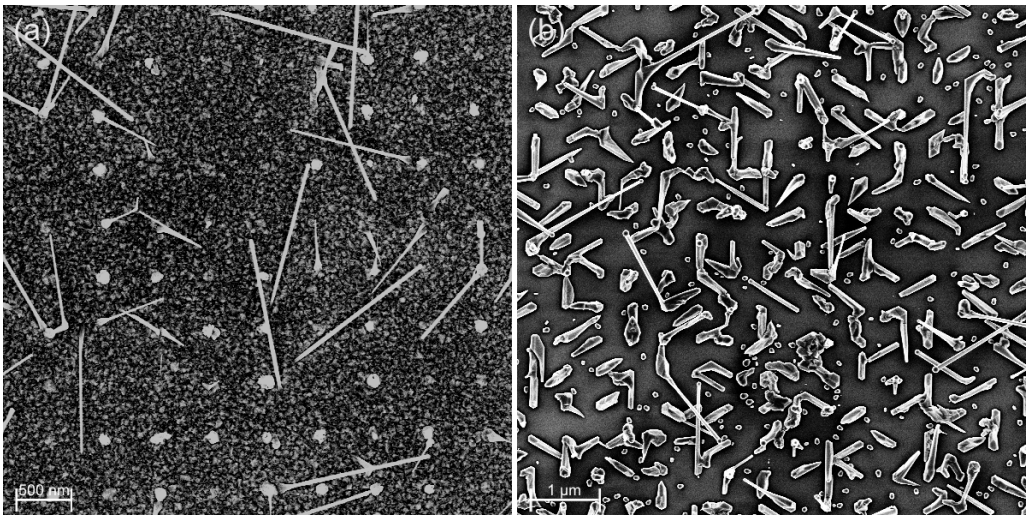

Figure 4.8: SEM top view image of (a) sample C110624C (T_{growth}=544° C) and (b) sample C110701B (T_{growth}=591° C). The SiO_2 layer of sample C110624C is completely covered with a rough GaAs layer. Nevertheless, NW growth could be observed in the predefined holes. The NWs appear as white dots in the SEM top view image. On sample C110701B, the SiO_2 layer is mostly free of clusters but cluster formation is observed in the predefined holes. Additionally, the NW density is strongly reduced.

mode [98]. This classification is supported by the morphology of the NWs on sample C110701B, which show a well defined hexagonal cross section and an increased size of the catalyst droplet, which is characteristic for the Ga catalyzed growth mode.

Due to the fact that the sticking coefficient for Ga on the SiO_2 layer is unity for the maximum growth temperature of Au catalyzed NW growth [44], both, a clean SiO_2 surface and Au catalyzed NW growth could not be achieved on the same sample with these growth parameters. On the one hand, the cluster formation on the SiO_2 surface at low growth temperatures changes the surface properties and thereby the Ga diffusion length. As a consequence, also the Au/Ga ratio of the catalyst droplets is changed during growth. This inhibits a controlled NW crystal structure tuning. On the other hand, the change in the growth mode from Au catalyzed to pseudo Ga catalyzed [98] at high growth temperatures also inhibits NW crystal structure tuning, because pure WZ NWs could only be achieved with the Au catalyzed growth method [100]. To conclude, the increase in growth temperature is not a suitable method to suppress the cluster formation on the SiO_2 layer because the growth mode is changed from Au catalyzed to pseudo Ga catalyzed. A different approach has to be used to get rid of the cluster formation on the SiO_2 layer and simultaneously conserve the Au catalyzed growth mode.

Sample number	C110701B	C110720D	C110718A
Ga rate [Å/s]	0.8	0.4	0.8
As pressure [10^{-6} Torr]	1.2	1.2	3.65
As_4/Ga ratio	1.8	3.6	5.4
Growth temperature [°C]	591	595	591
Manipulator power [W]	94	87	87
Hole occupation number [norm.]	1	1	1
NWs in [111] dir. [norm.]	0.24	0.26	0.06
NWs not in [111] dir. [norm.]	0.10	0.14	0.03
Cluster density [norm.]	0.66	0.60	0.91

Table 4.9: Results of the As_4/Ga ratio series for the Au catalyzed growth on pre-structured Si substrates. The growth of clusters on the SiO_2 layer and in the predefined holes is increased for increasing As_4/Ga ratios. In contrast, the NW density is strongly reduced for increasing As_4/Ga ratios.

Influence of the As_4/Ga ratio

Due to the fact that an increase in growth temperature above 570°C leads to the occurrence of a pseudo Ga catalyzed growth mode at an As_4/Ga ratio of 1.8, the As_4/Ga ratio was increased to 3.6 and 5.4 in order to regain the Au catalyzed growth mode. The additional As_4 was supposed to consume the excess Ga of the catalyst droplet, thereby changing the growth mode from pseudo Ga catalyzed to Au catalyzed. The growth temperature was kept at 590°C to prevent cluster formation on the SiO_2 layer. For the sample with an As_4/Ga ratio of 3.6, the Ga rate was reduced to 0.4 Å/s and the As_4 pressure was kept at 1.2×10^{-6} Torr while for the sample with an As_4/Ga ratio of 5.4 a Ga rate of 0.8 Å/s and an As_4 pressure of 3.65×10^{-6} Torr was used. The results are summarized in table 4.9.

The growth temperatures of all three samples are very close to each other while the manipulator power of sample C110701B is slightly increased with respect to the other two samples. As a consequence, the real growth temperature of sample C110701B might be a little bit higher than the measured value, which would be in agreement with the growth temperatures and manipulator powers of section 5.2.1. However, the growth temperatures of all three samples are above 590°C, which is higher than the maximum growth temperature for the Au catalyzed growth technique at an As_4/Ga ratio of 1.8 (cf. chapter 4.1.2). Therefore, the samples can be compared with respect to the influence of different As_4/Ga ratios on the NW growth mode at high growth temperatures.

Due to the increased As_4/Ga ratios of samples C110720D and C110718A, cluster

formation on the SiO_2 layer was observed. The clusters grew as single crystallites and did not form a closed GaAs layer. The cluster formation in the predefined holes is strongly increased with increasing As_4/Ga ratio. The NWs grew exclusively in the pseudo Ga assisted growth mode.
The results clearly indicate that an increase in As_4/Ga ratio cannot change the growth mode from pseudo Ga assisted to Au assisted. Despite that, the high As_4 pressure reduces the diffusion length of Ga on the SiO_2 layer and thereby increases the Ga cluster formation. Additionally, the catalyst droplets in the predefined holes are rapidly consumed by As_4 for high As_4/Ga ratios. This results in a decreased NW density and an increased cluster density for increasing As_4/Ga ratios.

Influence of As_2

Due to the fact that Au catalyzed NW growth could not be achieved at high growth temperatures independent of the used As_4/Ga ratio, the influence of As_2 on the GaAs cluster formation at low growth temperatures was investigated. The Ga diffusion length is known to be different under As_2 than under As_4. An increase in Ga diffusion length would lead to an increase in NW density and a decrease in cluster formation. If the Ga diffusion length is increased or decreased depends on the type and the crystal orientation of the substrate [43, 103]. However, no data is available for SiO_2. One sample (C110801A) with a Ga flux of 0.8 Å/s, an As_2 pressure of 0.36×10^{-6} Torr which yields an As_2/Ga ratio of 1.8 and a growth temperature of 558°C at a manipulator power of 62 W was grown. The growth parameters, especially the Ga rate, the As_x/Ga ratio and the growth temperature are comparable with the growth parameters of sample C110624C, which was investigated in section 4.3.3.
The sample grown with As_2, C110801A, shows an inferior sample quality compared to the sample grown with As_4, C110624C. The whole SiO_2 layer was covered by a rough GaAs layer. Ga puddles and a very low number of pseudo Ga catalyzed NWs could be found on the GaAs layer. We conclude that the use of As_2 is not suitable to prevent the GaAs cluster formation on the SiO_2 layer at low growth temperatures.

4.3.4 Conclusion

In this section we investigated positioned controlled growth of GaAs NWs on GaAs and Si substrates. As illustrated in the introduction to this section, position control is the precondition for NW size and crystal phase control of each single NW. The first approach to position controlled NW growth was the fabrication of Au discs in a grid like pattern with a diameter between 50 nm and 200 nm on bare GaAs substrates. During the oxide desorption procedure, the Au discs alloy with Ga

from the GaAs substrate and form Au/Ga droplets, which work as catalysts for NW growth. Problems arise from the sample layout because the Au/Ga droplets can migrate on the GaAs substrate. As a consequence, the equal distance between the catalyst droplets is lost and the incoming material from the effusion cells is not uniformly distributed under all NWs. Further problems arise from a possible contamination of the GaAs substrate surface which is attributed to residues from the e-beam resist. To solve this problem, the sample layout was changed. Now, Si substrates with a thermal SiO_2 layer were used for position controlled NW growth. To achieve position control, hole grids with different hole diameters were defined on the SiO_2 layer by e-beam lithography and wet chemical etching. The Au discs are now placed inside the predefined holes, which prevent the migration of the Au/Ga droplets. Also the problem of surface contamination is solved because an additional HF cleaning step can by applied which removes the first few monolayers of the SiO_2 layer and thereby any adhesion, which may stuck to it. New problems arise from the cluster formation on the SiO_2 layer. The cluster growth changes the surface properties of the SiO_2 layer and thereby the diffusion length of the Ga atoms. As a consequence, the Au/Ga ratio of the catalyst droplets is changed, which influences the crystal structure of the growing NWs. To get rid of the cluster formation, the growth temperature was raised to 590°C. At this growth temperature, the sticking coefficient of Ga on the SiO_2 layer is strongly reduced [44] and the cluster formation is suppressed. Unfortunately, this temperature is too high for Au catalyzed NW growth. The NW growth mode changes from Au catalyzed to pseudo Ga catalyzed which yields a decrease in NW density. Additionally, crystal phase control is not possible in the Ga catalyzed growth mode [100]. The attempt to restore the Au catalyzed growth mode by increasing the As_4/Ga ratio failed. Instead of a reduction of the excess Ga in the catalyst droplet, the growth of clusters on the SiO_2 layer and in the predefined holes was observed with increasing As_4/Ga ratios. Finally, the As species was changed form As_4 to As_2 to increase the diffusion length of Ga at NW growth temperatures below 570°C. Again, this attempt was not suitable to solve the problem of cluster formation on the SiO_2 layer.

In summary, we found that position controlled NW growth is very difficult to achieve for the Au catalyzed growth technique. To prevent the GaAs cluster formation on the SiO_2 layer, high growth temperatures above 590°C are necessary. At these high growth temperatures, only pseudo Ga catalyzed or Ga catalyzed NW growth is possible. In the next chapter, the sample layout is changed to provide suitable templates for position controlled NW growth with the Ga catalyzed growth technique.

Chapter 5

The Ga technique: Growth on SiO_2 covered substrates

In this chapter the results achieved with the Ga technique will be presented. For the Ga technique, a substrate covered by a thin SiO_2 layer is used. The SiO_2 layer works as mask material and prevents the nucleation of GaAs at substrate temperatures above 570°C [44]. Defects in the SiO_2 layer, which result from the SiO_2 layer fabrication procedure, e.g. sputtering or which are artificially created e.g. by wet chemical etching provide nucleation sites for Ga atoms. The Ga atoms accumulate at the defect sites to spherical Ga droplet with a diameter of approximately 80 nm. The Ga droplets work as catalyst during the NW growth.
First we investigated the influence of different growth temperatures, different kinds of SiO_2 layers and SiO_2 layer thicknesses on the NW density and morphology. Our goal is to obtain NW samples with a NW density comparable to the NW density of the Au technique. In addition, the NWs should be homogeneous in size to provide suitable templates for the GaMnAs shell growth.
Next, we pre-structure the SiO_2 layer by e-beam lithography and wet chemical etching to create predefined hole, which are arranged in a grid like pattern. The predefined holes provide defined nucleation sites for the Ga catalyst droplets. A uniform distance between the catalyst droplets is a precondition for the equal distribution of the incoming material from the effusion cells under all NWs. As the amount and the ratio of Ga and As determines the NW morphology and crystal structure of a single NW [100], position control is a necessary step to achieve NW size and crystal phase control. Like in the fist part of this chapter we investigate the influence of different growth parameters and SiO_2 layers on the hole occupation number and the NW morphology. To explain our observations, we modify the current growth model.

5.1 Growth on unstructured substrates

For the growth on GaAs substrates, a sputtered SiO_2 layer with an initial layer thickness between 20 nm and 35 nm was used. The substrate, the substrate preparation technique and the growth parameters were provided by Prof. Dr. Fontcuberta i Morral from the Walter Schottky Institut (WSI) in Munich (now Ecole Polytechnique Fédérale de Lausanne, Switzerland). For the growth on Si substrates, two different kinds of SiO_2 layers were investigated. Native SiO_2 is naturally generated on Si substrates when they are exposed to air. The native SiO_2 layer thickness is in the order of a few nm. In contrast, thermal SiO_2 is artificially created by a high temperature annealing procedure of the Si substrates under oxygen rich conditions. Here, the SiO_2 layer thickness can be controlled by the annealing parameters and is adjusted to 30 nm. Both types of substrates were provided by Silicon Materials. As the usual way of wafer mounting - using Ga as adhesion agent between the GaAs substrate and the sample holder - is not possible for Si substrates, a new kind of sample holder had to be designed. This sample holder uses a clamp based mounting system to secure the Si wafers.

The provided growth parameters for the Ga rate of 0.2 Å/s and for the As_4 fluxes of 5×10^{-7} Torr, which we will refer to as standard growth parameters, could be used for our MBE system without any changes. However, this was not possible for the growth temperature as the values for the temperature measurements, which are conducted with a pyrometer, can significantly differ from one MBE system to another. The reasons for this behavior are the different geometries of the growth chambers and other MBE specific quantities, e.g. the condition of the pyroport window. Therefore, a sample series with different NW growth temperatures was fabricated to find the best temperature value for our MBE system. Due to the fact that the NW density was quite low and the NW growth was undirected in the first attempts, experiments concerning the SiO_2 layer thickness were performed for three different kinds of SiO_2 layers.

For a directed NW growth and a suitable NW density, the SiO_2 layer has to be thinned down from its initial thickness to below 10 nm. This was done by wet chemical etching using an Ammonium fluoride etching mixture with a HF concentration of 1.25%. The HF etching was either done immediately before the sample was loaded or a second short HF dip was applied prior to the transfer in the MBE system, if the SiO_2 layer was thinned down before. The purpose for the second HF dip is to remove a few nm of the SiO_2 layer and thereby any adhesions, which may stuck to it. For native SiO_2 on Si substrates only a short HF dip of two seconds was applied because the native SiO_2 layer is already very thin.

Sample number	C080515B	C080609A	C080613B	C080613A	C080515A
Growth T [°C]	569	580	590	595	600
NW density [μm^{-2}]	0.03	0.2	0.1	0.04	0.02
Cluster density [μm^{-2}]	6.4	1.6	0.8	0.6	0.07
NW diameter [nm]	98	62	176	85	98
Standard dev. [nm]	13	11	13	12	11
Tapering [norm.]	1.2	1.0	1.5	1.5	1.3

Table 5.1: Influence of the NW growth temperature on the NW and cluster density as well as on the NW morphology. The NW density is increasing until 580° C and then decreasing while the cluster density is continuously decreasing for increasing growth temperatures.

5.1.1 Influence of the growth temperature

To adjust the NW growth temperature of the WSI MBE system, which was 620°C, to our MBE system, a series of five samples was grown. For these experiments, GaAs substrates with a sputtered SiO_2 layer and standard growth parameters for Ga and As_4 were used. The SiO_2 layer thickness was approximately 10 nm for the samples with a growth temperature of 570°C, 580°C and 600°C and approximately 23 nm for the samples with a growth temperature of 590°C and 595°C. The results are summarized in table 5.1.

The NW density is increasing from 570°C to 580°C and then slowly deceasing for higher growth temperatures. The cluster density is highest for a growth temperature of 570°C and decreases with increasing growth temperature. The NW growth is undirected on all samples. This inhibits the investigation of the NW length, because the SEM images have to be taken perpendicular to the NW growth direction or the tilt angle of the NW has to be known. Otherwise, the SEM image shows only a two dimensional projection of the NW and the NW length is distorted. The NW diameter and the NW tapering exhibit a pronounced maximum for the sample grown at 590°C.

The change of the NW density and the cluster density could be explained with the temperature dependent sticking coefficient and the temperature dependent diffusion length of Ga on SiO_2. At low growth temperatures, the sticking coefficient of Ga is high [44] and the Ga diffusion length is low [60]. As a consequence of the high sticking coefficient, the amount of Ga on the SiO_2 surface is high. Due to the fact that the diffusion length is limited, the Ga atoms often nucleate on the next nearest defect site of the SiO_2 layer and do not reach a Ga catalyst droplet. This results in a low NW density and a high cluster density. At intermediate growth temperatures, the amount of Ga on the SiO_2 surface is reduced and the diffusion

length is increased [44, 60]. Now the Ga atoms can diffuse in increasing number to the Ga catalyst droplets, yielding a higher NW density and a decreasing cluster density. At high growth temperatures, the amount of Ga on the SiO_2 surface is low while the Ga diffusion length is further increased [44, 60]. At this stage, the amount of Ga on the SiO_2 surface is so small that the NW density as well as the cluster density are decreasing.
In summery we found that the best growth temperature with respect to a high NW density and a low cluster density is in the range of 590°C to 595°C. The undirected NW growth, which was observed on all samples of this series is attributed to the thick SiO_2 layer, which prevents the contact between NWs and GaAs substrate. In the next section, the influence of the SiO_2 layer thickness on the NW density and morphology will be systematically investigated.

5.1.2 Growth on sputtered SiO_2

For these experiments, GaAs substrates with a sputtered SiO_2 layer were used. To find the SiO_2 layer thickness which gives the best NW density and morphology, a series of seven samples with different SiO_2 layer thicknesses were grown using standard growth parameters. To ensure that the final SiO_2 layer thickness is adjusted as precisely as possible, the initial SiO_2 layer thickness as well as the SiO_2 etching rate were determined before the etching procedure. To exclude differences in material fluxes or growth temperature, all samples were mounted on the same sample holder and grown during one growth run. The results of this experiment are summarized in table 5.2. The sample with a SiO_2 layer thickness of -10 nm is an over-etched samples. Here, the etching time was chosen such that 10 additional nm of SiO_2 could be removed. The labels (a) and (b) are used to differentiate between bright and dark areas on the sample.
The NW density is increasing with decreasing SiO_2 layer thickness. The only exception is the sample with 10 nm SiO_2, which shows a higher NW density than most of the other samples. The best value for the NW density is obtained for the over-etched sample. The cluster formation is totally suppressed for the samples with a SiO_2 layer thickness between 15 nm and 0 nm. The bright areas of the over-etched sample show a cluster density of 0.6 μm^{-2} (cf. figure 5.1 (a)) while the dark areas show a coalescence of the numerous clusters (cf. figure 5.1 (b)), which is expressed by an infinite sign in table 5.2. The density of the black triangles, which are observed in SEM top view images on the substrate surface increases for a decreasing SiO_2 layer thickness and disappears for the over-etched sample. The size of the NWs is very similar for the samples with 15 nm to 0 nm SiO_2 layer thickness. Here, nearly

Sample number	C110829B							
SiO_2-layer thick. [nm]	15	10	7.5	5	2.5	0	-10(a)	-10(b)
NW density [μm^{-2}]	0.37	2.61	0.39	0.43	0.65	0.57	1.2	5
Cluster density [μm^{-2}]	0	0	0	0	0	0	0.6	∞
Black triangles [μm^{-2}]	<0.05	<0.05	<0.05	<0.05	<0.2	<0.5	0	0
NW length [μm]	0.3						5.9	6.8
Standard dev. [μm]	0.05						0.26	0.07
NW diameter [nm]	145						123	128
Standard dev. [nm]	25						9	12

Table 5.2: NW density, cluster density and NW properties for different SiO_2 layer thicknesses. The best result with respect to the NW density and NW morphology are achieved for the over-etched sample. Here, the labels (a)/(b) denote the bright/dark areas on the over-etched sample, respectively.

exclusively short and thick NWs with an irregular morphology are grown. The NW length is strongly increased for the over-etched sample while the NW diameter is slightly decreased.

The results show that the SiO_2 layer has to be extremely thin or almost etched away to obtain samples with an adequate NW density and morphology. This is supported by the high cluster density, which is observed in the dark regions of the over-etched sample because cluster formation is only possible on the bare GaAs substrate under the applied growth conditions. The black triangles are defects on the SiO_2 layer which are caused by the etching procedure. The increasing number of defects with decreasing SiO_2 layer thickness could be explained by the longer etching time, which is necessary to obtain thinner SiO_2 layers. The absence of black triangles for the over-etched sample additionally supports the assumption of an almost vanished SiO_2 layer. From these results we can conclude that the last few monolayers of the SiO_2 layer strongly adhere on the GaAs substrate and are hard to remove by the Ammonium fluoride etching procedure. The remaining thin SiO_2 layer provides a high number of nucleation sites for the formation of Ga catalyst droplets and allows a connection of the growing NWs to the GaAs substrate, yielding directed NW growth. Despite the fact that the obtained NW density and morphology is very satisfying for the over-etched sample (cf. figure 5.1 (c)), the SiO_2 layer thickness, which is necessary for a good NW morphology and NW density is hard to adjust. Therefore, the field of application for Ga catalyzed NW growth on sputtered SiO_2 with respect to the growth of NW heterostructures is limited.

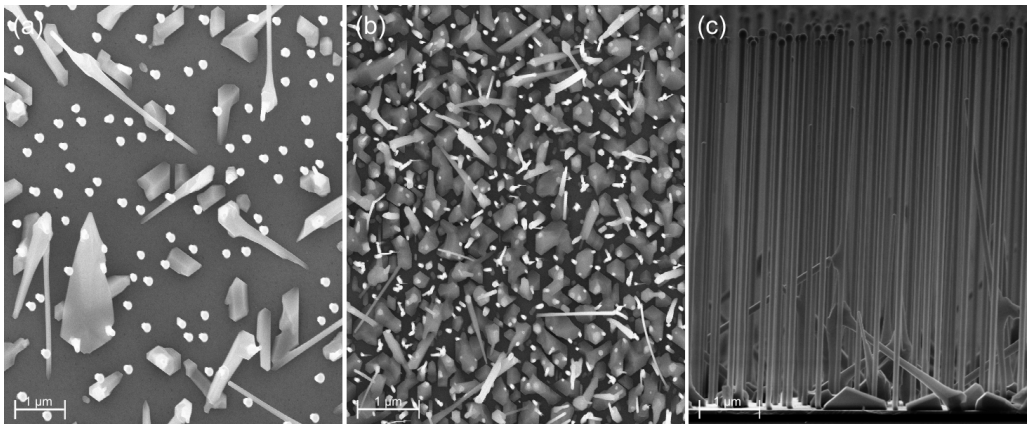

Figure 5.1: SEM top view image from (a) the bright area of the over-etched sample and (b) the dark area of the over-etched sample. SEM side view image from (c) the dark areas of the over-etched sample. The NW size is very homogeneous and the NW density is quite high.

5.1.3 Growth on native SiO_2

For these experiments, Si substrates with a native SiO_2 layer were used. Due to the fact that the native SiO_2 is very thin the first HF etching step, which is used to adjust the SiO_2 layer thickness to the required value, can be skipped. We had to investigate if the second HF etching step, which is usually applied to remove adhesions form the SiO_2 surface before the sample is transferred to the MBE system, is necessary for the native SiO_2 layer. Therefore, two samples were grown under identical growth conditions, one with and one without second HF dip. The results are summarized in table 5.3.

As can be seen in figure 5.2, the NW density and the NW orientation are significantly influenced by the second HF etching step. While the NW density drops form 2.5 μm^{-2} to 1.4 μm^{-2}, the ratio of NWs oriented in the [111] direction decreases from 1 to 0.6 for the not etched sample with respect to the etched sample. The cluster formation between the NWs is observed on both samples but very pronounced on the sample with second HF dip. The infinity sign in table 5.3 indicates that the clusters are grown together and form a nearly closed GaAs layer. Also the NW morphology is influenced by the second HF dip. The NW diameter increases while the NW length decreases for the etched sample with respect to the not etched sample.

The massive cluster formation, the well oriented NW growth and the high NW density of the sample with second HF dip are comparable to the corresponding quantities of the over-etched sample C110829B, which was discussed in chapter 5.1.2. This indicates that the second HF dip removed the native SiO_2 nearly completely. In contrast, as a consequence of the thicker native SiO_2 layer, the sample without

Sample number	C110623C	C110706C	C110718B
Oxide type	native	native	thermal
2nd HF etching step	yes	no	yes
NW density [μm^{-2}]	2.5	1.4	0.03
NWs in [111] dir. [norm.]	1	0.6	0
Cluster density [μm^{-2}]	∞	∞	2.5
NW length [μm]	4.1	4.7	-
Standard dev. [μm]	0.45	0.8	-
NW diameter [nm]	147	88	170
Standard dev. [nm]	15	10	36
Tapering [norm.]	0.9	1.1	1.3

Table 5.3: The influence of the second HF etching step applied immediately before the sample is loaded in the MBE system on the NW and cluster density as well as one the NW morphology for two native SiO_2 samples. The results are compared with a thermal SiO_2 sample, which has approximately the same SiO_2 layer thickness of 1-3 nm.

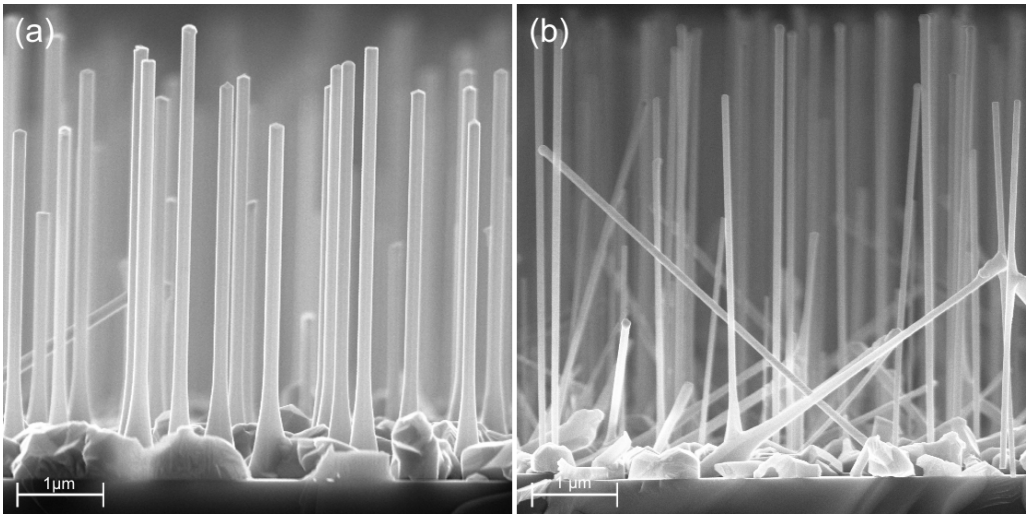

Figure 5.2: SEM side view image of (a) sample C110623C (sample with second HF dip) and (b) sample C110706C (sample without second HF dip). The NW density and orientation are increased for sample C110623C with respect to sample C110706C.

second HF dip shows a reduced cluster formation with a lower ratio of oriented NWs and a lower NW density. The differences in NW tapering between the etched and the not etched sample are relatively small and can be explained by statistical fluctuations. We therefore conclude that the second HF etching step is essential for a good sample quality, although this implies an increased cluster formation on the SiO_2 layer.

5.1.4 Growth on thermal SiO_2

For these experiments, Si substrates with a thermal SiO_2 layer were used. We investigated if the results achieved with native SiO_2 can be reproduced with thermal SiO_2. Therefore, a thermal SiO_2 layer with an initial thickness of 30 nm was etched down with 1.25 % Ammonium fluoride to approximately 5 nm. A second HF etching step was applied to clean the SiO_2 surface before the sample was transferred to the MBE system. The final thickness of the etched thermal SiO_2 layer after the second HF etching step was approximately 1-3 nm, which is comparable to the size of the etched native SiO_2 layer. The sample holder and the growth parameter were identical for the native and the thermal SiO_2 samples. The results are summarized in table 5.3 (right column, sample C110718B).
We see that the sample quality is strongly decreased for the thermal SiO_2 layer compared to the native SiO_2 layer. The NW density is reduced by almost two orders of magnitude, the NW growth is undirected and the NW diameter differs significantly between the NW top and the NW bottom, yielding a NW tapering of 30%. Note that due to the undirected NW growth the NW length could not be estimated.
The origin of the decreasing sample quality can be attributed to the SiO_2 layer thickness, which was above the optimum value for this sample. Due to the fact that a final SiO_2 layer thickness of below 1 nm is hard to adjust if the initial SiO_2 layer thickness is 30 nm, the use of Si substrates with native SiO_2 is recommended for further experiments.

5.1.5 Conclusion

In this section we investigated the influence of different growth temperatures and different kinds of SiO_2 layers on the NW sample quality. The best growth temperature with respect to a high NW density and a low cluster density was found to be in the range of 590°C to 595°C for sputtered SiO_2 on GaAs substrates. Here, the cluster formation is almost fully suppressed due to the high diffusion length of Ga

on the SiO_2 surface while the sticking coefficient of Ga is still high enough to provide a sufficient amount of Ga for the Ga catalyst droplet formation.
For the sputtered SiO_2 layer on GaAs substrates we found that the SiO_2 layer thickness has to be very thin to obtain directed NW growth and a high NW density. The best results were achieved with an over-etched sample. Here, the remaining SiO_2 layer provides a high number of nucleation sites for the formation of Ga catalyst droplet and allows the contact between the growing NWs and the underlying GaAs substrate, yielding directed NW growth. For the native SiO_2 layer on Si substrate, one sample with and one sample without HF dip was investigated. The sample with HF dip had a superior sample quality which is attributed to the reduced size of the native SiO_2 layer. For the thermal SiO_2 layer on Si substrate, one sample with an initial SiO_2 layer thickness of 30 nm was analyzed. The thermal SiO_2 layer was reduced in a first HF etching step to 5 nm and in a second HF etching step to approximately 1-3 nm, which is the assumed size of the etched native SiO_2 layer. However, the thermal SiO_2 sample shows an inferior sample quality with a strongly reduced NW density and an undirected NW growth. This result is attributed to the SiO_2 layer thickness, which was obviously too large on the investigated sample. We conclude that for the growth of GaAs NWs on Si substrates native SiO_2 should be favored because the SiO_2 layer thickness is much easier to adjust to the appropriate value compared to the thermal SiO_2.

5.2 Growth on pre-structured Si substrates

For the growth on pre-structured Si substrates, a thermal SiO_2 layer with an initial layer thickness of 30 nm was used. The substrates were purchased from Silicon Materials. First the wafer was cut into 10x10 mm^2 double sample pieces. The SiO_2 layer thickness was reduced to approximately 15 nm by wet chemical etching, using a Ammonium fluoride etching mixture with a HF concentration of 1.25%. An etching mask consisting of hole grids with different hole pitches was defined in the middle of every 5x10 mm^2 sample by e-beam lithography. The etching mask was transferred to the SiO_2 layer by wet chemical etching, using the same etching mixture as for the first etching step. The sample was chemical cleaned with Acetone and Propanol. A third short HF dip was performed to clean the SiO_2 surface before the samples were transferred to the MBE system. For more detailed information about the sample preparation procedure see [53].
To obtain a high hole occupation number, which is the ratio of the occupied predefined holes and the total number of the predefined holes, Ga was deposited on the substrate before the NW growth was started. High fluxes of one monolayer per sec-

Sample number	C110728D	C110803A	C110707C
As species	none	As_2	As_4
Amount of deposited Ga [Å]	140	140	140
Deposition time [sec.]	50	50	50
Growth temperature [°C]	616	627	629
Manipulator power [W]	99	99	87
Hole occupation number [norm.]	1	1	1
NWs in [111] dir. [norm.]	-	0.02	0.44
NWs not in [111] dir. [norm.]	-	0.03	0.22
Cluster density [norm.]	-	0.95	0.34

Table 5.4: Applied Ga pre-deposition parameters for the growth on Si substrates. On sample C110728D, only Ga pre-deposition was performed to investigate the Ga droplet formation in the predefined holes. For sample C1100803A and C110707C, NW growth with different As species was performed after the Ga pre-deposition procedure.

ond for Ga and a beam equivalent pressures of 1.8×10^{-6} Torr for As_2 and 4.3×10^{-6} Torr for As_4 were used. In addition, the influence of the As_2/Ga ratio on the hole occupation number was investigated. Note that the temperature measurements are not absolutely reliable due to the geometry of the Si sample holder (cf. chapter 4.3.3). Therefore, the heating power of the substrate is given as second reference value for the growth temperature.

5.2.1 Influence of the Ga pre-deposition and the As species

For this experiment, three samples were investigated. On the first sample, 140 Å of Ga were pre-deposited at 616°C. Here, only the Ga cell was opened for 50 s while the As cell was closed [70]. The sample was removed from the MBE system after the Ga pre-deposition procedure and no NW growth was performed. On the second and third sample, NWs were grown using the growth parameters of [85] with a high Ga flux of one monolayer per second and different As species. The As_x pressure was adjusted such that the As_x/Ga ratio was 1.8 for both samples. The results are summarized in table 5.4.
The measured temperatures and the applied manipulator power seem to be inconsistent for the three investigated samples. Despite the fact that both samples are heated with the same manipulator power, sample C110803A shows a 13°C higher temperature than sample C110728D. This difference in the temperature measurement is attributed to the measurement error caused by the geometry of the sample holder, which was discussed in chapter 4.3.3. A similar inconsistence can be found

when the temperature and the manipulator power of sample C110707C and sample C110803A are compared. Here, both samples show the same temperature but the applied manipulator power of sample C110707C is 12 W smaller than the applied manipulator power of sample C110803A. This can be explained by the different Ga cells used for NW growth. To obtain the same Ga rate the Ga cell used for sample C110707C (Ga4: 1020°C) has to be heated to a much higher temperature than the Ga cell used for sample C110803A (Ga5: 963°C). Therefore, the high growth temperature of sample C110707C can be explained by the increased heat input from the Ga cell, which compensated the reduced manipulator power. Due to the fact that the differences in temperature between sample C110728D and sample C110803A as well as the differences in the manipulator power between the samples C110707C and C110803A can be consistently explained, we assume that all three samples have approximately the same substrate temperature during growth.

On sample C110728D a Ga droplet is formed in every predefined hole, independent of the hole pitch. The size of the Ga droplet is much smaller than the size of the predefined hole and increases with increasing hole diameter. Figure 5.3 (a) shows a hole grid of sample C110728D with a hole pitch of 1 μm after Ga pre-deposition. Sample C110803A, which is grown with As_2, has a hole occupation number of 1 but a very high cluster density of 0.95. The few NWs which are grown on this sample grow in the [111] direction and in random directions with equal probability. Figure 5.3 (b) shows a hole grid of sample C110803A with a hole pitch of 4 μm after NW growth. Sample C110707C, which is grown with As_4, has a hole occupation number of 1 and a cluster density of 0.34 in the predefined holes. However, a massive cluster formation was be observed on the SiO_2 layer. The NWs grow in the [111] direction and in random directions. Figure 5.3 (c) shows a hole grid of sample C110707C with a hole pitch of 1 μm after NW growth.

The results of sample C110728D show that the concept of Ga pre-deposition works. Despite the fact that the pre-deposition temperature is high, the deposited Ga forms droplets in the predefined holes and is not reevaporated from the substrate. The fact that most of the grown NWs point in the [111] direction while a smaller number point in random directions on sample C110803A and C110707C is attributed to an oxide layer on the bottom of the predefined holes. The oxide layer partially inhibits the contact between the catalyst droplet and the Si substrate which results in an undirected NW growth.

The difference in cluster density in the predefined holes between the samples grown with As_4 and As_2 is attributed to the different diffusion length of Ga for different As species (cf. chapter A.2). A shorter diffusion length is equivalent to a higher nucleation probability. If we adopt these results to Si substrates, the accumulated

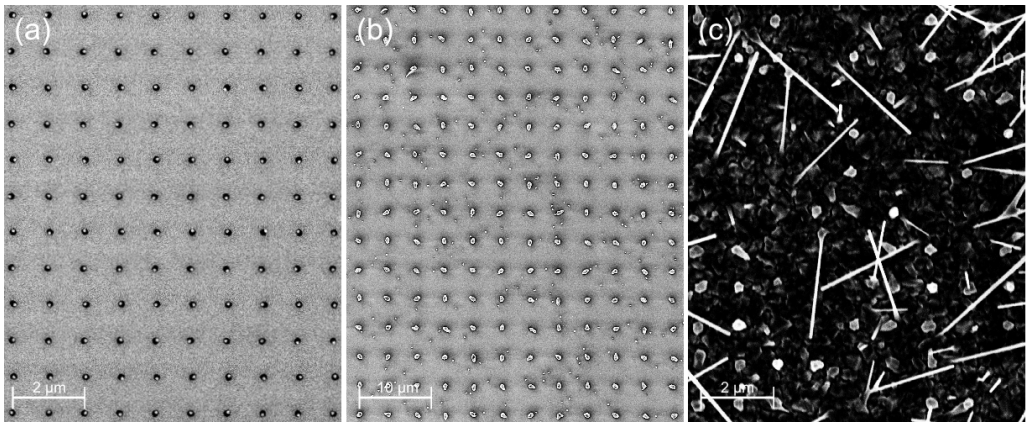

Figure 5.3: (a) SEM top view image of sample C110728D (no growth) after the Ga pre-deposition procedure. A Ga droplet is visible in every predefined hole. (b) SEM top view image of sample C110803A (As_2) after NW growth. Here, cluster growth is observed in the predefined holes while no cluster formation is found between the predefined holes. (c) SEM top view image of sample C110707C (As_4) after NW growth. Here, NW growth can be observed in the predefined holes but also cluster formation is found in and between the predefined holes.

Ga atoms in the predefined holes are rapidly consumed by As_2 and GaAs clusters are formed before the Ga atoms can accumulate to Ga catalyst droplets. The massive cluster formation on the SiO_2 layer for the sample grown with As_4 is attributed to a combination of the high total As_4 pressure of 4.3×10^{-6} Torr, which reduces the Ga diffusion length and the bad quality of the used SiO_2 layer [71].

5.2.2 Influence of the As_2/Ga ratio

In this section the influence of the As_2/Ga ratio on the cluster density is investigated. Despite the fact that the cluster formation in the predefined holes was very pronounced for sample C110803A, which was examined in the previous section, Plissard et al. [85] showed that a high NW density without cluster growth is achievable with As_2 on pre-structured SiO_2. To reduce the high cluster density of sample C110803A, a series of three samples with different As_2/Ga ratios was grown. The As_2 pressure was increased such that the As_2/Ga ratio was 2.9 and 4.4 for the investigated samples because previous experiments (cf. chapter A.2) showed that an As_2/Ga ratio of 1.8 is below the optimum value for a high NW sample quality. For this experiment, a high Ga rate of one monolayer per second at a growth temperature of 620°C was used. Ga pre-deposition was applied for sample C110803A and sample C110725A but not for sample C110805A. The growth parameters and the obtained results are summarized in table 5.5.
The obtained values for the temperature measurement are trustworthy as the applied

Sample number	C110803A	C110805A	C110725A
As_2/Ga ratio	1.8	2.9	4.4
Ga pre-deposition	yes	no	yes
Growth temperature [°C]	627	622	620
Manipulator power [W]	99	99	99
Hole occupation number [norm.]	1	0.75	1
NWs in [111] dir. [norm.]	0.02	0.06	0.02
NWs not in [111] dir. [norm.]	0.03	0.02	0
Cluster density [norm.]	0.95	0.92	0.98

Table 5.5: Influence of the As_2/Ga ratio on the sample quality of pre-structured Si substrates. To vary the As_2/Ga ratio, the Ga rate was fixed at one monolayer per second and the As_2 pressure was increased from 1.8×10^{-6} Torr to 4.3×10^{-6} Torr. The growth temperature was kept constant at approximately 620° C for all samples.

manipulator power was the same for all three samples and the measured temperatures are very close together. The hole occupation number is quite high for all three samples but the NW density is quite low. Instead of NWs, clusters are grown in the predefined holes independent of the applied As_2/Ga ratio and the Ga pre-deposition procedure.

The high cluster density of sample C110803A could not be reduced by changing the As_2/Ga ratio. The clusters show up for all As_2/Ga ratios independent of the fact if Ga pre-deposition was performed or not. The reason for this behavior is the fast consumption of Ga under As_2. A detailed explanation for this behavior was already given in chapter 5.2.1. The inconsistence of our results with the results achieved by Plissard [85] can be explained by the used type of As cell, which was a solid source cell in our MBE system and a gas source cell in the MBE system of Plissard. The As from a solid source cell is provided in form of As_4, which is cracked in a high temperature process to As_2. In contrast, As from the gas source cell is provided in form of a precursor gas as AsH_3. In a high temperature process, the AsH_3 is cracked and As_2 molecules are formed. Despite the fact that both kinds of As cells nominally emit As_2, the real composition of the As fluxes might be quite different. Also an influence of the hydrogen, which is a side product of the AsH_3 cracking process, on the Ga diffusion length, as observed for MBE growth on GaAs substrates [68], might be possible. An increased Ga diffusion length would lead to an increased Ga supply of the catalyst droplet, which makes a fast consumption of the catalyst droplet by As_2 less likely. Due to the fact that the growth with As_2 leads to pronounced cluster formation in the predefined holes independent of the used As_2/Ga ratio, As_4 will be used for further experiments.

Sample number	C110627C	C110819A	C110816C
Growth temperature [°C]	593	604	623
Manipulator power [W]	93	99	108
Hole occupation number [norm.]	0.9	1	0.1
NWs in [111] dir. [norm.]	0.21	0	0
NWs not in [111] dir. [norm.]	0.10	0.02	0
Cluster density [norm.]	0.69	0.98	1

Table 5.6: Results of the temperature series for the growth on pre-structured Si substrates. Here, the Ga rate is 0.2 Å/s and the As_4 pressure 5×10^{-7} Torr. No Ga pre-deposition was performed. NW growth could only be observed for the lowest growth temperature of 593° C. 90% of the predefined holes of sample C110816C are empty.

5.2.3 Influence of the growth temperature

The pronounced cluster formation inbetween the pre-defined holes on the SiO_2 layer for the growth with As_4, which was observed in chapter 5.2.1, was attributed to a combination of the high material fluxes and the low SiO_2 layer quality. Therefore, the Ga rate was reduced to 0.2 Å/s for further experiments. Due to the lower Ga flux, the growth temperature has to be adjusted as the sticking coefficient of Ga on SiO_2 is temperature dependent [44]. Otherwise, NW growth is suppressed because the amount of Ga, which is present on the SiO_2 layer at low Ga rates and high growth temperatures is to small for the formation of Ga catalyst droplets (cf. chapter 4.1.2). To investigate the influence of the growth temperature on the NW and cluster density, a series of three samples was grown. The As_4 pressure was set to 5×10^{-7} Torr. No Ga pre-deposition was applied for this series. The results of this experiment are summarized in table 5.6.

The increase in growth temperature with increasing manipulator power seems to be reasonable. The difference in the measured values between sample C110819A and e.g. sample C110803A of chapter 5.2.2, which were grown with the same manipulator power can be explained by the different applied Ga fluxes, which are accompanied by different Ga cell temperatures. The hole occupation number is quite high for the samples C110627C and C110819A. However, NW growth could only be achieved for the lowest growth temperature of 593°C. At 604°C, only cluster growth is observed and the NW density tends to zero. At 623°C also the cluster density is strongly reduced and most of the predefined holes are empty.

The results indicate that like for the growth on untreated substrates a growth temperature of approximately 590°C is best for the applied low material fluxes. Besides that, also the assumption made in chapter 5.2.1, that the cluster formation on the

SiO_2 layer of sample C110707C is partly caused by the high material fluxes, is supported by this sample series. Here, also at lower growth temperatures the SiO_2 layer is cluster free. The decrease in NW density for the samples C110819A and C110816C is attributed to an increased reevaporation of the incoming Ga due to the increased growth temperature [44]. The lack of Ga leads to a higher effective As_4/Ga ratio and as a consequence, GaAs cluster formation is observed in the predefined holes of sample C110819A. The fact that most of the predefined holes are empty on sample C110816C is also attributed to the further increased growth temperature. Here, the Ga sticking coefficient is so low that the amount of Ga in the predefined holes was not sufficient for the GaAs cluster formation.

5.2.4 Conclusion

We found that the Ga pre-deposition procedure works well for the growth of GaAs NWs on pre-structured Si substrates. A Ga droplet with a diameter of approximately 80 nm is formed in every predefined hole during the pre-deposition procedure, independent of the hole pitch. The sample morphology after NW growth depends mainly on the used As species. For As_2, predominantly clusters are grown in the predefined holes while NW growth is suppressed. The SiO_2 layer between the predefined holes is free of clusters. This result holds for different As_2/Ga ratios. It can be explained by the rapid consumption of the accumulated Ga atoms in the predefined holes due to the used As species. The As_2 inhibits the formation of Ga catalyst droplets, if no Ga pre-deposition was applied or consumes the existing Ga catalyst droplets, if Ga pre-deposition was applied. For As_4 the case is reversed. Here, the cluster density is low and predominantly NWs are grown in the predefined holes. However, a massive cluster formation is observed on the SiO_2 layer between the predefined holes. The growth of NWs instead of clusters can be explained by the slower consumption of the catalyst droplets by As_4. The massive growth of clusters on the SiO_2 layer is attributed to a combination of the high material fluxes and the low quality of the SiO_2 layer. The grown NWs are oriented in the [111] direction perpendicular to the substrate and in random directions. The reason for this behavior is attributed to a thin SiO_2 layer at the bottom of the predefined holes, which partly inhibits the contact between NWs and substrate. The SiO_2 layer is most likely formed by natural oxidation when the sample is transferred from the etching setup to the MBE system. The best growth temperature for low Ga rates of 0.2 Å/s is, like for the growth on untreated substrates, 590°C. At higher growth temperatures NW growth is suppressed. This is explained by the temperature dependent sticking coefficient of Ga on SiO_2 [44], which leads to an increase of the effective As_4/Ga ratio in the

predefined holes and thereby to cluster formation. At higher growth temperatures the whole incoming Ga is immediately reevaporated from the SiO_2 layer and only empty predefined holes are observed. We want to mention that this result is only valid for low Ga rates. At high Ga rates of e.g. one monolayer per second NW growth is also observed at high growth temperatures of 630°C.

5.3 Growth on pre-structured GaAs substrates

For the growth on pre-structured GaAs substrates, a sputtered SiO_2 layer with an initial layer thickness between 15 nm and 35 nm was used. The substrate preparation procedure is nearly the same as for the thermal SiO_2 layer on Si substrates. Some parameters like the etching time have to be adjusted as the etching rate of thermal and sputtered SiO_2 differ significantly. For a more detailed description of the sample layout and preparation procedure see [3, 46].

5.3.1 Influence of the Ga pre-deposition

To investigate the influence of the Ga pre-deposition procedure on the sample quality for a sputtered SiO_2 layer, three different samples were grown. On every sample, nine different hole grids with different hole pitches were fabricated by e-beam lithography and lift off. The hole pitches were 200 nm, 250 nm, 500 nm, 1000 nm and 2000 nm. Two different electron doses are used for each hole pitch except for the hole pitch of 2000 nm. The amount of pre-deposited Ga was at first calculated such that Ga droplets with a diameter of 80 nm could be formed at medium hole pitch of 500 nm, assuming Ga diffusion on the SiO_2 layer and a Ga sticking coefficient of one. Due to the fact that the hole density, which is a parameter in the calculation is different for different hole pitches, the pre-deposited Ga exceeds the amount of required Ga for larger hole pitches and deceeds it for smaller hole pitches, respectively. For sample C090826A, the 2D equivalent amount of 36 Å Ga was deposited at 433°C substrate temperature. During the deposition sequence, the substrate temperature was raised to 540°C and NW growth was started. The low deposition temperature was chosen to prevent Ga re-evaporation from the substrate. This approach seems to be appropriate because the Ga rate of 0.2 Å/s for the pre-deposition procedure was very small and as a consequence the pre-deposition time was quite long. For the samples C091001A and C091104B the amount of pre-deposited Ga was reduced to 24 Å. Additionally, the Ga pre-deposition procedure was performed at the growth temperature for sample C091104B. For NW growth, the standard As_4 and Ga fluxes were used. The applied values are summarized in table 5.7.

Sample number	C090826A	C091001A	C091104B
Amount of deposited Ga [Å]	36	24	24
Deposition time [sec.]	180	120	120
Deposition temperature [°C]	433	431	596
Growth temperature beg. [°C]	540	510	602
Growth temperature end [°C]	585	587	602

Table 5.7: Ga pre-deposition parameters for the growth on GaAs substrates. With respect to sample C090826A, the amount of deposited Ga was reduced for sample C091001A and sample C091104B. Additionally, the deposition and growth temperature was raised for sample C091104B.

Sample C090826A shows a pronounced cluster formation on the SiO_2 layer for all hole pitches. The clusters grow together and form a nearly closed GaAs layer. The NWs grow randomly on the SiO_2 surface and on the clusters. Besides the clusters, also Ga puddles can be found on the substrate. The Ga puddles disappear on sample C091001A but the cluster formation is even more pronounced than on sample C090826A. Here, the clusters form a closed GaAs layer which is very rough. Like on sample C090826A the NWs grow in random directions. The cluster growth disappears on sample C091104B. However, also the growth of NWs is totally suppressed and only empty predefined holes are visible on the SiO_2 layer.

The origin of the Ga puddles on sample C090826A is attributed to the relatively large amount of pre-deposited Ga. Therefore, the amount was reduced from 36 Å to 24 Å for sample C091001A. As a consequence, the Ga puddles disappear but the cluster density was still very high. The origin of the cluster formation is the high sticking coefficient and the low diffusion length of Ga [44,60] at the low growth temperatures, which are present at the beginning of the NW growth. Due to the fact that the NW growth was started immediately after the Ga pre-deposition procedure, the time was too short to heat the sample from the deposition temperature to the growth temperature. To get rid of the cluster formation, the Ga pre-deposition temperature was set to growth temperature for sample C091104B, although this implies the possibility that due to the low Ga flux all the pre-deposited Ga is immediately reevaporated from the SiO_2 surface. The lack of cluster and NW growth seems to confirm this expectation. However, a closer investigation of sample C091104B revealed that a SiO_2 layer is present on the delimiter strips between the hole grids. This indicates that the holes in the SiO_2 layer were not etched down to the substrate, which would also explain the lack of cluster and NW growth in the predefined holes. We conclude that further investigations are necessary to examine the applicability of the Ga pre-deposition procedure on GaAs substrates for low Ga fluxes.

Sample number	C101118B	C101108A	C101013A	C101028A	C101111A
As_4/Ga ratio	1.4	2.4	2.8	3.4	4.4
Ga rate [Å/s]	0.20	0.21	0.20	0.20	0.21
As_4 flux [10^{-6} Torr]	0.26	0.44	0.5	0.61	0.79
Growth temp. [°C]	594	593	596	594	593

Table 5.8: Growth parameters for the As_4/Ga ratio series. To vary the As_4/Ga ratio, the Ga flux was kept constant at 0.2 Å/s and the As_4 pressure was increased from 0.26×10^{-6} Torr to 0.79×10^{-6} Torr. The growth temperature was kept constant at approximately 595° C for all samples. No Ga pre-deposition was performed.

5.3.2 Influence of the As_4/Ga ratio

Next, the influence of the As_4/Ga ratio on the NW morphology and the hole occupation number was investigated. For this experiment, samples with eight different hole grids per sample were used. The hole pitches of the hole grids were 250 nm, 500 nm, 750 nm, 1000 nm, 1250 nm, 1500 nm, 1750 nm and 2000 nm. The As_4/Ga ratio was changed by keeping the Ga rate fixed at 0.2 Å/s and varying the As_4 flux. Seven different values for the As_4/Ga ratio were investigated. The samples with the lowest (1.0) and the highest (5.4) As_4/Ga ratio were excluded from the analysis due to their inferior sample quality. The growth temperature was in the range of 593°C to 596°C. The growth parameters are summarized in table 5.8.
The NW morphology as well as the hole occupation number strongly depend on the applied As_4/Ga ratio and the hole pitch. Therefore, every hole grid with different hole pitch was evaluated separately. The results for the NW length and the inversely NW tapering (which we refer to as NW tapering) are summarized in figure 5.5.
The NW length is increasing for increasing As_4/Ga ratios and decreasing hole pitches. For large hole pitches and high As_4/Ga ratios (e.g. As_4/Ga ratio of 13.5, sample not listed above) the NW growth is totally suppressed and only cluster formation is observed (cf. figure 5.4 (d)). The NW diameter (not shown in figure 5.5) is first increasing, reaches a maximum at a hole pitch of 500 nm or 750 nm and is then decreasing with increasing hole pitch. The value for the NW diameter varies between 70 nm and 160 nm. The NW tapering is decreasing for increasing As_4/Ga ratios and decreasing hole pitches.
The increase in NW length with increasing As_4/Ga ratio is attributed to the As_4 determined NW growth (cf. chapter 4.1.4). The decrease of the NW length with increasing hole pitch will be discussed in the next section. The variance of the NW diameter with increasing hole pitch is still an open question. Due to the fact that this trend was observed on all samples, a correlation to the sample preparation

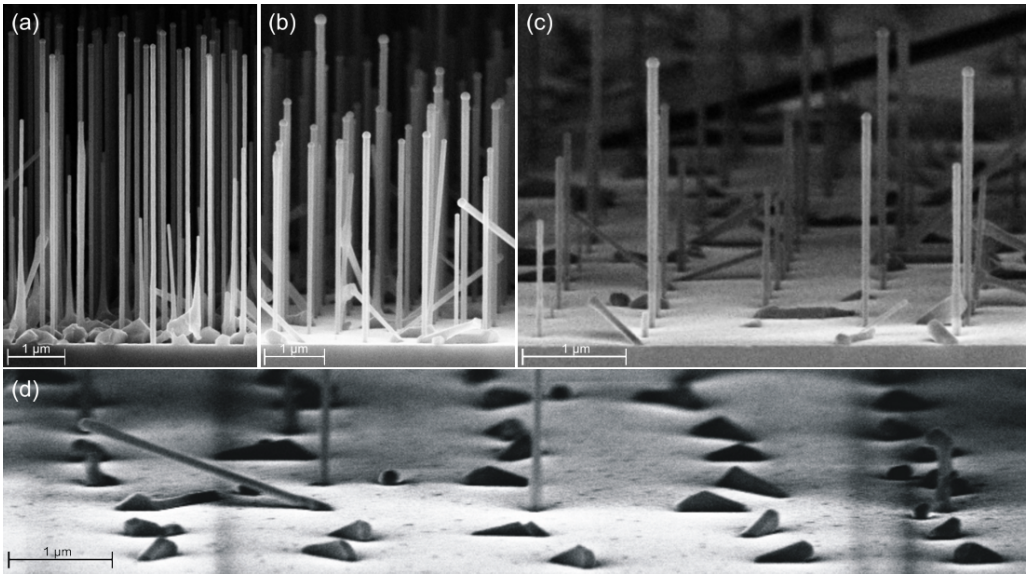

Figure 5.4: SEM side view images of NW fields with different hole pitches of (a) 200 nm, (b) 500 nm, (c) 1 µm and (d) 2 µm. The NW length decreases for increasing hole pitches. At a hole pitch of 2 µm, NW growth is almost completely suppressed and the formation of clusters in the predefined holes is observed.

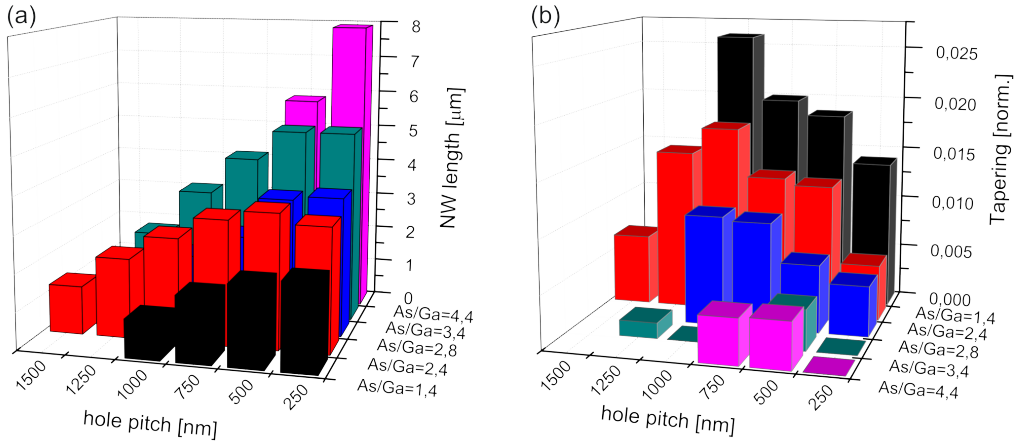

Figure 5.5: (a) NW length with respect to the As_4/Ga ratio and the hole pitch, (b) NW tapering with respect to the As_4/Ga ratio and the hole pitch. Note that the axis for the As_4/Ga ratio is reversed on figure 5.5 (b).

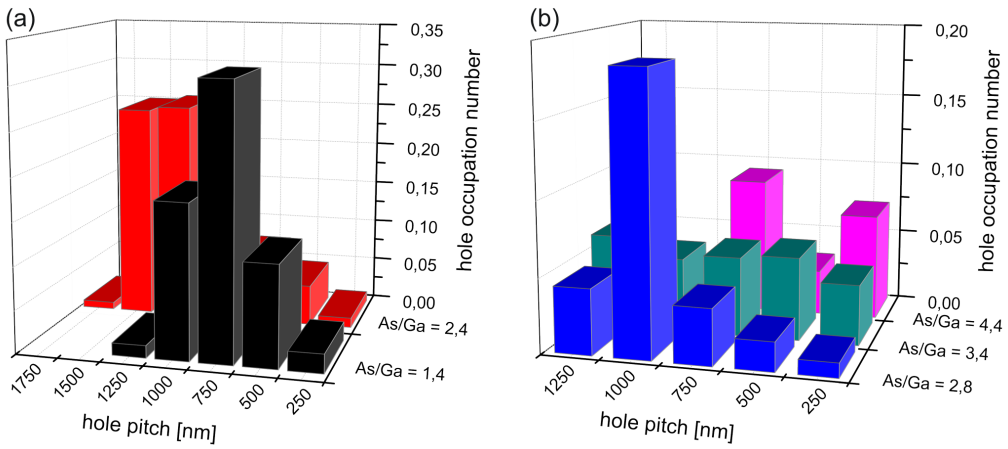

Figure 5.6: Hole occupation number with respect to the hole pitches for an As_4/Ga ratio of (a) 1.4 and 2.4 and (b) 2.8, 3.4 and 4.4.

procedure seems to be likely. From other experiment (not shown here) we know that the catalyst droplet diameter is correlated with the predefined hole diameter. A change in hole diameter can be caused e.g. by the proximity effect or by a slight misalignment of the sample during the e-beam lithography step. The decrease of the NW tapering with increasing As_4/Ga ratio was already observed on unstructured samples (cf. chapter 4.1.4). The increase of the NW tapering with increasing hole pitch at a fixed As_4/Ga ratio will be discussed in the next section.

Figure 5.6 shows the hole occupation number with respect to different As_4/Ga ratios and hole pitches. The absolute values for the hole occupation number are decreasing with increasing As_4/Ga ratios. The highest value for the hole occupation number is 0.3 for an As_4/Ga ratio of 1.4 and a hole pitch of 750 nm. The distribution of the hole occupation number for a fixed As_4/Ga ratio shows first an increase for small hole pitches, than a maximum and then a decrease for larger hole pitches. The maximum value of the hole occupation number seems to shift to larger hole pitches for increasing As_4/Ga ratios.

The low values for the hole occupation numbers are attributed to parasitic two dimensional GaAs cluster growth. Due to the fact that no Ga pre-deposition was applied for the growth on GaAs substrates, the formation of Ga catalyst droplets occurs during the NW growth process, when As_4 is already present in the growth chamber. The presence of As_4 reduces the probability for the Ga droplet formation because Ga is consumed by the As_4 before Ga catalyst droplets can be formed. This process is enhanced with increasing As_4 pressure. As a consequence, the hole occupation number is higher for small As_4/Ga ratios than for larger ones. The distribution of the hole occupation numbers at a fixed As_4/Ga ratio and the shift

of the maximum in the hole occupation number with increasing As_4/Ga ratio can - like the increase in NW length with decreasing hole pitch and the increase in NW tapering with increasing hole pitch - not easily be explained. For this purpose, a modification of the present growth model is necessary.

5.3.3 Modification of the current growth model

Until now it was assumed that Ga is collected by the catalyst droplet directly from the incoming Ga flux and by surface diffusion over the substrate and the NW side facets during NW growth. In contrast, it is assumed that As_4 can only be collected by the catalyst droplet directly from the incoming As_4 flux because surface diffusion of As_4 seems to be negligible. Due to the fact that the probability for the formation of a nucleus on the NW-droplet boundary depends on the As concentration in the catalyst droplet [38], NWs originating from smaller droplets should grow faster than NWs originating from bigger droplets because the As concentration necessary for the nucleus formation is obtained much faster for smaller droplets [72]. If we apply this growth model to our results, a dependence of the NW length on the droplet diameter, which differs significantly between 70 nm and 160 nm for different hole pitches, is expected. However, this was not observed. In contrast, a dependence of the NW length on the hole pitch was found. This can only be explained if a constant As reservoir for each NW and a Ga diffusion length of the order of the hole pitches is assumed. The second condition is confirmed by literature [60].

To provide a constant As reservoir independent of the catalyst droplet diameter, surface diffusion of As_4 has to be taken into account. The As_4 diffusion length has to be smaller than the Ga diffusion length, which is of the order of a few hundred nanometer at our growth conditions [60]. If we apply these diffusion parameters to our sample geometry with hole pitches between 250 nm and 2000 nm, every NW has his own As_4 reservoir but shares the Ga reservoir with his neighboring NWs for small hole pitches. This results in an increased effective As_4/Ga ratio for small hole pitches because the amount of obtainable Ga for each single NW is reduced. For larger hole pitches the overlap of the Ga reservoirs of the single NWs decreases and at very large hole pitches every NW has its own Ga reservoir. As a consequence of the different Ga and As_4 diffusion lengths, the effective As_4/Ga ratio has its maximum at the smallest hole pitch and decreases for increasing hole pitches. Due to the fact that the NW growth is As determined, an increase of the As_4/Ga ratio leads to an increase in NW length (cf. chapter 4.1.4). At the largest hole pitches the As_4/Ga ratio can be so low that the NW growth is totally suppressed. Here, the Ga droplets, which are formed in the predefined holes are most likely consumed by As_4 during

the growth termination procedure and the formation of GaAs clusters is observed.
With the same model, also the distribution of the hole occupation number with respect to the hole pitches at a fixed As_4/Ga ratio could be explained. At small hole pitches, the local growth conditions are too As_4 rich. Therefore, the formation of clusters is enhanced and the NW density is low. With increasing hole pitches the growth conditions become more Ga rich and the As_4/Ga ratio reaches its optimum value for NW growth. As a consequence, also the hole occupation number reaches its maximum value. With further increasing hole pitches, the NW growth conditions become too Ga rich and the hole occupation number decreases. According to this theory, an increase of the As_4/Ga ratio should lead to a shift of the field with the maximum occupation number to larger hole pitches. This is exactly what we observe in our experiments. Also the decrease in NW tapering with decreasing hole pitches at a fixed As_4/Ga ratio is consistent with the As_4 diffusion model. As mentioned above, the effective As_4/Ga ratio becomes more Ga rich for increasing hole pitches. The increased amount of Ga in the catalyst droplet cannot immediately be incorporated into the NW and leads to an increase of the catalyst droplet volume. As a consequence, a pronounced NW tapering is observed for large hole pitches.

5.3.4 Conclusion

In conclusion we found that the Ga pre-deposition procedure is not appropriate to increase the hole occupation number of Ga catalyzed NWs on sputtered SiO_2. Instead of NWs, only GaAs clusters are grown in the predefined holes and on the SiO_2 layer if the Ga pre-deposition procedure is performed at low deposition temperatures. The origin of the cluster growth is attributed to the low growth temperatures, which were present at the beginning of the NW growth. Due to the high sticking coefficient of Ga on SiO_2, which is unity for growth temperatures below 570°C [44] and the short migration length of Ga, which is between 90 nm and 150 nm for this temperature range [60], the nucleation of GaAs on the SiO_2 layer is not longer suppressed and cluster formation is the consequence. Despite the fact that the cluster formation disappears at high deposition temperatures, also the NW growth is suppressed. This was first attributed to reevaporation of the pre-deposited Ga due to the high pre-deposition temperature. However, a closer investigation revealed that the predefined holes in the SiO_2 layer were probably not etched down to the substrate, which could also explain the absence of NW and cluster growth. Further investigations are required to resolve this question.
Furthermore we found that a change in the As_4/Ga ratio leads to a change of the hole occupation number and the NW morphology. On a sample with different hole

grids the NW length increases with increasing As_4/Ga ratio and decreasing hole pitches. The NW diameter is not correlated to the As_4/Ga ratio and shows a non monotonic behavior for increasing hole pitches. The NW tapering is decreasing for an increasing As_4/Ga ratio and decreasing hole pitches. The hole occupation number shows a Gaussian like distribution for different hole pitches at a fixed As_4/Ga ratio. The maximum of the hole occupation number seems to shift towards larger hole pitches for an increasing As_4/Ga ratio.

The increase in NW length and the decrease in NW tapering with increasing As_4/Ga ratio can be explained within the current growth model by the As_4 determined NW growth. To explain the decrease of the NW length with increasing hole pitch, the cluster formation for very large hole pitches, the increase of NW tapering with increasing hole pitches, the distribution of the hole occupation number for different hole pitches at a fixed As_4/Ga ratio and the shift of the maximum hole occupation number with increasing As_4/Ga ratio the growth model had to be modified. In contrast to the present growth model, As_4 diffusion on the SiO_2 layer and the NW side facets is assumed with an As_4 diffusion length smaller than the diffusion length of Ga. Under this assumption, all of our observations can be explained. In addition, the statements made for the NW length and tapering, which are based on the old growth model are consistent under the new growth model.

Finally we want to note that just recently a alternative model was proposed which assumes the re-evaporation of As from the substrate and the NW side facets and the absorption at the NW catalyst droplet [86]. This theory, which treats the substrate and the NW side facets as secondary As sources, can qualitatively explain most of our observations. However, some results like the strong increase in NW length with respect to the applied As_4 pressure [4] are not in accordance with this model.

Chapter 6

NW heterostructures: Magnetic NWs

In this chapter we investigate the magnetic properties of GaMnAs grown on (110) oriented GaAs substrates, the structural and magnetic properties of GaAs/GaMnAs core shell NWs and the influence of a post growth annealing procedure on the magnetic properties of the NW heterostructures.
The first step was to optimize the GaMnAs growth parameters for the crystal orientation of the NW side facets. As shown in [97], our NWs reveal predominantly (1120)/(110) side facets for the WZ/ZB crystal phase, respectively. Therefore, the growth of GaMnAs on (110) oriented GaAs substrates was optimized with respect to the GaMnAs layer quality and Curie temperature.
Next, GaAs/GaMnAs core shell heterostructures were fabricated. For the growth of the GaAs core NWs, the Au catalyzed growth technique was used because pure WZ and ZB core NWs can only be obtained with this technique [100]. For the growth of the GaMnAs shell, the growth temperature was reduced below 300°C to suppress the segregation of MnAs [89]. Additionally, the growth in the axial direction is inhibited because the catalyst droplet is not liquid in this temperature regime [28]. This ensures a proper GaMnAs shell growth around the GaAs core NW. The obtained NW heterostructures are investigated with respect to their structural and magnetic properties.
Finally, the GaAs/GaMnAs core shell NWs are annealed in a NW annealing oven to reduce the amount of Mn interstitial defects and thereby increase the Curie temperature. The annealing experiments were performed in a temperature regime between 152°C and 277°C.

6.1 Optimizing GaMnAs growth on (110) oriented GaAs substrates

For the optimization of GaMnAs growth on (110) oriented GaAs substrates, two 5x10 mm^2 sample pieces were mounted on the NW sample holder. To ensure an equal growth temperature for the GaMnAs layers and the GaMnAs shells without readjusting the manipulator power, the same sample holder was used for both experiments. The sample pieces were cleaned with Acetone and Propanol and then transfered to the MBE system. The native GaAs oxide was desorbed at approximately 620°C for 15 minutes. The oxide desorption was monitored with RHEED. To provide a flat substrate surface for the GaMnAs layer growth, a 30 nm thick GaAs buffer layer was grown at 540°C, using a Ga rate of 0.4 Å/s and an As_4 flux of 6.9×10^{-6} Torr, yielding an As_4/Ga ratio of 20. The quality of the buffer layer was monitored with RHEED. Next, the growth temperature was reduced for the GaMnAs layer growth. During this step, the manipulator power was adjusted until the target temperature and the measured temperature did not differ from each other more than 1°C. In addition, the temperature was only regarded as stable if the temperature change over time was less than 1°C in five minutes. After the temperature stabilization, a 30 nm thick GaMnAs layer was grown with a Ga rate of 0.4 Å/s at different growth temperatures. High As_4/Ga ratios between 10 and 20 were used to meet the special requirement of 2D layer growth on (110) oriented GaAs substrates. To compensate the heat input from the Ga and Mn cells, the manipulator power was changed in three steps as described in chapter 3.2.2. After the growth, the GaMnAs samples were again monitored with RHEED. To investigate the contact and sheet resistivity at room temperature and at helium temperature as well as the Curie temperature, the 10x5 mm^2 sample pieces were cut to a size of 5x5 mm^2 and mounted on a sample carrier as described in chapter 3.5.2. The measurements were performed in the dewar measurement setup.

6.1.1 Adjusting the growth temperature and As_4/Ga ratio

For the first sample series, the As_4/Ga ratio was set to 20 and the Mn content was fixed at 3.5%. The GaMnAs growth temperature was varied between 240°C and 300°C. The results are summarized in table 6.1.
The samples grown at 240°C, 260°C and 280°C show a streaky two dimensional RHEED pattern after growth which indicates that the sample surface is smooth and no MnAs segregation has occurred. In contrast, the samples grown at 290°C and 300°C showed a three dimensional RHEED pattern which indicates the formation

Growth T [°C]/ As_4/Ga ratio	240	260	280	290	300
20	insulating	insulating	51 K	3D	3D
15	-	-	50 K	-	-
12.5	-	-	57 K*	-	-
10	-	-	3D	-	-

*Table 6.1: Sample properties for different As_4/Ga ratios and growth temperatures at a fixed Mn content of 3.5%. The temperature window for the growth of ferromagnetic GaMnAs is very small. The As_4/Ga ratios has no influence on the Curie temperature until a transition from a streaky to a three dimensional RHEED pattern is observed (indicated by *).*

of MnAs clusters [89]. An example for a two and three dimensional RHEED pattern is given in figure 6.1 (a) and (d). The measurement of the sample resistivity during the warm up process revealed that the samples grown at 240°C and 260°C become insulating at low temperatures and did not show a singularity in the first derivation of the resistivity curve [73], i.e. that no ferromagnetic phase transition occurred in these samples. The sample grown at 280°C showed a ferromagnetic phase transition with a Curie temperature of 51 K.

An example of a cooling curve for an insulating and a ferromagnetic GaMnAs sample is given in figure 6.2 (a) and (c). The samples grown at 290°C and 300°C are not measured due to the MnAs cluster formation, which was observed in RHEED. We conclude that the growth window for GaMnAs layers at a high As_4/Ga ratio of 20 and a Mn content of 3.5% is very small. Only the sample grown at 280°C showed a smooth layer surface *and* a ferromagnetic phase transition with a T_C of 51 K. The samples grown at lower growth temperatures become insulating at low temperatures and did not show a ferromagnetic phase transition while the samples grown at higher growth temperatures show a rough surface in RHEED, which indicates MnAs segregation.

Next, we investigate the influence of the As_4/Ga ratio on the sample properties. Therefore, the growth temperature was fixed at 280°C and the Mn content was set to 3.5%. Three samples with an As_4/Ga ratio of 15, 12.5 and 10 were grown. The results are summarized in table 6.1. The sample with an As_4/Ga ratio of 15 showed a streaky RHEED pattern and a Curie temperature of 50 K. The sample with an As_4/Ga ratio of 12.5 revealed a transition from a two dimensional to a three dimensional RHEED pattern as shown in figure 6.1 (b) and (c). This indicates that MnAs segregation has already started but was not very pronounced. The T_C of this sample was 57 K. The characteristic cooling curve is shown in figure 6.2 (d).

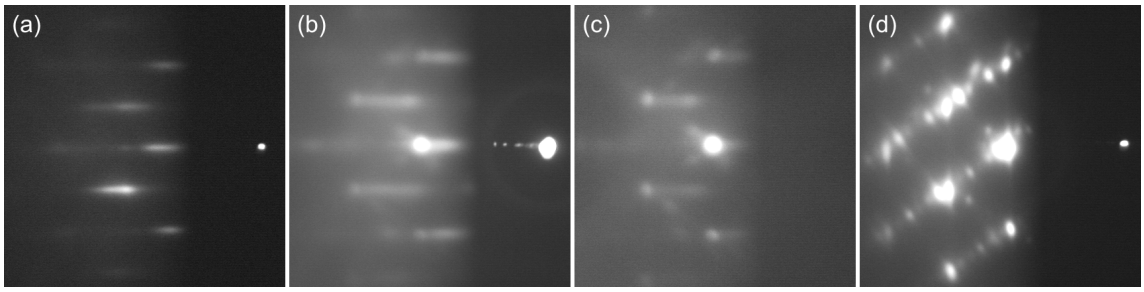

Figure 6.1: RHEED pattern for different growth conditions of GaMnAs on (110) oriented GaAs substrates. (a) Streaky RHEED pattern which is characteristic for a smooth GaMnAs layer surface. (b) Streaky RHEED pattern under a small angle of incidence of the electron beam and (c) three dimensional RHEED pattern of the same sample under a larger angle of incidence. The RHEED pattern of figure 6.1 (b) and (c) are characteristic for a sample with a beginning MnAs segregation. (d) Three dimensional RHEED pattern which indicates a distinct MnAs cluster formation.

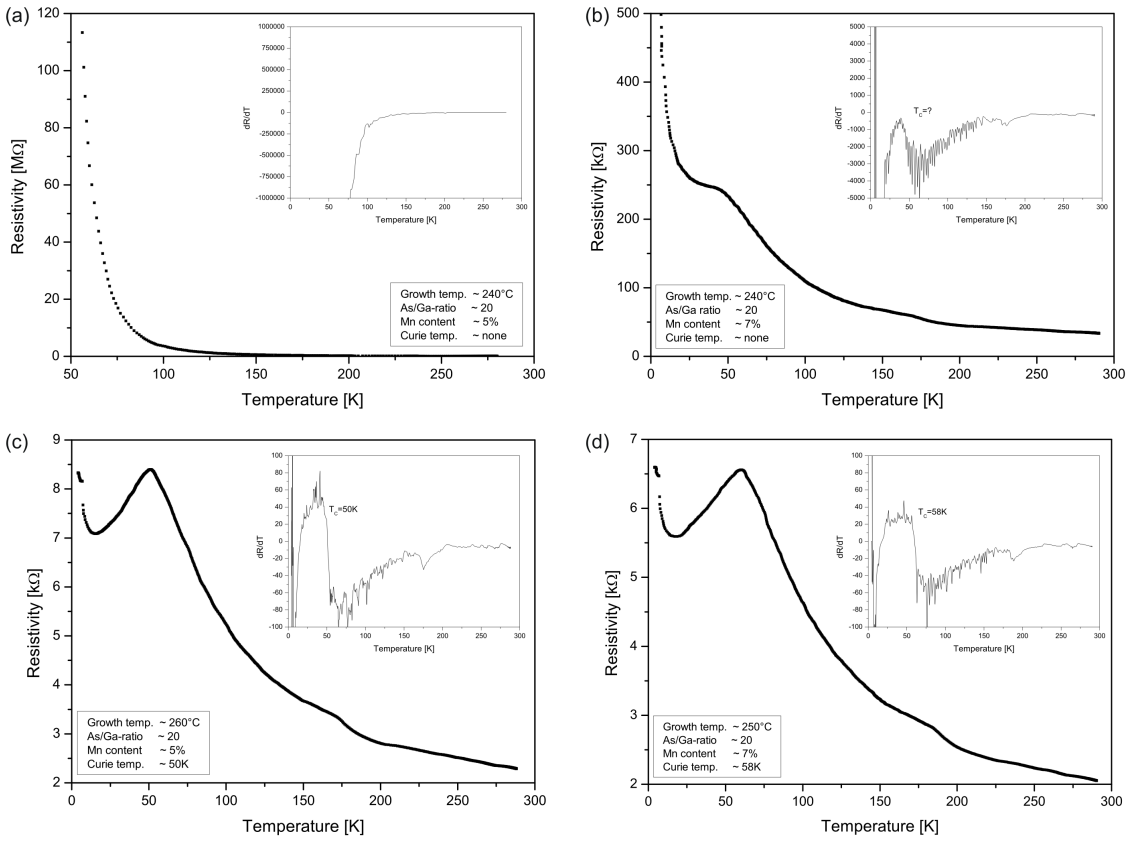

Figure 6.2: (a) Cooling curve for an insulating sample, (b) cooling curve for a semi insulating sample, (c) cooling curve for a ferromagnetic GaMnAs sample and (d) cooling curve for a ferromagnetic sample which exhibits the onset of MnAs segregation in RHEED. The inset shows the corresponding first derivatives dR/dT of the cooling curves.

Growth T. [°C]/ Mn content [%]	240	250	260	280	300	310
2	-	-	-	insulating	52 K	3D
3.5	insulating	-	insulating	51 K	3D	-
5	insulating	-	50 K	3D	-	-
7	semi-ins.	58 K*	-	-	-	-

*Table 6.2: Sample properties for different Mn contents and growth temperatures at a fixed As_4/Ga ratio of 20. Again the temperature window for the growth of ferromagnetic GaMnAs is very small for all Mn contents. The Curie temperature is very similar for all Mn contents until a transition from a streaky to a three dimensional RHEED pattern is observed (indicated by *).*

The sample with an As_4/Ga ratio of 10 showed a three dimensional RHEED pattern. Therefore, the Curie temperature was not determined. We concluded that the Curie temperature does not depend on the As_4/Ga ratio until MnAs segregation is started. As a consequence, the As_4/Ga ratio was set to 20 for the following experiments.

6.1.2 Adjusting the Mn content

Now we investigate the influence of the Mn content on the sample properties. For this experiment a series of eleven samples with Mn contents of 2%, 3.5%, 5% and 7% were grown. The As_4/Ga ratio was set to 20 for all samples and the growth temperature was varied between 240°C and 310°C. The results are summarized in table 6.2.

We found that the growth window for ferromagnetic GaMnAs samples is very narrow independent of the used Mn content. For a Mn content of 2%, a ferromagnetic GaMnAs sample with a T_C of 52 K was obtained at a growth temperature of 300°C. For a Mn content of 3.5% and 5%, ferromagnetic GaMnAs samples with Curie temperatures of 51 K and 50 K were obtained at growth temperatures of 280°C and 260°C, respectively. If the growth temperature is slightly increased, the RHEED pattern becomes three dimensional for all three samples, which indicates MnAs cluster formation. In contrast, if the growth temperature is slightly reduced, the samples become insulating at low temperatures.

No appropriate GaMnAs sample could be obtained for a Mn content of 7%. The sample grown at 240°C shows a semi insulating behavior, i.e. the sample resistivity increases with decreasing measurement temperatures but the sample did not become insulating at 4 K. Despite that, no singularity was found in the first derivative of the resistivity curve (cf. figure 6.2 (b)). The sample grown at 250°C shows a T_C of 58 K but also the onset of MnAs cluster formation was observed in RHEED. A

third sample, which is not listed in table 6.2 was grown with a Mn content of 7%, a growth temperature of 240°C and an As_4/Ga ratio of 15. Due to the fact that the RHEED investigation revealed a three dimensional pattern, the Curie temperature for this sample was not investigated.

To summarize, GaMnAs samples which show a two dimensional RHEED pattern *and* a ferromagnetic phase transition could be fabricated in a very small growth window for Mn contents between 2% and 5%. In contrast to our expectations, the Curie temperature did not increase with increasing Mn content but was approximately 50 K for all samples. The growth temperatures of the ferromagnetic samples shift towards smaller values for increasing Mn contents. For a Mn content of 7%, the samples show either a semi insulating behavior and a streaky RHEED pattern or a Curie temperature of 58 K and a three dimensional RHEED pattern.

6.1.3 Conclusion

We conclude that the Mn content has to be in the order of 2% to 5% for the successful fabrication of ferromagnetic GaMnAs layers on (110) oriented GaAs substrates. Within this range, the Curie temperature for all samples was approximately 50 K independent of the Mn content. To achieve a good crystal quality, indicated by a streaky RHEED pattern *and* a ferromagnetic phase transition at low temperatures, the GaMnAs growth temperature has to be decreased for increasing Mn contents. The origin of this result is complex and can be explained if a temperature dependent sticking coefficient of As_4 on (110) oriented GaAs and a Mn concentration dependent MnAs formation rate are taken into account. The temperature dependent sticking coefficient of As_4 seems at first to be in contradiction with the results obtained by Foxon [32], who found that the As_4 sticking coefficient is temperature independent in the temperature regime of 177°C to 327°C for the growth on (100) oriented GaAs in the presence of a high Ga flux. However, Foxon also found that for low As_4 fluxes the As_4 sticking coefficient is temperature dependent in the absence of a Ga flux. Due to the fact that the Ga flux in our experiments is very low compared to the Ga flux of the experiments performed by Foxon, we believe that we are in a regime where the As_4 sticking coefficient is temperature dependent.

If this assumption is made, we can argue as follows. For samples with a low Mn concentration, the formation of MnAs occurs only at very high growth temperatures. The sticking coefficient of As_4 is reduced and the As_4 diffusion length is increased in this temperature regime. As a result, the amount of As antisites is small and the formation of ferromagnetic GaMnAs can occur at high growth temperatures, despite the low Mn concentration. In contrast, if the Mn concentration is high, the MnAs

formation occurs at lower temperatures and the GaMnAs growth temperature has to be reduced. In this temperature regime, the amount of As antisites is increased due to the higher As_4 sticking coefficient and the lower As_4 diffusion length. However, the increased amount of As antisites can be compensated by the higher Mn concentration. As a result, the formation of a ferromagnetic phase in GaMnAs is possible for higher Mn concentration at lower growth temperatures. The limit for this compensation between As antisites and Mn concentration is reached at a Mn concentration of 7%. To achieve a smooth GaMnAs layer, the growth temperature has to be reduced to a value where the As antisite formation is strongly increased. This increase can not be compensated by the increased Mn concentration of this sample. If the amount of As antisites is reduced by decreasing the As_4/Ga ratio or by increasing the growth temperature, the formation of MnAs clusters is observed in RHEED. We want to note that the increase in Mn interstitial defects with increasing Mn content [113] can also reduce the Curie temperature. Due to the fact that this effect is found on substrates where T_C is increased with increasing Mn content, it cannot be the dominant factor for the observed behavior in our experiments.
Finally we want to note that a GaMnAs optimization series was also grown for low As_4/Ga ratios on (110) oriented GaAs substrates. The series contains seven samples with two different values for the Mn content, two different As_4/Ga ratios and three different growth temperatures. Due to the low As_4 pressure, the applied GaMnAs growth temperatures were much lower than the growth temperatures for this series. However, it was not possible to grow a sample which shows a streaky RHEED pattern *and* a ferromagnetic phase transition at low temperatures. Therefore, this approach was no longer pursued.

6.2 Growth of GaAs/GaMnAs core shell NWs

In this chapter we apply the optimized parameters for the growth of GaMnAs on (110) oriented GaAs substrates to the growth of a GaMnAs shell around GaAs core NWs with predominantly (110)/(1120) oriented side facets. We found that the growth conditions on (110) oriented GaAs substrates differ significantly from the growth conditions on the NW side facets. Therefore, an adaptation of the GaMnAs growth parameters was necessary. After the growth parameters were adjusted, the obtained core shell NWs are investigated with respect to their structural and magnetic properties. In our structural investigations we examine the interface region between the core NW and the GaMnAs shell, the morphology of the GaMnAs shell with respect to the morphology of the GaAs core NW and the distribution of Mn in the GaMnAs shell. In the magnetic investigations we focus on the magnetic

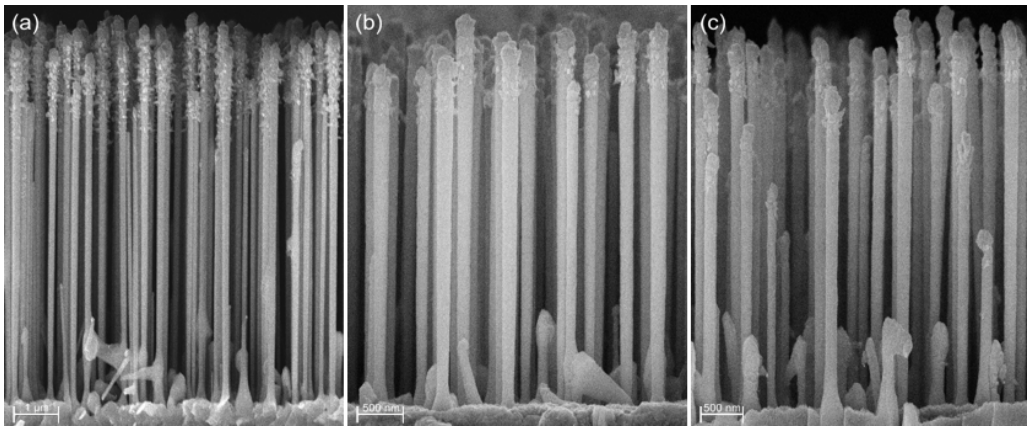

Figure 6.3: SEM side view image of (a) sample C110803B, (b) sample C110808B and (c) sample C110804A. The GaMnAs shells were grown at 240° C, 225° C and 220° C, respectively. The quality, i.e. the smoothness and homogeneity of the shell increases from (a) to (c).

anisotropy and the Curie temperature of the GaAs/GaMnAs core shell NWs. The observed behavior of the magnetic anisotropy in magnetotransport measurements is explained by introducing an effective magnetic field.

6.2.1 Adjusting the GaMnAs growth parameters

Despite the fact that the NW side facets exhibit predominantly the (110)/(1120) crystal orientation, the GaMnAs growth conditions on the side facets differ significantly from the growth conditions on (110) oriented GaAs substrates. This is attributed to the special geometry of the NW side facets [97], which will be discussed later in this chapter. As a consequence, the growth parameters have to be adjusted for the growth of GaMnAs on the NW side facets. For this purpose, a series of eighteen samples was grown. For the following investigation, we will focus on samples with a ZB core NWs. As shown in chapter 6.1 the Curie temperature of GaMnAs layers is independent from the used Mn content as long as the growth temperature is adjusted properly. For our first experiments we use a Mn content of 3.5% and an As_4/Ga ratio of 20. The growth temperature, which was 280°C for a 2D GaMnAs layers, was reduced in three steps from 240°C to 225°C and finally to 220°C until the GaMnAs shell exhibits a uniform morphology. Figure 6.3 shows SEM side view images of the three samples.
A ferromagnetic phase transition at low temperatures was not observed for the three GaAs/GaMnAs core shell NW samples in magnetotransport measurements. Therefore, the As_4/Ga ratio was reduced from 20 to 1.5 while the other growth parameters were kept constant. A decrease in the As_4/Ga ratio leads to a decrease

of As antisites and as a consequence the hole concentration in the GaMnAs shell, which has to exceed a certain value for a ferromagnetic phase transition, is increased. Despite the fact that the GaMnAs shell exhibits a homogeneous morphology at an As_4/Ga ratio of 1.5 and a growth temperature of 225°C, the sample did not show a ferromagnetic phase transition at low temperatures. As a consequence, the Mn content was increased to 5% while the As_4/Ga ratio was kept at 1.5. The increase in Mn content reduces the distance between the Mn atoms and increases the hole density. To avoid MnAs segregation, the growth temperature had to be reduced. Again, a series of three samples with different growth temperatures of 210°C, 200°C and 190°C was fabricated. Only the sample grown at 190°C exhibits a homogeneous morphology of the GaMnAs shell. Using these growth parameters, a GaMnAs shell was grown around pure WZ core NWs. For the mixed WZ/ZB NWs the same growth parameters were used but the growth temperature was nominally increased by 15°C.

The difference in nominal growth temperature for the mixed WZ/ZB NWs can be explained by the different temperature measurement device, which was a pyrometer instead of the usually used bandgap absorption spectrometer. Due to our small sample size and the continuous sample rotation during growth, the values obtained from the pyrometer temperature measurement fluctuate significantly and a mean value has to be calculated. The calculated mean value is converted to a bandgap absorption spectrometer temperature, using a calibration curve. Both, the mean value calculation and the temperature conversion introduce a certain error to the temperature value. Therefore, it seems reasonable to assume that the mixed WZ/ZB NWs were grown with approximately the same temperature as the pure ZB and pure WZ NWs. The Curie temperature of the samples, which was determined by magnetotransport measurements, was 20 K for the pure WZ NWs and the mixed WZ/ZB NWs. No ferromagnetic phase transition was observed for the as grown pure ZB NWs.

To summarize, we found a Mn concentration of at least 5% and a low As_4/Ga ratio of 1.5 is necessary for the growth of ferromagnetic GaAs/GaMnAs core shell NWs. To obtain a smooth and homogeneous GaMnAs shell, the growth temperature had to be reduced to 190°C. The Curie temperatures of 20 K for the pure WZ NWs and the mixed ZB/WZ NWs are below the Curie temperatures achieved for 2D GaMnAs layers. The ZB NWs did not show a ferromagnetic phase transition for the as grown samples in magnetotransport measurements. To find an explanation for the low Curie temperatures, the structural properties of the GaMnAs shell have to be examined.

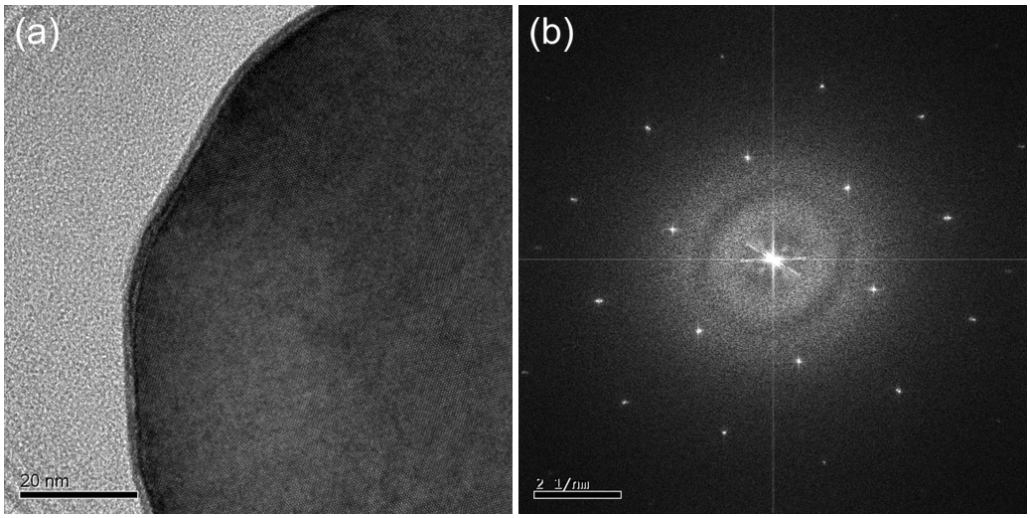

Figure 6.4: (a) High resolution cross sectional TEM image of a GaAs/GaMnAs core shell NW. (b) FFT of (a). The pattern indicates that the periodic arrangement of the crystal is not changed between the core NW and the GaMnAs shell. Taken from [97].

6.2.2 Structural properties of GaAs/GaMnAs core shell NWs

For the following investigation, core shell NWs with a mixed WZ/ZB crystal structure were used. First we examine if the GaMnAs shell is grown epitaxially on the GaAs core NW and how the GaAs core NW cross section influences the GaMnAs shell cross section. Therefore, TEM cross sectional samples were fabricated as described in [97]. We use the obtained results to explain the observed Mn segregation on the corners of the core NWs.

GaMnAs shell properties

A high resolution cross sectional TEM image of a GaAs/GaMnAs core shell NW and the corresponding fast Fourier transform (FFT) pattern are shown in figure 6.4. The GaAs core NW could not be distinguished from the GaMnAs shell in figure 6.4 (a) because no interface region is formed between the core and the shell. This indicates that the GaMnAs shell is grown epitaxially on the GaAs core NW. The FFT pattern of figure 6.4 (b) confirms this result because no additional peaks to the well known WZ/ZB [0001]/[111] diffractograms are observed, which would indicate a change in crystal structure between the GaAs core and the GaMnAs shell. We therefore conclude that the GaMnAs shell is grown epitaxially on the GaAs core NW.

Next, we investigate the dependence of the GaMnAs shell morphology on the morphology of the GaAs core NW. On our samples, hexagonal core NWs with $(10\bar{1}0)$

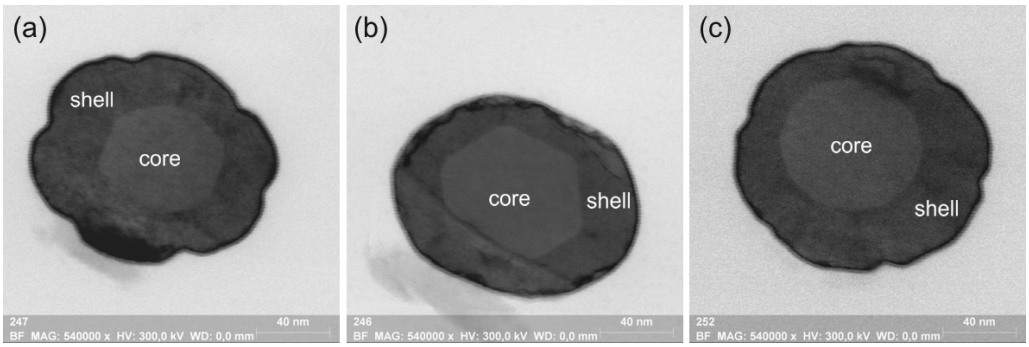

Figure 6.5: STEM images of GaAs/GaMnAs core shell NWs. The morphology of the GaMnAs shell depends on the morphology of GaAs core NW. (a) Core NW showing a hexagonal cross section with six $(10\bar{1}0)$ *side facets, (b) core NW showing a hexagonal cross section with six* $(11\bar{2}0)$ *side facets and (c) core NW showing a polygonal cross section with six* $(10\bar{1}0)$ *and six* $(11\bar{2}0)$ *side facets. Taken from [97].*

and $(11\bar{2}0)$ side facets and polygonal core NWs with $(10\bar{1}0) + (11\bar{2}0)$ side facets are observed. Figure 6.5 shows STEM images of the three different kinds of NWs.

In the STEM image, the GaMnAs shell appears darker as the GaAs core NW due to Mn interstitial defects in the GaMnAs shell [97]. The morphology of the GaMnAs shell strongly depends on the side facet orientation of the GaAs core NW. The GaMnAs shell cross section of GaAs core NWs with $(10\bar{1}0)$ sidewalls looks blossom like. In contrast, the GaMnAs shell cross section of GaAs core NWs with $(11\bar{2}0)$ sidewalls is round and the GaMnAs shell cross section of polygonal GaAs core NWs with $(10\bar{1}0) + (11\bar{2}0)$ sidewalls is a combination of both. This can be explained by taking into account different surface energies of the NW side facets and potential barriers at the corners of the side facets, which limit the diffusion of adatoms at low growth temperatures.

For GaAs core NWs with WZ crystal structure, the surface energies obey the inequality $\gamma_{10\bar{1}0} < \gamma_{11\bar{2}0}$ [96]. Due to the fact that only $(10\bar{1}0)$ and $(11\bar{2}0)$ side facets are formed during NW growth, we conclude that the $(10\bar{1}0)$ side facets represent the equilibrium shape of the NW cross section while the $(11\bar{2}0)$ side facets represent the energetically unfavorable sidewall configuration. The different surface energies are equivalent to different chemical potentials on the $(10\bar{1}0)$ and $(11\bar{2}0)$ sidewalls and as a consequence adatom diffusion takes place which is directed such that the size of the energetically unfavorable $(11\bar{2}0)$ side facets is decreasing while energetically more favorable $(10\bar{1}0)$ sidewalls are formed [111].

Due to the fact that small $(10\bar{1}0)$ side facets in the order of 5 nm are present at the corners of NWs with $(11\bar{2}0)$ sidewalls, the adatom diffusion should lead to a transformation of the NW cross section during shell growth and as a result exclusively

core shell NWs with an equilibrium shape, i.e. $(10\bar{1}0)$ sidewalls should appear [111]. The reason why this is not observed for our NW samples is attributed to potential barriers on the corners of the core NWs, which play a major roll at low growth temperatures [40,112]. The potential barriers reduce the diffusion length of adatoms and increase the nucleation rate at the corners of the side facets. As a consequence, the increased growth rate at the corners yields the formation of the blossom like cross section for core NWs with $(10\bar{1}0)$ oriented side facets. By taking into account the diffusion flux caused by the energetically unfavorable sidewall configuration, also the round cross section for core NWs with $(11\bar{2}0)$ oriented side facets could be explained. Due to the fact that polygonal NWs show both types of side facets, the observed shell cross section can be attributed to a superposition of the effects responsible for the GaMnAs shell morphology on $(10\bar{1}0)$ and $(11\bar{2}0)$ side facets.

Mn segregation

Now we investigate the influence of the potential barriers on the Mn distribution in the GaMnAs shell. Therefore, several TEM bright field cross sectional images of GaAs/GaMnAs core shell NWs were examined. The cross sectional images of GaAs core NWs with $(11\bar{2}0)$ oriented side walls exhibit dark strips, which start from the corners of the core NW and extend radially into the GaMnAs shell. Figure 6.6 (a) shows a TEM bright field cross sectional image of a core shell NW with $(11\bar{2}0)$ side facets. The dark strips in the GaMnAs shell are indicated by black arrows. To investigate the origin of the dark strips, EDX point measurements were performed. The regions of the point measurements are indicated by red and blue dots in figure 6.6 (b). For a detailed description of the measurements see [97].
The results of the EDX point measurements are summarized in figure 6.6 (c). It should be noted that no absolute numbers for the Mn concentration can be given because the TEM specific Cliff-Lorimer factors are not known. Therefore, the Mn/As peak ratio of the dark strips and the region between the dark strips is used to compare the Mn contents of different shell regions. As can be seen in the inset of figure 6.6 (c), the Mn content is increased in the strips with respect to the region between the strips. The origin of the increased Mn concentration is attributed to the potential barriers at the corners of the NW sidewalls, which strongly reduce the Mn diffusion length. To determine whether the additional Mn is incorporated as substitutional Mn on Ga sites or as Mn interstitial defects, the Ga peak ratio of the dark strips and the region between the dark strips is compared. If the Mn is incorporated as substitutional Mn on Ga sites, then the amplitude of the Ga peak in the dark strips has to be reduced. However, this was not observed. Therefore we conclude that the additional Mn in the black strips is incorporated as Mn interstitial defects. The

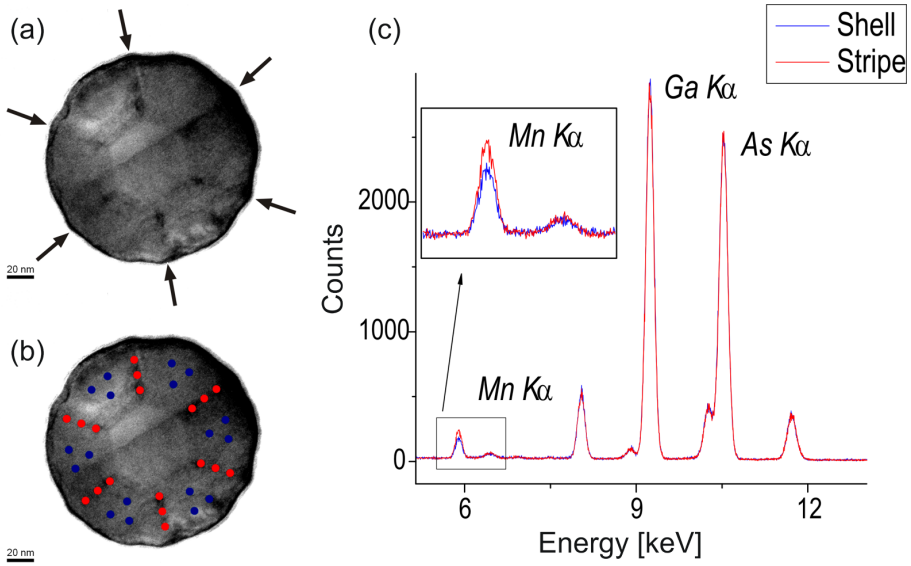

Figure 6.6: (a) TEM bright field cross sectional image of a core shell NW. The side facets of the core NW are oriented in the $(11\bar{2}0)$ *direction. Dark strips are visible in the GaMnAs shell which are oriented along the corners of the core NW. (b) The same TEM bright field image, the red and blue dots indicate the regions in which the EDX point measurements are performed. (c) The results of the EDX point measurements for the dark strips and the region between the dark strips. Taken from [97].*

low Curie temperature of the GaAs/GaMnAs core shell NWs with a mixed WZ/ZB crystal structure compared to 2D GaMnAs layers can at least partially be attributed to the high number of Mn interstitial defects.

To summarize, we found that the GaMnAs shell is grown epitaxially on the GaAs core NW. As a consequence, the crystal structure of the GaAs core NW is adopted by the GaMnAs shell. However, the cross section of the GaAs core NW is not adapted by the GaMnAs shell. While GaAs core NWs exhibit a hexagonal cross section with $(10\bar{1}0)$ or $(11\bar{2}0)$ side facets or a polygonal cross section with $(10\bar{1}0) + (11\bar{2}0)$ side facets, the GaMnAs shell forms a more complex structure. In case of $(10\bar{1}0)$ sidewalls, the GaMnAs shell cross section looks blossom like while for $(11\bar{2}0)$ sidewalls the GaMnAs shell cross section is nearly round. For the polygonal core NWs with $(10\bar{1}0) + (11\bar{2}0)$ side facets the GaMnAs shell cross section is a superposition of the $(10\bar{1}0)$ and $(11\bar{2}0)$ sidewall cross sections. This observation could be explained by the different surface energies of the side facets and potential barriers at the corners of the GaAs core NWs. The potential barriers also influence the diffusion of Mn and as a consequence an increased Mn content is found in dark strips, which start at the corners of the GaAs core NW and extend radially into the GaMnAs shell. TEM EDX measurements reveal that the additional Mn is incorporated into the

crystal as Mn interstitial defects. The Mn interstitial defects act as double donors and reduce the hole density in the GaMnAs shell. The reduced Curie temperature of GaAs/GaMnAs core shell NWs with respect to the 2D GaMnAs layers is at least partially attributed to the Mn interstitial defects. However, also an influence of the predominant WZ crystal structure on the Curie temperature seems to be possible. Whether the special growth conditions on the GaAs core NW side walls also influence the magnetic properties, e.g. the magnetic anisotropies of the GaAs/GaMnAs core shell NWs, will be investigated in the next section.

6.2.3 Magnetic properties of GaAs/GaMnAs core shell NWs

The magnetic properties of the GaAs/GaMnAs core shell NW samples were investigated using a quantum interference device (SQUID) [88] and magnetotransport measurements [8]. For the SQUID characterization all NW samples were measured as grown. For magnetotransport measurements the NWs were transferred from the GaAs substrate to a Si substrate and contacted by e-beam lithography as described in [8]. The samples were measured in a cryostat which is equipped with a superconducting coil enabling measurements at temperatures down to 1.4 K and in magnetic fields up to 10 T [8]. The sample was mounted on a rotatable sample holder, permitting to vary the angle between the applied magnetic field and the NW axis.

SQUID measurements

As the NWs grow preferentially along the [111] direction the magnetic field can be oriented with respect to the NW axis. Due to the high density of NWs and an average length of 3.5 μm, the planar growth of GaMnAs on the substrate is almost completely suppressed. For an idealized NW sample with a uniform NW diameter of 70 nm, a NW length of 3.5 μm and a NW density of 10 NW/μm^2, the total surface area of the NWs would be by a factor of 7.7 larger than the bare substrate surface. Assuming that the deposited GaMnAs is distributed equally over the total area, this would result in a shell thickness of 34 nm and 23 nm for a nominal 2D layer thickness of 300 nm and 200 nm, respectively. In reality, due to the reduced diffusion of adatoms, the amount of GaMnAs material deposited at the tip of the NWs will be even higher and, as a consequence, the planar growth even more inhibited. This is consistent with SEM characterizations of core shell NWs where the obtained base shell thickness of < 20 nm was considerably thinner than the calculated value of 34 nm. Therefore the magnetization values obtained by SQUID characterize mainly the magnetic shell of the NWs with the contribution of the planar grown GaMnAs in between the NWs being at most 10% of the signal.

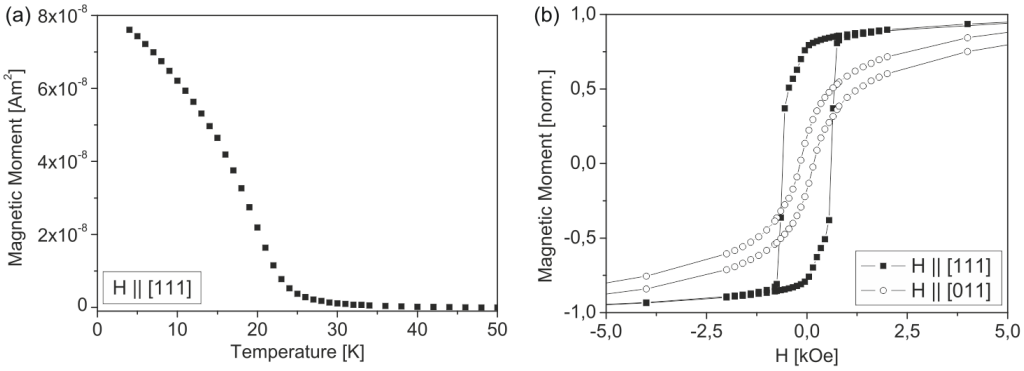

Figure 6.7: (a) Temperature dependence of the magnetization of a core shell NW sample grown at 209° C with a nominal GaMnAs 2D thickness of 300 nm giving a Curie temperature of 20 K. (b) Hysteresis loops at 6 K of the same NW sample. Taken from [8].

The Curie temperature was determined by measuring the temperature dependence of the magnetization with a magnetic field of 25 mT (250 Oe) applied parallel to the NW axis along the [111] direction. NW samples with a nominal 2D GaMnAs layer thickness of 200 nm or 300 nm grown at substrate temperatures between 205°C and 247°C were analyzed. All NW samples show T_C values in the range of 12 K and 20 K. The highest T_C of 20 K is achieved for growth temperatures of 205°C and 209°C (samples C081204B and C081212A) for a nominal 2D GaMnAs layer thickness of 200 nm or 300 nm, respectively, as shown in figure 6.7 (a). The thickness of the GaMnAs shell does not have a measurable effect on T_C. Increasing the growth temperature (215°C or 220°C) leads to lower T_C values of 17 K or 16 K. At 220°C substrate temperature, where the transition from a rough GaMnAs shell growth to branched NW growth was observed, T_C is reduced to 12 K, indicating a reduced quality of the GaMnAs shell.

In figure 6.7 (b) magnetization hysteresis loops of a NW sample with a GaMnAs shell of a nominal 2D layer thickness of 300 nm grown at 209°C are shown. The magnetic field was applied either parallel to the NW axis along the [111] direction or perpendicular to the NW axis in the $[01\bar{1}]$ direction. There is a clear difference between the two field orientations. In the perpendicular case the NWs show a magnetic hard axis behavior with 20% remanence and only little hysteresis. In the parallel field orientation the remanence is 80% and a coercive field of 55 mT (550 Oe) is observed. For the parallel field orientation various NW samples with two different 2D GaMnAs nominal layer thicknesses grown at different substrate temperatures are compared. All NW samples exhibit the same characteristics. The remanence is between 80% and 65%. The coercive fields range from 50 mT to

75 mT (500 Oe to 750 Oe) with the NW samples with higher Curie temperatures having a larger coercive field. The magnetization hysteresis loops show that the [111] direction parallel to the NW axis is a magnetic easy axis. For the branched NW sample we observe, as expected, a less pronounced magnetic anisotropy. For a full understanding of the hysteresis loops, one also has to take into account the magnetic signal arising from the (not totally suppressed) planar growth inbetween the NWs and from the polycrystalline GaMnAs growth at the tip of the NWs. Furthermore, there is a finite number of kinked NWs. We want to note that the sample cannot be mounted in the SQUID without NWs at the edge of the sample breaking off. Third, due to the non-uniform shell thickness the anisotropy constants are likely to vary along the NW axis. All three points explain to some extent the observed deviation from the squared loop characteristics of an ideal magnetic easy axis.
As shown for lithographically fabricated GaMnAs strips of similar width, the shape anisotropy term does not play a significant role as the saturation magnetization is small [5, 48]. To explain the observed anisotropy, two basic scenarios are considered. Either a uniform magnetization forms with a well-defined magnetic anisotropy or the different side facets develop separate magnetic domains which add up to a net magnetization. In the second scenario one would expect a net magnetization pointing along the NW axis as radial components of opposite side facets cancel each other. This is valid, when the magnetic easy axis of the side facets does not point perpendicularly to the NW axis, which can be excluded from our measurements. For the uniform magnetization, although no simulation of strain induced anisotropy of (110) GaMnAs strips exist, we expect the reason for the observed easy axis along the NW axis to be the same as in the case of lithographically defined strips, namely, anisotropic strain relaxation [48, 115].

Magnetotransport measurements

The magnetotransport measurements were performed by Christian Butschkow. The SQUID results, which were obtained on an ensemble of GaAs/GaMnAs core shell NWs (sample size: ∼4x4 mm^2, NW density: ∼10 NW/μm^2, total number of NWs: $\sim 1.6 \times 10^8$) will now be compared with magnetotransport measurements which are obtained from a single NW. The Curie temperature of a single NW was extracted from the resistance R(T) as described in chapter 6.1.1. We determined the Curie temperature of five NWs to be between 17 K and 19 K, in good agreement with the results of the SQUID measurements.
For a magnetic field applied parallel to the NW axis and sweeping the field up, R displays a large resistance jump once the magnetization has changed direction (cf. figure 6.8 (a)). In contrast, sweeps with a perpendicular magnetic field orientation

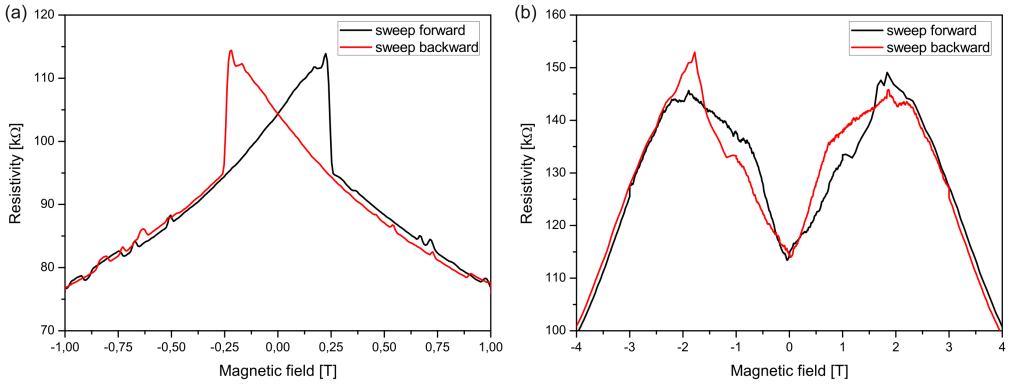

Figure 6.8: (a) Magnetotransport data at T=4 K for H parallel to the nanowire axis (0°). The black and red lines refer to opposite sweep directions. (b) Magnetic field sweep perpendicular to the nanowire axis (90°) at T=4 K. Taken from [8].

exhibit a continuous change of the low field resistance (cf. figure 6.8 (b)). This is consistent with previous studies on NW ensembles by SQUID, indicating a uniaxial magnetic anisotropy with the easy axis pointing along the NW axis. The resistance jumps can then be ascribed to an abrupt magnetization reversal due to thermally activated domain wall nucleation and propagation, characteristic for magnetization reversal along a magnetic easy axis. The continuous resistance change for the perpendicular configuration reflects a coherent rotation of the magnetization, characteristic for a magnetic hard axis. The nearly linear slope of R(H) in figure 6.8 (b) suggests that the negative magnetoresistance effect (NMR) exhibits an approximately linear dependence on the applied magnetic field in this configuration for fields below 1 T.

We now show that the dominating features observed in the magnetoresistance traces of figure 6.8 can be described by the dependence of the NMR on the effective magnetic field $\vec{H}_{eff}$. In our case, only a uniaxial anisotropy term with an anisotropy constant K_U and the Zeeman energy term need to be considered for the free energy:

$$E(\theta_M, \varphi_M) = K_U \sin^2(\theta_M) \sin^2(\varphi_M) + \mu_0 M_S H \sin(\theta_M) \cos(\varphi_M - \varphi_H) \qquad (6.1)$$

θ_M and φ_M specify the azimuthal and polar angles of the magnetization with respect to the magnetic easy axis, while φ_H is the direction of the external magnetic field and M_S the saturation magnetization. When the static magnetization is oriented in the plane of the substrate ($\theta_M = 90°$) equation 6.1 leads to the expression for the effective field:

$$H_{eff} = \frac{1}{\mu_0 M_S \sin(\theta_M)} \sqrt{E_{\theta_M\theta_M} E_{\varphi_M\varphi_M} - E^2_{\theta_M\varphi_M}} \tag{6.2}$$

$$\overset{\theta_M=90^\circ}{\approx} H_0 \cos(\varphi_M - \varphi_H) + \frac{2K_U}{\mu_0 M_S} \cos(2\varphi_M) \tag{6.3}$$

where $E_{\theta_M\theta_M}$, $E_{\varphi_M\varphi_M}$ and $E_{\theta_M\varphi_M}$ are the second derivatives of the free energy landscape. The effective field consists of two terms, the first term is related to the applied external magnetic field and the second term to the anisotropy field $H_a = \frac{2K_U}{\mu_0 M_S}$.
Next we analyze the data of figure 6.8 under the assumption that the NMR changes linearly with the effective field. The magnetoresistance measured along the NW axis (cf. figure 6.8 (a)) shows a nearly linear increase from -1 T to 0 T and continues to increase beyond $\mu_0 H = 0$ T, until a resistance jump occurs at the coercive field H_C. The values of $\mu_0 H_C$ obtained for different NWs at 4 K range between 140 mT and 220 mT, in good agreement with the SQUID data of NW ensembles. Prior to the magnetization reversal, the magnetization and the applied magnetic field are pointing into opposite directions ($\varphi_M = 180^\circ$, $\varphi_H = 0^\circ$). According to equation 6.3 this leads for $H_0 = H_C$ to $H_{eff,1} = -H_C + \frac{2K_U}{\mu_0 M_S}$. After the jump, the magnetization aligns with the external field ($\varphi_M = 0^\circ$, $\varphi_H = 0^\circ$) and we obtain $H_{eff,2} = H_C + \frac{2K_U}{\mu_0 M_S}$. Thus, the resistance jump due to NMR reflects the absolute difference of the effective magnetic field values of $\Delta H_{eff} = 2H_C$. The corresponding backsweep (red curve) provides, due to ferromagnetic hysteresis, qualitatively the same measurement but mirrored at $\mu_0 H_0 = 0$ T.
In contrast, the magnetoresistance for $\vec{H}$ applied perpendicular to the NW axis (cf. 6.8 b,) changes almost continuously and exhibits only little hysteresis. Assuming a continuous rotation of the magnetization, the situation is also well described by equation 6.3. The two local maxima at ± 1.8 T in figure 6.8 (b) mark approximately the anisotropy field H_a where the magnetization saturates ($\varphi_M = 90^\circ$, $\varphi_H = 90^\circ$). Here, the externally applied field equals the anisotropy field, and the effective magnetic field vanishes.
For direct comparison of the magnetoresistance for the parallel and perpendicular field configuration, the curves have to be displayed as a function of the effective magnetic field. For $\varphi_H = 0^\circ$ and $H_0 > H_C$, $H_{eff} = H_0 + H_a$ holds while for $\varphi_H = 90^\circ$ and $H_0 > H_a$ the effective magnetic field is $H_{eff} = H_0 - H_a$. By shifting both curves by $\mu_0 H_a$ along the x-axis to the right and to the left, respectively (figure 6.9, gray and orange line), the two data sets can be compared directly on the effective magnetic field scale for $H_{eff} > H_a + H_C$ (figure 6.9 inset). While on the $\mu_0 H_0$ scale the magnetic field dependence of the resistance for parallel and perpendicularly applied fields appear to be rather different, they are nearly the same

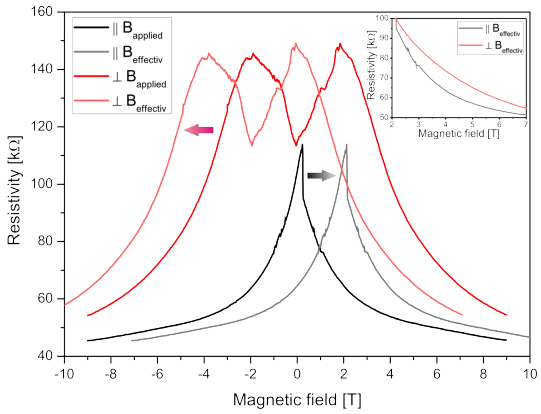

Figure 6.9: Transformation from the $\mu_0 H_0$ scale to the $\mu_0 H_{eff}$ scale by shifting R(90°) and R(0°) by $\pm\mu_0 H_a$. The resulting high field magnetoresistance at 4 K as a function of the effective magnetic field is shown in the inset. This makes the two curves directly comparable for values of the effective field of $\mu_0 H_{eff} > 2.2$ T. Taken from [8].

on the $\mu_0 H_{eff}$ scale, thus emphasizing the dominating role of the effective magnetic field for magnetotransport. The remaining difference is of the order of 3% to 10% and stems most likely from the anisotropic magnetoresistance (AMR) effect. The AMR effect usually does not show any field dependence. However, the resistance difference R(90°) - R(0°) in the inset of figure 6.9 is not constant, suggesting that additional effects influence the magnetoresistance. For example weak localization [64] or, due to the inhomogeneity of the NW, spatially altering magnetic properties could contribute to the measurements.

6.2.4 Conclusion

We found that, in contrast to 2D GaMnAs layer growth, the GaMnAs shell has to be grown at a low As_4/Ga ratio of at most 1.5 with a minimum Mn content of 5% to obtain ferromagnetic GaAs/GaMnAs core shell NWs. As a consequence of the low As_4/Ga ratio also the growth temperature has to be very low. A smooth GaMnAs shell was obtained for growth temperatures between 190°C and 210°C. At higher growth temperatures the formation of clusters on the NW side facets was observed. TEM high resolution bright field cross sectional images reveal that the GaMnAs shell is grown epitaxially on the GaAs core NW because no interface region was observed in the TEM images. From STEM images we deduce that the GaMnAs shell morphology strongly depends on the side facet orientation of the GaAs core NW. For hexagonal GaAs core NWs with $(10\bar{1}0)$ side facets the GaMnAs shell cross

section looks blossom like while for hexagonal GaAs core NWs with $(11\bar{2}0)$ side facets the GaMnAs shell cross section is round. For polygonal GaAs core NWs with $(10\bar{1}0) + (11\bar{2}0)$ side facets the GaMnAs shell cross section is a superposition of both hexagonal cross sections. This could be explained by taking into account the different surface energies of the side facets [96] and potential barriers at the corners of the side facets, which play a major role at low growth temperatures [40, 112]. The potential barriers are also responsible for Mn segregation which was observed for GaAs core NWs with $(11\bar{2}0)$ oriented side facets. The Mn segregation, which starts at the corners of the GaAs core NW and extends radially into the GaMnAs shell leads to a locally increased Mn concentration, indicated by dark strips in TEM bright field images. EDX point measurements reveal that the additional amount of Mn is incorporated as Mn interstitial defects.

The observation that ferromagnetic GaMnAs shells could only be fabricated with special growth parameters (low As_4/Ga ratio of 1.5 and a minimum Mn content of at least 5%) is attributed to the high amount of Mn interstitial defects. Due to the fact that the amount of holes, which is essential for the formation of the ferromagnetic phase in GaMnAs is reduced by the Mn interstitial defects, an additional decrease in hole density, e.g. from As antisites, which originate from a high As_4/Ga ratio, or a too low hole density, which originates from a low Mn concentration, would result in a total suppression of the ferromagnetic phase transition. The Curie temperature of the GaAs/GaMnAs core shell NWs, which is 20 K for pure WZ NWs and mixed WZ/ZB NWs, is lower then the Curie temperature of a comparable GaMnAs layer due to the low hole concentration. An influence of the crystal structure on T_C is also possible.

Using SQUID and magnetotransport measurements, the magnetic properties of the GaAs/GaMnAs core shell NWs are investigated. Both methods reveal a magnetic easy axis along the NW axis and a magnetic hard axis perpendicular to the NW axis. The remanence for the magnetic easy axis was between 80% and 65% and the coercive fields was in the range from 50 mT to 75 mT (500 Oe to 750 Oe) for SQUID ensemble measurements (at 6 K) and from 140 mT to 220 mT for magnetotransport single NW measurements (at 4 K). The shape of the magnetotransport curves can be explained by introducing an effective magnetic field, which consists of the external magnetic field and an anisotropy field. Due to the fact that the observed magnetic anisotropies are also found in thin GaMnAs strips [48,115], the origin of the magnetic anisotropy of GaAs/GaMnAs core shell NWs is attributed to strain relaxation of the GaMnAs shell perpendicular to the NW axis.

6.3 Post growth annealing

The annealing experiments were performed by Alexander Eckrot [27] under the supervision of Christian Butschkow. For the investigation of the NW resistivity with respect to the annealing temperature, core shell NWs (sample C081204B) with a mixed WZ/ZB crystal structure, a Mn content of 5%, a shell thickness of approximately 30 nm and a GaMnAs growth temperature of 205°C were used. To examine the Curie temperature of pure ZB (sample C120308A) and pure WZ (sample C120111B) core shell NWs after annealing, samples with a Mn content of 5%, a shell thickness of approximately 30 nm and a GaMnAs growth temperature of 190°C were used. The Curie temperature of mixed WZ/ZB core shell NWs after annealing was investigated on the same sample, which was already used for the magnetic anisotropy investigations (sample C081204B). The results of the GaAs/GaMnAs NWs annealing experiments are compared with results obtained from 2D GaMnAs layers, which were annealed in the same oven. The annealing setup consists of the NW annealing oven and the measurement hardware as described in chapter 3.4. The T_C measurements were carried out in a cryostat of Prof. Weiss.

First, a suitable annealing temperature and annealing time had to be found. Therefore, the NWs were annealed at temperatures between 152°C and 277°C for at least 20 hours. In figure 6.10 (a) the normalized GaMnAs shell resistivity is plotted as a function of the annealing time for annealing temperatures of 152°C, 182°C, 203°C, 206°C, 229°C and 277°C. Due to the fact that the Curie temperature depends on the carrier concentration of the GaMnAs layer [113], the decrease in sample resistivity usually is accompanied by an increase in T_C. As shown in figure 6.10 (a), the sample resistivity for high annealing temperatures drops faster than for low annealing temperatures. For long annealing times and high annealing temperatures the resistivity approaches a finite value. We conclude that for high annealing temperatures above 229°C a saturation of the resistivity is observed after approximately 24 hours. For lower annealing temperatures the saturation of the resistivity is expected to occur after longer annealing times.

In the next step, the Curie temperatures of the core shell NWs with pure ZB, a mixed WZ/ZB and pure WZ crystal structure were investigated. The pure ZB and the pure WZ core shell NWs were annealed at 185°C for 72 hours while the mixed ZB/WZ core shell NWs were annealed at 227°C for 280 hours. A saturation of the sample resistivity was observed for all three samples. The observed increase in T_C was approximately 3 K for the mixed WZ/ZB core shell NWs (from 20 K to 23 K) and 10 K for the pure WZ core shell NWs (from 20 K to 30 K). No ferromagnetic phase transition was observed for pure ZB core shell NWs as grown. However, after

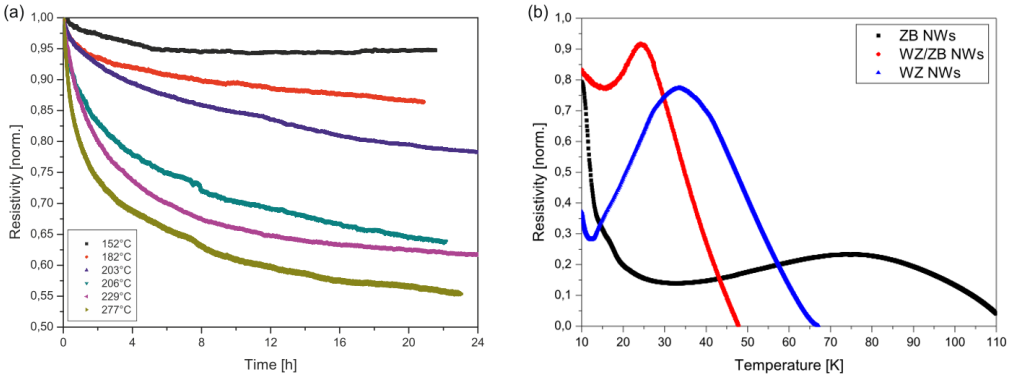

Figure 6.10: (a) Sample resistivity (sample C081204B) versus the annealing time for different annealing temperatures. The decrease in sample resistivity is more pronounced for higher annealing temperatures. (b) Cooling curves of pure ZB (sample C120308A), mixed WZ/ZB (sample C081204B) and pure WZ (sample C120111B) core shell NWs. Data provided by A. Eckrot.

annealing the Curie temperature was approximately 60 K, a value which is close to annealed 2D GaMnAs layers on (110) oriented GaAs substrates [118]. We want to note that the values for the Curie temperature are not very precise because the first derivative of the cooling curve showed no pronounced singularity. The small increase in T_C for mixed WZ/ZB and pure WZ core shell NWs can be attributed to the crystal properties of these NWs. The mixed WZ/ZB core shell NWs are characterized by a changing crystal structure while the pure WZ NWs show a high number of stacking faults (cf. chapter 4.2.4). The crystal mixing zones and the crystal defects may impede the Mn segregation during the annealing procedure and thereby reduce the increase in T_C. Compared to the mixed WZ/ZB and pure WZ core shell NWs, the crystal structure of pure ZB NWs shows only a few stacking faults in the largest part of the NW (cf. chapter 4.2.5). As a consequence, a Curie temperature comparable to 2D GaMnAs layers grown on (110) oriented GaAs substrates can be observed after annealing. However, also an influence of the crystal structure on T_C is possible. Next, annealing experiments with GaMnAs layers grown on (110) oriented GaAs substrate were carried out.

For the GaMnAs layer annealing experiment, a GaMnAs sample (C110623B) grown on (110) oriented GaAs substrate at a growth temperature of 260°C with a Mn content of 4.9% and a layer thickness of 30 nm was investigated. The cooling curve obtained in the cryostat revealed a T_C of 43 K as grown. This is in agreement with the Curie temperature estimated in the dewar based measurement setup described in chapter 3.5.2, which was 50 K. Here, the measured Curie temperature is only precise to approximately 10% because the singularity in the first derivative of the cooling curve could again not exactly be determined.

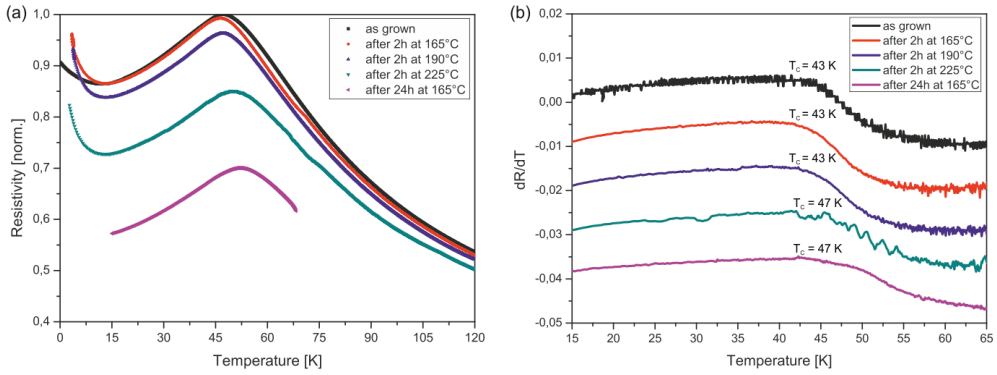

Figure 6.11: (a) Cooling curves of a GaMnAs layer, which was annealed at 165° C, 190° C, and 225° C for 2 hours and at 190° C for 24 hours. (b) First derivatives of the cooling curves with the corresponding Curie temperatures. Data provided by A. Eckrot.

In figure 6.11 (a) the cooling curves for three different annealing temperatures are shown. The sample was annealed at 165°C, 190°C and 225°C for 2 hours, respectively. Afterwards, an additional annealing step at 190°C for 24 hours was applied. As can be seen from the first derivative of the cooling curve in figure 6.11 (b), the Curie temperature is not significantly changed for annealing temperatures of 165°C and 190°C. For an annealing temperature of 225°C, the Curie temperature increases from 43 K to 47 K. The additional annealing step at 165°C for 24 hours reduces the sample resistivity but has no influence on the Curie temperature. As in the case of the mixed WZ/ZB and the pure WZ core shell NWs, the increase in T_C after annealing for GaMnAs layers grown on (110) oriented GaAs substrates is very small. An influence of the annealing setup on the increase in T_C can therefore not be excluded. However, it seems more likely that the origin of the small increase in T_C for the investigated GaMnAs layer is caused by the high amount of As antisites, which result from the high As_4/Ga ratio of 20. Due to the high amount of As antisites (donors), the reduction of Mn interstitials (donors) induced by annealing is negligible and as a consequence the increase in T_C is small.

Chapter 7

Conclusion

In the first part of this thesis, the influence of different growth parameters on the NW morphology and the NW crystal structure was investigated. To explain our observations, a theory was developed which relates the Ga content of the catalyst droplet during growth to the crystal structure of a single NW [98]. Applying this theory to the sample preparation procedure and to the NW growth parameters enables the fabrication of GaAs NWs with pure WZ and pure ZB crystal phase.
In the second part of this thesis, NW growth on GaAs and Si substrates covered by a thin SiO_2 layer was investigated. The SiO_2 layer was pre-structured with holes, which provide defined nucleation sites for the Ga catalyst droplets. The equal distance between the holes ensures that the material from the effusion cells is equally distributed under all NWs. As a consequence, the Ga content in the catalyst droplets and thereby the NW crystal structure is the same for all NWs on one sample. By evaluating the NWs of different hole grids, a dependence of the NW morphology and the hole occupation number on the hole pitch was observed [4]. To explain our observations the current growth theory for NW growth on SiO_2 covered substrates was extended, now including As diffusion on the SiO_2 layer and the NW sidewalls.
In the third part of this thesis, the magnetic properties of GaAs/GaMnAs core shell NWs were investigated. First, the growth of GaMnAs on (110) oriented GaAs substrates, which is the predominant orientation of the NW side facets, was optimized. The growth parameters had to be adjusted for the GaMnAs shell growth. The obtained GaAs/GaMnAs core shell NWs, which were grown with pure WZ, a mixed WZ/ZB and pure ZB crystal phase were investigated by TEM, SQUID and magnetotransport measurements. Due to their special geometry, the GaAs/GaMnAs NWs reveal unique magnetic properties like a strong uniaxial magnetic anisotropy [8, 88] and a crystal structure dependent Curie temperature.

Before 2008, the systematic investigation of the NW morphology with respect to the applied growth parameters for GaAs NWs grown by MBE includes the change in growth temperature from 320°C to 620°C in 50°C intervals [104] and the change in As_4/Ga ratio from 1.5 to 2.3 [83] as well as the change in deposited material from 500 nm to 1000 nm [16]. The quantity which was mainly investigated was the dependence of the NW length on the NW diameter [16, 83]. Due to the fact that these investigations were not very detailed, as most of them contain only two values for every investigated parameter and in addition are not absolutely applicable to our MBE system, as a gas source MBE was used for some of the experiments [83], a detailed study of the sample preparation procedure and the growth parameters was conducted. The analysis includes the variation of the Au layer thickness, the substrate preparation and oxide desorption procedure as well as the variation of different growth parameters like the growth temperature, the total As_4 and Ga fluxes, the As_4/Ga ratio and the As_2/Ga ratio. Here, we just want to highlight some of the observations which were made during the morphology investigations.

The Au layer thickness does not systematically influence the NW density. Instead of more catalyst droplets, bigger catalyst droplets with a higher Au/Ga ratio are formed for increasing Au layer thicknesses. This leads to the formation of predominantly thick and short NWs with pure WZ crystal structure. The maximum growth temperature was found to be 580°C and the best growth temperature with respect to a homogeneous NW length at an acceptable NW growth rate was 540°C. The investigation of the As_4 and Ga total fluxes revealed that an increase in total flux results in an approximately proportional increase in NW length. From experiments regarding the As_4/Ga ratio we know that the increase in NW length is dedicated to an increase in As_4 pressure. The Au catalyzed growth of GaAs NWs is therefore regarded as As determined. The observed behavior can be explained by the faster nucleation at the NW-droplet boundary with increasing As_4 pressure, which causes a reduction of the droplet supersaturation and thereby increases the Ga diffusion to the catalyst droplet. This is accompanied by a decreased nucleation on the substrate. The As_4/Ga ratio experiments also reveal that for a very low As_4/Ga ratio of 0.7, NW with a very homogeneous size distribution, cross section and a big Ga catalyst droplet are observed. These NWs show pure ZB crystal structure.

The observation that pure WZ and ZB NWs can be grown with the Au catalyzed growth technique initialized a detailed investigation of the correlation between the Ga content in the catalyzed droplet and the NW crystal structure [98]. For a Ga concentration between 25% and 50% during growth, Au catalyzed NW growth is observed which results in the formation of NWs with pure WZ crystal structure. At a Ga concentration higher than 60% during growth, a new growth mode is observed

which we refer to as pseudo Ga assisted. The enhanced probability to form ZB segments in the pseudo Ga assisted growth mode is attributed to the reduced droplet surface energy of the catalyst droplet resulting in nucleation at the center of the NW-droplet boundary. Using these results, NWs with a distinct crystal phase were fabricated. For NWs with pure ZB crystal structure a substrate with a very thin Au layer of 0.5 Å and a high Ga flux of one monolayer per second at a small As_4/Ga ratio of 1.3 was used to achieve a Ga concentration of at least 60% in the droplet during growth. For NWs with pure WZ crystal structure a substrate with a thick Au layer of 10 Å and a small Ga flux of 0.4 Å/s at a high As_4/Ga ratio of 8.8 was used to keep the Ga concentration in the catalyst droplet below 50% during growth. TEM investigations confirmed the formation of NWs with pure WZ and ZB crystal phase.

To ensure that the Ga concentration of all catalyst droplets and thereby the crystal structure of all NWs is the same on one sample, the incoming Ga from the effusion cell has to be distributed equally under all catalyst droplets. Therefore, the samples were pre-structured to achieve an equal distance between the catalyst droplets. First, Au discs were fabricated on bare GaAs substrate at equal distances. The obtained results were not satisfying because the Au/Ga droplets migrate on the GaAs substrate. To prevent the surface migration, the Au discs were fabricated in predefined holes of a SiO_2 layer. However, also these results were not satisfying due to a massive GaAs cluster formation on the SiO_2 layer which changes the surface properties of the SiO_2 layer and thereby the Ga supply of the catalyst droplets. To overcome these problems, the Ga catalyzed growth technique [49] was applied which allows NW growth in a temperature regime where the cluster formation on the SiO_2 layer is suppressed [44]. For the Ga catalyzed growth technique, holes, which provide defined nucleation sites for the Ga catalyst droplets are fabricated in a grid like pattern with different hole pitches on the SiO_2 layer by e-beam lithography and wet chemical etching.

The most interesting result achieved on pre-structured SiO_2 is the dependence of the NW length, the NW tapering and distribution of the hole occupation number on the hole pitch at a fixed As_4/Ga ratio and the shift of the maximum in the hole occupation number for increasing As_4/Ga ratios. The NW length decreases while the NW tapering increases for increasing hole pitches. The distribution of the hole occupation number with respect to the hole pitches shows a Gaussian shape for a fixed As_4/Ga ratio and the maximum of the hole occupation number shifts to larger hole pitches for increasing As_4/Ga ratios. This results can only be explained if the commonly accepted growth model, which assumes Ga diffusion on the SiO_2 layer and on the NW sidewalls but no As diffusion is modified and As diffusion is taken

into account. The As diffusion length has to be in the order of some ten nm, much smaller than the Ga diffusion length, which is a few hundred nm in this temperature regime [60]. Due to the small As diffusion length, every NW has its own As reservoir independent of the hole pitch. In contrast, the NWs share their Ga reservoirs with vicinal NWs for small hole pitches. For increasing hole pitches the overlap of the Ga reservoirs is decreasing and for large hole pitches every NW has its own Ga reservoir. As a consequence of the different diffusion lengths of Ga and As, the effective As_4/Ga ratio is high for small hole pitches, decreases for larger hole pitches and finally becomes constant, if every NW has its own Ga reservoir. The decrease in NW length with increasing hole pitch can now be attributed to the decreasing effective As_4/Ga ratio, because Ga catalyzed NW growth is also As determined [10]. The increase in NW tapering with increasing hole pitch is attributed to the more Ga rich growth conditions at larger hole pitches where the excess Ga leads to an increase of the Ga catalyst droplet during growth. The Gaussian shape of the hole occupation number at a fixed As_4/Ga ratio is attributed to the fact that the growth conditions for GaAs NW growth are too As rich for small hole pitches, reach their optimal value for medium hole pitches and become too Ga rich for large hole pitches. Due to the fact that the optimum growth conditions shift toward larger hole pitches with increasing As_4/Ga ratios, also the maximum of the hole occupation number is shifted to larger hole pitches.

In the third part of this thesis the growth parameters for crystal structure tuning were used to fabricate GaAs/GaMnAs core shell NWs with a distinct crystal phase. As a first step, the growth of GaMnAs on (110) oriented GaAs substrate was optimized. The (110) crystal orientation in ZB, which is equivalent to the $(11\bar{2}0)$ crystal orientation in WZ, is the predominant crystal orientation of the NW side facets. A Curie temperature of 50 K was achieved in a very narrow growth window for a Mn concentration between 2% and 5%, a growth temperatures between 300°C and 260°C and an As_4/Ga ratio of 20. Due to the fact that pure WZ NWs could not be grown with the Ga catalyzed growth technique [100], the Au catalyzed growth technique was used for the fabrication of the GaAs core NWs. For the growth of the GaMnAs shell, the growth parameters have to be adjusted to meet the special growth conditions on the NW side facets. HRTEM images reveal that the GaMnAs shell grows epitaxially on the GaAs core NW. As shown by STEM cross sectional images, the shape of the GaMnAs shell depends strongly on the side facet orientation of the GaAs core NW. The GaMnAs shell cross section of GaAs core NWs with $(10\bar{1}0)$ sidewalls looks blossom like. In contrast, the GaMnAs shell cross section of GaAs core NWs with $(11\bar{2}0)$ sidewalls is round and the GaMnAs shell cross section of polygonal GaAs core NWs with $(10\bar{1}0) + (11\bar{2}0)$ sidewalls is a superposition of the

two hexagonal cross sections. The observed shape can be explained by the different surface energies of the NW side facets, which favours the formation of the low energy $(10\bar{1}0)$ sidewalls over the high energy $(11\bar{2}0)$ sidewalls and potential barriers on the corners of the NW side facets, which reduce the diffusion length of impinging adatoms. As a consequence of the potential barriers, also Mn segregation in the GaMnAs shell is observed for GaAs core NWs with $(11\bar{2}0)$ oriented side facets. In TEM bright field images, the Mn segregation becomes visible as dark strips, which start at the corners of the GaAs core NW and extend radially into the GaMnAs shell. EDX point measurements reveal that the amount of Mn in the dark strips is increased with respect to the regions between the dark strips. However, the additional Mn is not incorporated as substitutional Mn on Ga sites but as Mn interstitial defects. Magnetotransport and SQUID measurements reveal a Curie temperature of 20 K for pure WZ and mixed WZ/ZB NWs. The pure ZB NWs did not show a ferromagnetic phase transition as grown. After annealing, the Curie temperature was increased to 23 K for mixed WZ/ZB NWs and to 30 K for pure WZ NWs. The pure ZB NWs show a ferromagnetic phase transition at 60 K after annealing. The lower T_C compared to 2D GaMnAs layers grown on (110) oriented GaAs substrate is attributed to the high number of Mn interstitial defects in the GaMnAs shell, which work as donors and thereby reduce the hole concentration, which is essential for the formation of a ferromagnetic phase transition in GaMnAs [13]. Additionally, the crystal properties like the amount of stacking faults and the crystal phase may have an influence on T_C. Furthermore, a uniaxial magnetic anisotropy with a magnetic easy axis along the NW axis and a magnetic hard axis perpendicular to the NW axis was observed in SQUID and confirmed by magnetotransport measurement. The GaAs/GaMnAs core shell NWs show remanence for the magnetic easy axis between 80% and 65% and a coercive fields in the range of 50 mT to 75 mT (500 Oe to 750 Oe) for SQUID ensemble measurements (6 K) and of 140 mT to 220 mT for magnetotransport single NW measurements (4 K). The origin of the magnetic anisotropy is attributed to strain relaxation [48] of the GaMnAs shell in the direction perpendicular to the NW axis.

Chapter 8

Outlook

The dependence of the NW morphology on the growth parameters and the sample preparation techniques was studied in detail. Further investigations are required concerning the NW crystal structure.
Au catalyzed NWs with a pure ZB crystal phase reveal a region with a high density of stacking faults in the upper third of the NW and a short WZ segment below the catalyst droplet. It is assumed that this region is formed during the growth termination procedure, when the sample heating is switched off and the supply with Ga is stopped, but As is still present in the growth chamber. Despite the fact that the section with the irregular crystal structure is quite long with respect to the short growth termination procedure, which is in the order of 5 minutes, it is possible that the upper third of the NW is grown during this period. The reason is the temperature dependence of the NW growth rate (cf. chapter 2.1.2). To clarify this open question, further experiments with a different growth termination procedure are required.
The Au catalyzed NWs with a pure WZ crystal phase show a high density of stacking faults distributed over the whole NW length. This observation is attributed to the high As_4/Ga ratio of 8.8 which is used for the growth of pure WZ NWs. To improve the crystal quality and simultaneously conserve the pure WZ crystal structure, further experiments should be performed with lower As_4/Ga ratios. In particular, the parameter space between an As_4/Ga ratio of 8.8 (pure WZ crystal structure, but high density of SFs) and 3.6 (predominantly, but not exclusively WZ crystal structure, low density of SFs) should be investigated.

For the position controlled growth of GaAs NWs with the Au technique, the problem of catalyst droplet migration on the bare GaAs substrate has to be solved. It is suggested that the Au discs are deposited in very shallow holes, which are etched in the Si or GaAs substrates by wet chemical etching. With this sample setup, the standard parameters for Au catalyzed NW growth can be applied.
For the position controlled growth of GaAs NWs with the Ga technique, the value for the hole occupation number, which is approximately 30%, has to be increased. Therefore, different Si substrates and etching procedures, like reactive ion etch, should be investigated.

The growth of GaAs/GaMnAs core shell NWs still provides a lot of open questions. In this thesis, only the first samples with different crystal structures were grown to compare GaMnAs in its WZ and ZB crystal phase. However, the parameter space with respect to the Mn content and the As_4/Ga ratio is very large and could therefore not completely be investigated. The magnetic properties, especially the Curie temperature might strongly increase if different growth parameters, e.g. higher Mn contents above 5% and lower As_4/Ga ratios, close to unity, are applied. Also the growth of an AlGaAs shell between the GaAs core NW and the GaMnAs shell seems to be promising to increase T_C. Despite that, spin injection experiments could be performed with such a NW tunnel diode structure if the core NWs can be n+ doped (first experiments, not shown in this thesis, reveal that the doping of GaAs core NWs is possible).

Chapter 9

Acknowledgment

Here I like to thank all the people who supported me during my PhD time and/or contributed to this thesis. A special thank goes to my parents, Birgit and Klaus Rudolph for supporting me during the whole period of education and to my girlfriend Nikola, who gave me - by constantly moaning about her own PhD thesis - the feeling that everything is fine in my doctoral studies.

I further like to thank:

- Prof. Dr. Werner Wegscheider, for giving me the opportunity to do the PhD on his chair and for supervising my PhD thesis during the first 12 month.
- Prof. Dr. Dominique Bougeard, for supervising my PhD thesis during the last 18 month, revising my PhD script and improving my scientific writing skill.
- Dr. Elisabeth Reiger, for supervising my PhD thesis during the last 4 years, for the fruitful discussion, for the opportunity to visit a lot of conferences and for revising my PhD script.
- Dr. Dieter Schuh, for the maintenance of the MBE system.
- Martin Utz for introducing me into MBE growth.
- The "Schleusenfee" Imke Gronwald for safely transferring my samples into (and out of) the MBE system.
- Martin Furthmeier for his construction work on the annealing oven.
- Prof. Dr. Anna Fontcuberta i Morral and Prof. Dr. Tomasz Wojtowicz for showing me how to grow NWs with the Au catalyzed and the Ga catalyzed growth technique, respectively.

- Prof. Dr. Dieter Weiss for the access to the clean room.
- Matthias Kiessling for the SQUID measurements.
- Dr. Marcello Soda for the TEM investigations and for the fruitful discussions.
- Christian Butschkow for the magnetotransport measurements and for the fruitful discussions.
- Alexander Eckrot for the annealing experiments.
- Benedikt Bauer, Joachim Hubmann and Markus Kargl for the cooperation and fruitful discussion on the pre-structured NW growth topic.
- The whole chair of Prof. Wegscheider and Prof. Bougeard for the good cakes, Leberkäs and Weißwürst.

List of Publications

Publications in Journals

- A. Rudolph, M. Soda, M. Kiessling, T. Wojtowicz, D. Schuh, W. Wegscheider, J. Zweck, C. Back and E. Reiger: *Ferromagnetic GaAs/GaMnAs Core-Shell Nanowires Grown by Molecular Beam Epitaxy*, Nanoletters, **9**, 3860-3866 (2009)

- B. Bauer, A. Rudolph, M. Soda, A. Fontcuberta i Morral, J. Zweck, D. Schuh and E. Reiger: *Position controlled self-catalyzed growth of GaAs nanowires by molecular beam epitaxy*, Nanotechnology, **21**, 435601 (2010)

- M. Soda, A. Rudolph, D. Schuh, J. Zweck, D. Bougeard and E. Reiger: *Transition from Au to pseudo Ga-catalyzed growth mode observed in GaAs nanowires grown by MBE*, Physical Review B, **85**, 245450 (2012)

- C. H. Butschkow, E. Reiger, S. Geißler, A. Rudolph, M. Soda, D. Schuh, G. Woltersdorf, W. Wegscheider and D. Weiss: *Magnetoresistance of individual ferromagnetic GaAs/(Ga,Mn)As core-shell nanowires*, arXiv:1110.5507v1

- M. Heiss, S. Conesa-Boj, J. Ren, H. H. Tseng, A. Gali, A. Rudolph, E. Uccelli, F. Peiró, J. R. Morante, D. Schuh, E. Reiger, E. Kaxiras, J. Arbiol, and A. Fontcuberta i Morral: *Direct correlation of crystal structure and optical properties in wurtzite/zinc-blende GaAs nanowire heterostructures*, Physical Review B, **83**, 045303 (2011)

Talks and Posters

- *MBE growth of nanowires: Comparison of Gold catalyst and Gallium catalyst growth technique*,
  Poster, Nanowire Summerschool, Cortona, Italy, 06/2008
- *MBE growth of GaAs/GaMnAs core-shell nanowires*,
  Poster, DPG Spring Meeting, Dresden, Germany, 03/2009
- *MBE-Wachstum von ferromagnetischen Nanodrähten*,
  Poster, SFB Survey, Regensburg, Germany, 07/2009
- *GaAs/GaMnAs core-shell nanowires grown by MBE*,
  Poster, Nanowire Growth Workshop, Paris, France, 10/2009
- *Ferromagnetic core-shell GaAs/GaMnAs nanowires*,
  Talk, SFB Meeting, Kloster Niederalteich, Germany, 10/2009
- *GaAs/GaMnAs core-shell nanowires grown by MBE*,
  Talk, DPG Spring Meeting, Regensburg, Germany, 03/2010
- *Nanowire growth report 2010*,
  Talk, Zürich, Switzerland, 05/2010
- *Position-controlled Growth of Nanowires*,
  Talk, SFB Meeting, Kloster Niederalteich, Germany, 09/2010
- *Position controlled growth of GaAs nanowires by MBE*,
  Poster, Nanowire Growth workshop, Rom, Italy, 11/2010
- *Position controlled self-catalyzed growth of GaAs nanowires by MBE*,
  Poster, Euro MBE, L'Alpe d'Huez, France, 03/2011
- *Growth of GaAs nanowires and nanowire heterostructures*,
  Talk, Zürich, Switzerland, 11/2011
- *Properties of GaAs/GaMnAs core-shell nanowires grown by MBE*,
  Talk, MRS Fall Meeting, Boston, USA, 12/2011
- *Growth of GaAs nanowires and nanowire heterostructures*,
  Invited talk, Lausanne, Switzerland, 01/2012

Appendix A

The influence of surface preparation and As_2

A.1 Surface preparation

Here we discuss the influence of the oxide desorption procedure as well as the influence of the buffer layer growth and the HF etching procedure on the NW morphology. All three points are of technical nature and are therefore not discussed in the morphology chapter.

A.1.1 Influence of the oxide desorption procedure

The oxide desorption procedure is used to remove the natural oxide from the GaAs substrates. Oxide desorption starts at 575°C [59] and becomes more effective with increasing temperature. This raises the question whether a short oxide desorption procedure at high temperatures is more favorable with respect to a homogeneous NW morphology than a long procedure at lower temperatures.
At the beginning of the oxide desorption, the manipulator power is set to 0 W. The oxide desorption time is the time span between the moment where the manipulator power is set to the desorption value and the moment where the manipulator power is set to the growth value. It should be noted that the manipulator needs several minutes to reach the final oxide desorption temperature. For the optimization of the oxide desorption procedure five samples were grown using standard growth parameters and a substrate with an Au layer thickness of 5 Å. The applied temperatures and desorption times as well as the statistical evaluation of the NW samples are summarized in table A.1.
Sample C090507B is grown without oxide desorption. This experiment was done to

Sample number	C090507B	C090507A	C090428B	C090512A	C090428A
Oxide des. temp. [°C]	545	580	580	623	630
Oxide des. time [min.]	35	35	60	10	15
NW density [μm^{-2}]	-	12	11	15	12
Kinked NWs [norm.]	0.44	0.04	0.07	0.11	0.08
Small NWs [norm.]	0.15	0.33	0.31	0.25	0.32

Table A.1: Oxide desorption parameters and their influence on the NW morphology. The low ratio of small NWs in sample C090507B is attributed to the large number of kinked NWs. The case is reversed for sample C090512A.

investigate if oxide desorption is after all necessary for NW growth. To exclude the influence of the desorption time, the sample was kept at 545°C for 35 minutes before growth. Sample C090507A and C090428B are heated to 580°C for 35 minutes and 60 minutes, respectively. Referring to [59], 580°C is close to the minimum temperature needed for oxide desorption. The transition from an amorphous to a streaky RHEED pattern, which was observed after 35 minutes at 580°C, indicates that the oxide was completely removed. In sample C090428B the oxide desorption time was extended to 60 minutes to investigate if an increase in desorption time leads to an increase in NW homogeneity. Samples C090512A and C090428A were heated to 623°C and 630°C for 10 minutes and 15 minutes, respectively. At higher temperatures the oxide desorption is much faster than at the lower temperature of 580°C. Here, 10 minutes is the lower boundary for the oxide desorption procedure, as applied for sample C090512A.

The investigation of sample C090507B showed that oxide desorption is a crucial step to achieve samples with a homogeneous NW morphology. If the oxide desorption procedure is skipped, the NW growth is very inhomogeneous and a large amount of the NWs are kinked or twisted. If the oxide desorption procedure is performed, the NW growth is much more homogeneous and the amount of kinked NWs is strongly reduced (cf. figure A.1). The difference in the amount of kinked and small NWs between the different desorption procedures is very small. The NW density is almost constant independent of the chosen desorption temperature and time.

As the maximum accessible temperature is different for different sample holders, 580°C is chosen as standard desorption temperature because this temperature can be reached with any sample holder. As a consequence, the same oxide desorption procedure can be applied to all NW samples. The standard oxide desorption time was set to 35 minutes, which was the minimum value necessary for a complete oxide desorption.

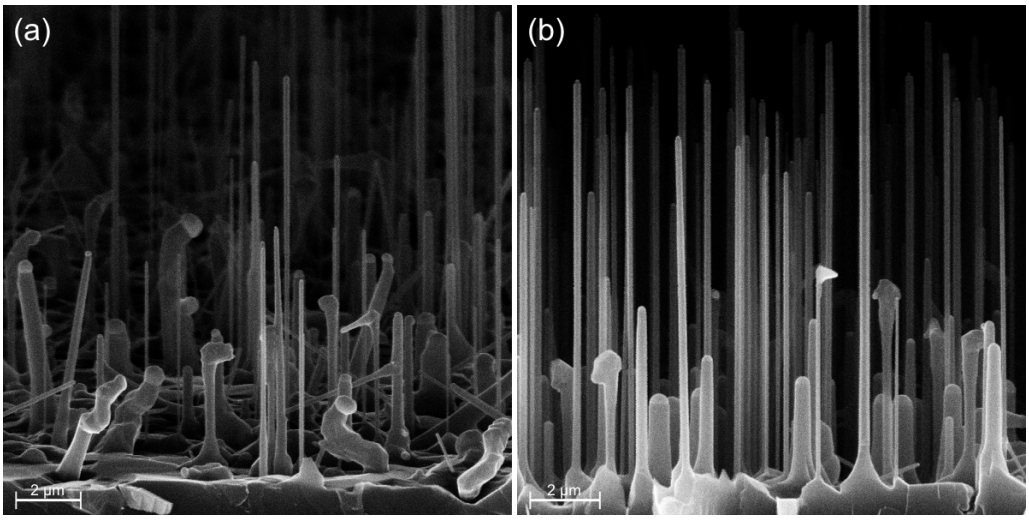

Figure A.1: SEM side view image of (a) sample C090507B and (b) sample C090507A. The only difference between the two samples is the thermal oxide desorption procedure, which was skipped for sample C090507B. As a result, the sample quality is strongly reduced.

A.1.2 Influence of the buffer layer and HF etching

Here, a 50 nm thick GaAs buffer layer is grown on (111)B oriented GaAs substrates with a Ga flux of 1 Å/s and an As_4 pressure of 3.6×10^{-6} Torr. The buffer layer flattens the GaAs substrate surface which is supposed to yield a more homogeneous catalyst droplet formation. Before the wafer is transferred to the metal MBE system, the liquid Ga from the back side of the substrate has to be removed with hydrochloric acid. To protect the buffer layer, the front side of the substrate was coated with wax. The wax was removed after the acid dip with chemical solvents. As the substrate is transferred to the metal MBE system in air after the buffer layer growth, a HF etching step (1.25% HF for 20 sec.) was applied to remove the newly built oxide before the Au film is deposited. Finally, a 10 Å Au film was deposited on the buffer layer in the metal MBE system. The thermal oxide desorption procedure in the semiconductor MBE, which should be dispensable if the oxide was removed by the HF etching step, was skipped for two samples. In order to investigate every step separately, a series of six samples was grown. Sample C090728B is used as reference sample as it has the same Au layer thickness and was grown with identical growth parameters. The results are summarized in table A.2.

The morphology of the NWs is independent of the surface treatment procedure before growth. The numbers for NW length and diameter are comparable to the corresponding numbers of sample C090728B. The only exception is the ratio of small NWs, which is nearly constant for all samples of this series but a factor of two

Sample number	C091215A		C091215B		C091216A		C090728B
Buffer layer and HF etching	-/-	-/HF	B/-	B/HF	-/HF	B/HF	ref
Thermal oxide desorption	yes	yes	yes	yes	no	no	yes
NW density [μm^{-2}]	18	21	20	16	9	13	16
Kinked NWs [norm.]	0.15	0.16	0.20	0.30	0.51	0.49	0.13
Small NWs [norm.]	0.19	0.20	0.15	0.19	-	-	0.38

Table A.2: NW properties with respect to the growth of a buffer layer and a HF etching step before Au deposition. Compared to the reference sample C090728B, the ratio of kinked NWs is increased if any kind of surface treatment is performed. As indicated by sample C091216A, the HF etching step is not suitable to permanently remove the native GaAs oxide layer.

higher for the reference sample. The ratio of small NWs could not be evaluated for the samples without thermal oxide desorption as the growth of whiskers was very pronounced. As a consequence, long and short NWs often coalesce and could not clearly be distinguished.

The difference in the ratio of small NWs between the reference sample and the samples of this series is attributed to the fact that the Au layer of the reference sample was deposited in the metal MBE system in Warsaw while the other Au layers were fabricated in the metal MBE system of Prof. Back in Regensburg. As a consequence, the properties of the Au layer, e.g. the Au layer homogeneity and thickness, could differ which leads to the formation of different catalyst droplet sizes. The quality of the NW samples is generally decreasing if a surface treatment procedure is applied before NW growth. The use of a HF etching step alone has no measurable influence on the sample quality as long as thermal oxide desorption is performed before NW growth. If a buffer layer is grown before Au deposition, the number of kinked NWs is slightly increased. The results get worse if both, a HF dip and the growth of a buffer layer are performed. The number of kinked NWs is doubled in this case compared with the sample without any surface treatment. The origin of this behavior is attributed to the cleaning procedure, which is used to remove the liquid Ga from the backside of the substrate after the buffer layer growth. Despite an exact use of the chemical cleaning recipe, some residues of the wax may have survived the chemical cleaning steps and stuck to the substrate surface.

To investigate if the HF etching step reliably removes the natural oxide of GaAs, two NW samples - one with and one without buffer layer - were grown without thermal oxide desorption. The amount of kinked NWs, which is strongly increased for both samples, is comparable to the corresponding number of sample C090507B. This sample, which was also grown without thermal oxide desorption was discussed

in chapter A.1.1. From these results we conclude that the HF etching step is not appropriate to permanently remove the natural GaAs oxide because the oxide reconstitution takes place within a few minutes [59], a time span which is to short to transfer the sample from the HF etching setup to the metal MBE system. As a consequence, the growth of a buffer layer and the HF dip were omitted for future samples.

A.1.3 Conclusion

The oxide desorption procedure was found to be crucial for NW growth as its omission leads to very inhomogeneous NW samples. The best desorption parameters with respect to sample reproducibility are 35 minutes desorption time at 580°C desorption temperature. The growth of a GaAs buffer layer did not improve the NW homogeneity because wax residues, which originate from the waver cleaning procedure, lead to a decrease in sample quality. Also the HF etching step before the Au layer deposition was found to be ineffective as the etched wafer immediately regains the natural oxide layer.

A.2 Influence of the As_2/Ga ratio

To investigate the influence of As_2 on the NW properties, a series of four samples with different As_2/Ga ratios of 0.8, 1.4, 1.8 and 2.2 at a fixed Ga rate of 0.8 Å/s was grown, similar to the series with different As_4 ratios (cf. chapter 4.1.4). For a fifth sample the Ga flux was increased to one monolayer/sec. and the As_2 pressure was adjusted such that the As_2/Ga ratio was 2.2. The amount of deposited Ga was doubled for this sample to 1200 nm. To obtain As_2 from the As_4 source the As cracker, which is placed on the opening of the As_4 cell was heated to 850°C. The sample substrate was changed during the sample series. The samples with an As_2/Ga ratio of 0.8 and 2.2 (600 nm GaAs deposition) were grown on a substrate covered by a 18 Å Au layer while the other samples were grown on a substrate covered by a 5 Å Au layer. Therefore, the NW densities of these samples cannot be compared. The results are summarized in table A.3.
The sample with an As_2/Ga ratio of 0.7 showed no NW growth and Ga puddles with a diameter of 1-2 μm were found all over the sample. The onset of NW growth was observed at an As_2/Ga ratio of 1.4 and 1.8. Again, Ga puddles are found on the sample surface but their number and size were decreasing. In addition, the growth of NW could be observed even if the NW density was very low. For an As_2/Ga ratio of 2.2 the NW density was strongly increased and the Ga puddles disappeared. The

Sample number	C090618A	C090630A	C090701A	C090622A	C090709A
Ga rate [Å/s]	0.75	0.77	0.80	0.78	2.75
As pressure [10^{-6} Torr]	0.21	0.36	0.49	0.58	2.06
As_2/Ga ratio	0.8	1.4	1.8	2.2	2.2
NW density [μm^{-2}]	-	<1	<1	26	34
NW length [μm]	-	0.6	0.4	0.7	1.6
Standard dev. [μm]	-	0.1	0.1	0.1	0.1
NW diameter [nm]	-	146	130	100	95
Standard dev. [nm]	-	18	37	55	15

Table A.3: NW properties with respect to the As_2/Ga ratio. For a suitable NW density the As_2/Ga ratios had to be raised to 2.2. The morphology of the NWs grown with As_2 differs significantly from the morphology of the NWs grown with As_4.

grown NWs were extremely homogeneous in length and show a pencil like shape (cf. figure A.2 (b)). The catalyst droplets are very small compared to the NW diameter. By increasing the amount of deposited Ga to 1200 nm and the Ga flux to one monolayer/sec. at an As_2/Ga ratio of 2.2 the NW length was doubled.

The results achieved with As_2 are very different from the results achieved with As_4. This is shown in figure A.2, where the sample C090316A (grown with As_4, 10 Å Au layer) is compared with sample C090622A (grown with As_2, 18 Å Au layer). For both samples an amount of 600 nm GaAs was deposited on the substrate with a Ga rate of 0.8 Å/s. The NW growth temperature was 537°C and 508°C, respectively. The As_x flux was adjusted such that the As_x/Ga ratio was 2.2 for both samples. The NW length is reduced from 3.1 μm to 0.7 μm and the NW diameter is increased from 75 nm to 100 nm for the sample grown with As_2. In addition, the NW shape is changed from cylindric (As_4) to pencil like (As_2). Despite the fact that a substrate with 18 Å Au, which gave the lowest NW density in chapter 4.1.1 was used for the growth with As_2, the NW density is increased from 10 NW/μm^2 for sample C090316A to 26 NW/μm^2 for sample C090622A.

The decrease in NW length could be explained with the decrease in total As_x pressure, which was 0.58×10^{-6} Torr for sample C090622A and 1.33×10^{-6} Torr for sample C090316A. However, the reduced total As_x pressure could not explain the increased NW diameter and the pencil like shape of the NWs grown with As_2. A comprehensive explanation can only be given if a dependence of the Ga diffusion length on the As species is taken into account. Unfortunately, no data is available for the Ga diffusion length under As_2 for the predominant crystal orientations of the NW side facets, which are (1120)/(110) for the WZ/ZB crystal phase, respectively.

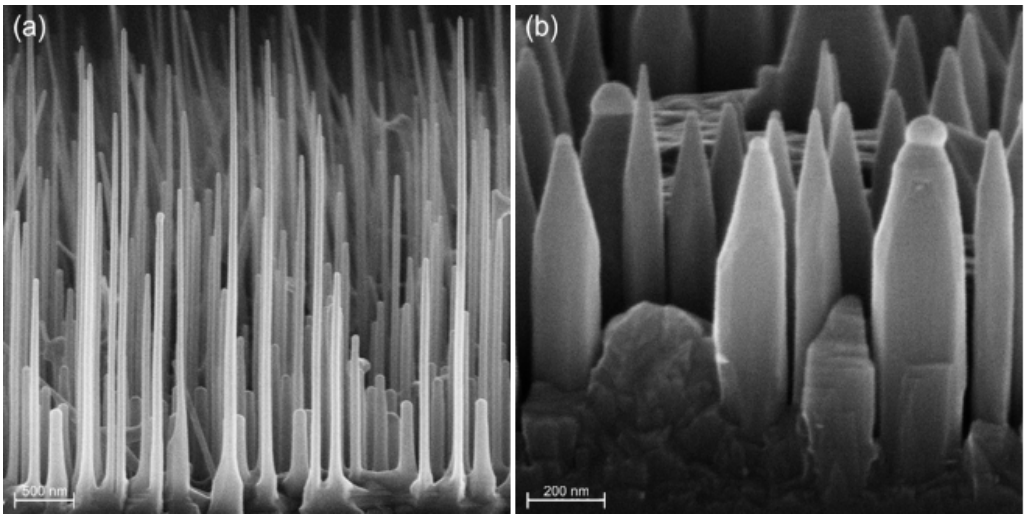

Figure A.2: SEM side view image of (a) sample C090316A (grown with As_4) and (b) sample C090622A (grown with As_2). Despite the fact that both samples were grown with identical As_x/Ga ratios, the NW morphology of the two samples differs significantly from each other.

However, for the (001) crystal orientation the Ga diffusion length is found to be smaller under As_2 than under As_4 [103]. If such a behavior is also assumed for the (1120)/(110) crystal orientations, the reduced NW length could be attributed to Ga nucleation on the NW side facets. As a consequence, the NW diameter would increase due to radial NW growth, which is in accordance with our observations. If the NW length significantly exceeds the Ga diffusion length, the nucleation would preferentially occur at the lower part of the NW. In addition, the catalyst droplet and thereby the NW diameter would constantly decrease if the Ga supply of the catalyst droplet is diminished. Both effects would lead to the observed pencil shape of the NWs. This explanation is supported by a publication from 2010, which investigated the influence of the As species on the NW morphology in detail [91]. Due to the fact that the growth parameters in this publication differ significantly from our growth parameters, also the NW morphologies are not identical. However, the conclusions drawn in the publication are similar to the conclusion drawn above. Referring to [91], which predicts a temperature dependent NW density, the increase in NW density of the sample grown with As_2 can now be explained with the slightly lower NW growth temperature of this sample with respect to the sample grown with As_4.

Bibliography

[1] J. R. Arthur, *Interaction of Ga and As_2 molecular beams with GaAs surfaces*, Journal of Applied Physics **39** (1968), 4032–4034.

[2] N. W. Ashcroft and N. D. Mermin, *Festkörperphysik*, Oldenbourg Verlag, 2001.

[3] B. Bauer, *Positionskontrolliertes Wachstum von GaAs-Nanodrähten durch Vorstrukturierung der Substrate mittels Elektronenstrahllithographie*, Master's thesis, Universität Regensburg, 2010.

[4] B. Bauer, A. Rudolph, M. Soda, A. Fontcuberta i Morral, J. Zweck, D. Schuh, and E. Reiger, *Position controlled self-catalyzed growth of GaAs nanowires by molecular beam epitaxy*, Nanotechnology **21** (2010), 435601.

[5] C. Bihler, M. Althammer, A. Brandlmaier, S. Geprägs, M. Weiler, M. Opel, W. Schoch, W. Limmer, R. Gross, M. S. Brandt, and S. T. B. Goennenwein, *$Ga_{1-x}Mn_xAs$/piezoelectric actuator hybrids: A model system for magnetoelastic magnetization manipulation*, Physical Review B **78** (2008), 045203.

[6] M. T. Björk, J. Knoch, H. Schmid, H. Riel, and W. Riess, *Silicon nanowire tunneling field-effect transistors*, Applied Physics Letters **92** (2008), 193504.

[7] T. Bryllert, L. B. Wernersson, T. Löwgren, and L. Samuelson, *Vertical wrap-gated nanowire transistors*, Nanotechnology **17** (2006), 227–230.

[8] C. H. Butschkow, E. Reiger, S. Geißler, A. Rudolph, M. Soda, D. Schuh, G. Woltersdorf, W. Wegscheider, and D. Weiss, *Magnetoresistance of individual ferromagnetic GaAs/(Ga,Mn)As core-shell nanowires*, arXiv:1110.5507v1 (2012).

[9] C. Chatillon, F. Hodaj, and A. Pisch, *Thermodynamics of GaAs nanowire MBE growth with gold droplets*, Journal of Chrystal Growth **311** (2009), 3598–3608.

[10] C. Colombo, D. Spirkoska, M. Frimmer, G. Abstreiter, and A. Fontcuberta i Morral, *Ga-assisted catalyst-free growth mechanism of GaAs nanowires by molecular beam epitaxy*, Physical Review B **77** (2008), 155326.

[11] S. Datta and B. Das, *Electronic analog of the electro-optic modulator*, Applied Physics Letters **56** (1990), 665–667.

[12] T. Dietl, H. Ohno, and F. Matsukura, *Hole-mediated ferromagnetism in tetrahedrally coordinated semiconductors*, Physical Review B **63** (2001), 195205.

[13] T. Dietl, H. Ohno, F. Matsukura, J. Cibert, and D. Ferrand, *Zener Model Description of Ferromagnetism in Zinc-Blende Magnetic Semiconductors*, Science **287** (2000), 1019–1022.

[14] M. Döppe, *Magnetotransport- und Anisotropieuntersuchungen an (001) und (311)A (Ga,Mn)As*, Ph.D. thesis, Universität Regensburg, 2007.

[15] V. G. Dubrovskii and G. E. Cirlin, *Growth kinetics of thin films formed by nucleation during layer formation*, Semiconductors **39** (2005), 1267–1274.

[16] V. G. Dubrovskii, G. E. Cirlin, I. P. Soshnikov, A. A. Tonkikh, N. V. Sibirev, Y. B. Samsonenko, and V. M. Ustinov, *Diffusion-induced growth of GaAs nanowhiskers during molecular beam epitaxy: Theory and experiment*, Physical Review B **71** (2005), 205325.

[17] V. G. Dubrovskii and N. V. Sibirev, *Growth rate of a crystal facet of arbitrary size and growth kinetics of vertical nanowires*, Physical Review E **70** (2004), 031604.

[18] V. G. Dubrovskii and N. V. Sibirev, *General form of the dependences of nanowire growth rate on the nanowire radius*, Journal of Crystal Growth **304** (2007), 504–513.

[19] V. G. Dubrovskii and N. V. Sibirev, *Growth thermodynamics of nanowires and its application to polytypism of zinc blende III-V nanowires*, Physical Review B **77** (2008), 035414.

[20] V. G. Dubrovskii, N. V. Sibirev, G. E. Cirlin, A. D. Bouravleuv, Y. B. Samsonenko, D. L. Dheeraj, H. L. Zhou, C. Sarte, J. C. Harmand, G. Patriarche, and F. Glas, *Role of nonlinear effects in nanowire growth and crystal phase*, Physical Review B **80** (2009), 205305.

[21] V. G. Dubrovskii, N. V. Sibirev, G. E. Cirlin, J. C. Harmand, and V. M. Ustinov, *Theoretical analysis of the vapor-liquid-solid mechanism of nanowire growth during molecular beam epitaxy*, Physical Review E **73** (2006), 021603.

[22] V. G. Dubrovskii, N. V. Sibirev, G. E. Cirlin, I. P. Soshnikov, W. H. Chen, R. Larde, E. Cade, P. Pareige, T. Xu, B. Grandidier, J.-P. Nys, D. Stievenard, M. Moewe, L. C. Chuang, and C. Chang-Hasnain, *Gibbs-Thomson and diffusion-induced contributions to the growth rate of Si, InP, and GaAs nanowires*, Physical Review B **79** (2009), 205316.

[23] V. G. Dubrovskii, N. V. Sibirev, J. C. Harmand, and F. Glas, *Growth kinetics and crystal structure of semiconductor nanowires*, Physical Review B **78** (2008), 235301.

[24] V. G. Dubrovskii, N. V. Sibirev, R. A. Suris, G. E. Cirlin, J. C. Harmand, and V. M. Ustinov, *Diffusion-controlled growth of semiconductor nanowires: Vapor pressure versus high vacuum deposition*, Surface Science **601** (2007), 4395–4401.

[25] V. G. Dubrovskii, N. V. Sibirev, X. Zhang, and R. A. Suris, *Stress-Driven Nucleation of Three-Dimensional Crystal Islands: From Quantum Dots to Nanoneedles*, Crystal Growth & Design **10** (2010), 3949–3955.

[26] V. G. Dubrovskii, I. P. Soshnikov, G. E. Cirlin, A. A. Tonkikh, Y. B. Samsonenko, N. V. Sibirev, and V. M. Ustinov, *On the non-monotonic lateral size dependence of the height of GaAs nanowhiskers grown by molecular beam epitaxy at high temperature*, Physica Stutus Solidi **241** (2004), 30–33.

[27] A. Eckrot, *Annealing Experiment an GaAs/GaMnAs core-shell Nanodrähten*, Master's thesis, Universität Regensburg, 2012.

[28] R. P. Elliott and F. A. Shunk, *The Au-Si (Gold-Silicon) system*, Journal of Phase Equilibria **4** (1983), 356–358.

[29] R. Engel-Herbert, *MBE instrument showing growth of functional oxide thin films*, website, 2011, http://www.mri.psu.edu/publications/focus_on materials/spring-2011/complex_oxides/hybrid_molecular_beam_epitaxy.jpg.

[30] H. Ohno et al., *Semiconductor Spintronics and Quantum Computation*, Springer, 2002.

[31] J. Fabian, A. Matos-Abiague, C. Ertler, P. Stano, and I. Žutić, *Semiconductor Spintronics*, Acta Physica Slovaca **57** (2007), 1–343.

[32] C. T. Foxon and B. A. Joyce, *Interaction kinetics of As_4 and Ga on {100} GaAs surfaces using a modulated molecular beam technique*, Surface Science **50** (1975), 434–450.

[33] C. T. Foxon and B. A. Joyce, *Interaction kinetics of As_2 and Ga on {100} GaAs surfaces*, Surface Science **64** (1977), 293–304.

[34] L. E. Fröberg, W. Seifert, and J. Johansson, *Diameter-dependent growth rate of InAs nanowires*, Physical Review B **76** (2007), 153401.

[35] E. I. Givargizov and A. A. Chernov, *Growth-rate of whiskers grown by vapor-liquid-solid mechanism and role of surface-energy*, Kristallografiya **18** (1973), 147–153.

[36] F. Glas, *Chemical potentials for Au-assisted vapor-liquid-solid growth of III-V nanowires*, Journal of Applied Physics **108** (2010), 073506.

[37] F. Glas, J. C. Harmand, and G. Patriarche, *Why Does Wurtzite Form in Nanowires of III-V Zinc Blende Semiconductors?*, Physical Review Letters **99** (2007), 146101.

[38] F. Glas, J. C. Harmand, and G. Patriarche, *Nucleation Antibunching in Catalyst-Assisted Nanowire Growth*, Physical Review Letters **104** (2010), 135501.

[39] J. Goldstein, D. Newbury, D. Joy, C. Lyman, P. Echlin, E. Lifshin, L. Sawyer, and J. Michael, *Scanning Electron Microscopy and X-Ray Microanalysis*, Kluwer Academic und Plenum, 2003.

[40] J. Y. Guo, Y. W. Zhang, and V. B. Shenoy, *Morphological Evolution and Ordered Quantum Structure Formation in Heteroepitaxial Core-Shell Nanowires*, ACS Nano **4** (2010), 4455–4462.

[41] J. C. Harmand, G. Patriarche, N. Péré-Laperne, M-N. Mérat-Combes, L. Travers, and F. Glas, *Analysis of vapor-liquid-solid mechanism in Au-assisted GaAs nanowire growth*, Applied Physics Letters **87** (2005), 203101.

[42] J. C. Harmand, M. Tchernycheva, G. Patriarche, L. Travers, F. Glas, and G. Cirlin, *GaAs nanowires formed by Au-assisted molecular beam epitaxy: Effect of growth temperature*, Journal of Crystal Growth **301** (2007), 853–856.

[43] T. Hayakawa, M. Morishima, and S. Chen, *Surface reconstruction limited mechanism of molecular beam epitaxial growth of AlGaAs on (111)B face*, Applied Physics Letters **59** (1991), 3321.

[44] M. Heiß, E. Riedlberger, D. Spirkoska, M. Bichler, G. Abstreiter, and A. Fontcuberta i Morral, *Growth mechanisms and optical properties of GaAs-based semiconductor microstructures by selective area epitaxy*, Journal of Crystal Growth **310** (2008), 1049–1056.

[45] K. Hiruma, M. Yazawa, K. Haraguchi, K. Ogawa, T. Katsuyama, M. Koguchi, and H. Kakibayashi, *GaAs freestanding quantum-size wires*, Journal of Applied Physics **74** (1993), 3162–3171.

[46] J. Hubmann, *GaAs-Nanodrähte: Vorstrukturierung der Substrate und Charakterisierung des Wachstums*, Master's thesis, Universität Regensburg, 2011.

[47] J. Hübner, W. W. Rühle, M. Klude, D. Hommel, R. D. R. Bhat, J. E. Sipe, and H. M. van Driel, *Direct observation of optically injected spin-polarized currents in semiconductors*, Physical Review Letters **90** (2003), 216601.

[48] S. Hümpfner, K. Pappert, J. Wenisch, K. Brunner, C. Gould, G. Schmidt, L. W. Molenkamp, M. Sawicki, and T. Dietl, *Lithographic engineering of anisotropies in (Ga,Mn)As*, Applied Physics Letters **90** (2007), 102102.

[49] A. Fontcuberta i Morral, C. Colombo, G. Abstreiter, J. Arbiol, and J. R. Morante, *Nucleation mechanism of gallium-assisted molecular beam epitaxy growth of gallium arsenide nanowires*, Applied Physics Letters **92** (2008), 063112.

[50] A. Fontcuberta i Morral, D. Spirkoska, J. Arbiol, M. Heigoldt, J. R. Morante, and G. Abstreiter, *Prismatic Quantum Heterostructures Synthesized on Molecular-Beam Epitaxy GaAs Nanowires*, Small **4** (2008), 899–903.

[51] H. C. Jeon, T. W. Kang, T. W. Kim, Y.-J. Yu, W. Jhe, and S. A. Song, *Magnetic and optical properties of $(Ga_{1-x}Mn_x)As$ diluted magnetic semiconductor quantum wires with above room ferromagnetic transition temperature*, Journal of Applied Physics **101** (2007), 023508.

[52] T. B. Joyce and T. J. Bullough, *Beam equivalent pressure measurements in chemical beam epitaxy*, Journal of Crystal Growth **127** (1993), 265–269.

[53] M. Kargl, *Positionskontrolliertes Wachstum von GaAs-Nanodrähten und deren Charakterisierung mit Hilfe von Mikro-Photolumineszenz*, Master's thesis, Universität Regensburg, 2011.

[54] T. Kasuya and A. Yanase, *Anomalous Transport Phenomena in Eu-Chalcogenide Alloys*, Review of Modern Physics **40** (1968), 684–696.

[55] H. S. Kim, Y. J. Cho, K. J. Kong, C. H. Kim, G. B. Chung, J. Park, J. Y. Kim, J. Yoon, M. H. Jung, Y. Jo, B. Kim, and J. P. Ahn, *Room-Temperature Ferromagnetic $Ga_{1-x}Mn_xAs(x \leq 0.05)$ Nanowires: Dependence of Electronic Structures and Magnetic Properties on Mn Content*, Chemistry of Materials **21** (2009), 1137–1143.

[56] L. W. Kirenski, *Magnetismus*, Teubner Verlagsgesellschaft, 1969.

[57] S. A. Kukushkin and A. V. Osipov, *New phase formation on solid surfaces and thin film condensation*, Progress in Surface Science **51** (1996), 1–107.

[58] L. D. Landau and E. M. Lifshits, *Statistical Physics*, Butterworth, 1980.

[59] Landolt-Börnstein, *Group IV Elements, IV-IV and III-V Compounds*, Springer, 2006.

[60] S. C. Lee and S. R. J. Brueck, *Scaling of the surface migration length in nanoscale patterned growth*, Applied Physics Letters **94** (2009), 153110.

[61] K. Ma, R. Urata, D. A. B. Miller, and J. S. Harris, *Low-temperature growth of GaAs on Si used for ultrafast photoconductive switches*, Journal of Quantum Electronics **40** (2004), 800–804.

[62] S. O. Mariager, C. B. Sørensen, M. Aagesen, J. Nygård, and R. Feidenhans'l, *Facet structure of GaAs nanowires grown by molecular beam epitaxy*, Applied Physics Letters **91** (2007), 083106.

[63] F. Martelli, M. Piccin, G. Bais, F. Jabeen, S. Ambrosini, S. Rubini, and A. Franciosi, *Photoluminescence of Mn-catalyzed GaAs nanowires grown by molecular beam epitaxy*, Nanotechnology **18** (2007), 125604.

[64] F. Matsukura, M. Sawicki, T. Dietl, D. Chiba, and H. Ohno, *Magnetotransport properties of metallic (Ga,Mn)As films with compressive and tensile strain*, Physica E **21** (2004), 1032–1036.

[65] A. Mauger and C. Godart, *The magnetic, optical, and transport properties of representatives of a class of magnetic semiconductors: The europium chalcogenides*, Physical Reports **141** (1986), 51–176.

[66] E. D. Minot, F. Kelkensberg, M. van Kouwen, J. A. van Dam, L. P. Kouwenhoven, V. Zwiller, M. T. Borgström, O. Wunnicke, M. A. Verheijen, and E. P. A. M. Bakkers, *Single Quantum Dot Nanowire LEDs*, Nanoletters **7** (2007), 367–371.

[67] G. E. Moore, *Cramming more components onto integrated circuits*, Electronics **38** (1965), 114–117.

[68] Y. Morishita, Y. Nomura, S. Goto, and Y. Katayama, *Effect of hydrogen on the surface diffusion length of Ga adatoms during molecular beam epitaxy*, Applied Physics Letters **67** (1995), 2500–2502.

[69] W. Nolting, *Quantentherorie des Magnetismus*, Teubner Studienbücher, 1986.

[70] This is possible, because Si substrates were used. For GaAs substrates, As pressure would be necessary to prevent the decomposition of the substrates.

[71] Personal correspondence with Prof. Dr. Fontcuberta i Morral.

[72] This results from the fact that As is collected by the droplet surface while the As concentration is related to the droplet volume.

[73] V. Novák, K. Olejník, J. Wunderlich, M. Cukr, K. Výborný, A. Rushforth, K. Edmonds, R. Campion, B. Gallagher, J. Sinova, and T. Jungwirth, *Curie Point Singularity in the Temperature Derivative of Resistivity in (Ga,Mn)As*, Physical Review Letters **101** (2008), 077201.

[74] B. J. Ohlsson, M. T. Björk, M. H. Magnusson, K. Deppert, and L. Samuelson, *Size-, shape-, and position-controlled GaAs nano-whiskers*, Applied Physics Letters **79** (2001), 3335–3337.

[75] H. Ohno, *Making Nonmagnetic Semiconductors Ferromagnetic*, Science **281** (1998), 951–956.

[76] H. Ohno, N. Akiba, F. Matsukura, A. Shen, K. Ohtani, and Y. Ohno, *Spontaneous splitting of ferromagnetic (Ga, Mn)As valence band observed by resonant tunneling spectroscopy*, Applied Physics Letters **73** (1998), 363–365.

[77] H. Ohno, A. Shen, F. Matsukura, A. Oiwa, A. Endo, S. Katsumoto, and Y. Iye, *(Ga,Mn)As: A new diluted magnetic semiconductor based on GaAs*, Applied Physics Letters **69** (1996), 363–365.

[78] H. Okamoto and T. B. Massalski, *The Au-Si (Gold-Silicon) System*, Journal of Phase Equilibria **4** (1983), 190–198.

[79] V. V. Osipov, N. A. Viglin, and A. A. Samokhvalov, *Investigation of heterostructure "ferromagnetic semiconductor-semiconductor" in the millimeter and submillimeter microwave range*, Physics Letters A **247** (1998), 353–359.

[80] W. Ostwald, *Über die vermeintliche Isomerie des roten und gelben Quecksilberoxyds und die Oberflächenspannung fester Körper*, Zeitschrift für Physikalische Chemie **34** (1900), 495–503.

[81] A. I. Persson, L. E. Fröberg, S. Jeppesen, M. T. Björk, and L. Samuelson, *Surface diffusion effects on growth of nanowires by chemical beam epitaxy*, Journal of Applied Physics **101** (2007), 034313.

[82] A. I. Persson, M. W. Larsson, S. Stenström, B. J. Ohlsson, L. Samuelson, and L. R. Wallenberg, *Solid-phase diffusion mechanism for GaAs nanowire growth*, Nature Materials **3** (2004), 677–681.

[83] M. C. Plante and R. R. LaPierre, *Growth mechanisms of GaAs nanowires by gas source molecular beam epitaxy*, Journal of Crystal Growth **286** (2006), 394–399.

[84] M. C. Plante and R. R. LaPierre, *Control of GaAs nanowire morphology and crystal structure*, Nanotechnology **19** (2008), 495603.

[85] S. Plissard, G. Larrieu, X. Wallart, and P. Caroff, *High yield of self-catalyzed GaAs nanowire arrays grown on silicon via gallium droplet positioning*, Nanotechnology **22** (2011), 275602.

[86] M. R. Ramdani, J. C. Harmand, F. Glas, G. Patriarche, and L. Travers, *Growth of self-catalyzed GaAs nanowires: what are the As pathways?*, 6th Nanowire Growth Workshop, 2012.

[87] M. Reinwald, U. Wurstbauer, M. Döppe, W. Kipferl, K. Wagenhuber, H.-P. Tranitz, D. Weiss, and W. Wegscheider, *Growth of (Ga,Mn)As on GaAs (001) and (311)A in a high-mobility MBE system*, Journal of Crystal Growth **278** (2005), 690–694.

[88] A. Rudolph, M. Soda, M. Kiessling, T. Wojtowicz, D. Schuh, W. Wegscheider, J. Zweck, C. Back, and E. Reiger, *Ferromagnetic GaAs/GaMnAs Core-Shell Nanowires Grown by Molecular Beam Epitaxy*, Nanoletters **9** (2009), 3860–3866.

[89] J. Sadowski, *GaMnAs: Layers, Wires and Dots*, Acta Physica Polonica A **114** (2008), 1001–1012.

[90] J. Sadowski, P. Dłużewski, S. Kret, E. Janik, E. Łusakowska, J. Kanski, A. Presz, F. Terki, S. Charar, and D. Tang, *GaAs:Mn Nanowires Grown by Molecular Beam Epitaxy of (Ga,Mn)As at MnAs Segregation Conditions*, Nanoletters **7** (2007), 2724–2728.

[91] C. Sartel, D. L. Dheeraj, F. Jabeen, and J. C. Harmand, *Effect of arsenic species on the kinetics of GaAs nanowires growth by molecular beam epitaxy*, Journal of Crystal Growth **312** (2010), 2073–2077.

[92] G. Schmidt, D. Ferrand, L. W. Molenkamp, A. T. Filip, and B. J. van Wees, *Fundamental obstacle for electrical spin injection from a ferromagnetic metal into a diffusive semiconductor*, Physical Review B **62** (2000), 4790–4793.

[93] M. J. Seong, S. H. Chun, H. M. Cheong, N. Samarth, and A. Mascarenhas, *Spectroscopic determination of hole density in the ferromagnetic semiconductor* $Ga_{1-x}Mn_xAs$, Physical Review B **66** (2002), 033202.

[94] P. W. Shor, *Polynomial-Time Algorithms for Prime Factorization and Discrete Logarithms on a Quantum Computer*, SIAM Review **41** (1999), 303–332.

[95] N. V. Sibirev, M. B. Nazarenko, G. E. Cirlin, Y. B. Samsonenko, and V. G. Dubrovskii, *The initial stage of growth of crystalline nanowhiskers*, Semiconductors **44** (2010), 112–115.

[96] N. V. Sibirev, M. A. Timofeeva, A. D. Bol'shakov, M. V. Nazarenko, and V. G. Dubrovskii, *Surface Energy and Crystal Structure of Nanowhiskers of III-V Semiconductor Compounds*, Physics of Solid State **52** (2010), 1531–1538.

[97] M. Soda, *Structural and Morphological TEM Characterization of GaAs based Nanowires*, Ph.D. thesis, Universität Regensburg, 2012.

[98] M. Soda, A. Rudolph, D. Schuh, J. Zweck, D. Bougeard, and E. Reiger, *Transition from Au to pseudo Ga-catalyzed growth mode observed in GaAs nanowires grown by MBE*, Physical Review B **85** (2012), 245450.

[99] I. P. Soshnikov, G. É. Cirlin, A. A. Tonkikh, V. N. Nevedomski, Y. B. Samsonenko, and V. M. Ustinov, *Electron Diffraction on GaAs Nanowhiskers Grown on Si(100) and Si(111) Substrates by Molecular-Beam Epitaxy*, Semiconductors and Dielectrics **49** (2007), 1440–1445.

[100] D. Spirkoska, J. Arbiol, A. Gustafsson, S. Conesa-Boj, F. Glas, I. Zardo, M. Heigoldt, M. H. Gass, A. L. Bleloch, S. Estrade, M. Kaniber, J. Rossler, F. Peiro, J. R. Morante, G. Abstreiter, L. Samuelson, and A. Fontcuberta i Morral, *Structural and optical properties of high quality zinc-blende/wurtzite GaAs nanowire heterostructures*, Physical Review B **80** (2009), 245325.

[101] M. J. Stevens, A. L. Smirl, R. D. R. Bhat, A. Najmaie, J. E. Sipe, and H. M. van Driel, *Quantum Interference Control of Ballistic Pure Spin Currents in Semiconductors*, Physical Review Letters **90** (2003), 136603.

[102] J. Stolze and D. Suter, *Quantum computing*, Wiley-VCH, 2004.

[103] T. Sugaya, T. Nakagawa, Y. Sugiyama, Y. Tanuma, and K. Yonei, *Difference in Diffusion Length of Ga Atoms under As_2 and As_4 Flux in Molecular Beam Epitaxy*, Japanese Journal of Applied Physics **36** (1997), 5670–5673.

[104] M. Tchernycheva, J. C. Harmand, G. Patriarche, L. Travers, and G. E. Cirlin, *Temperature conditions for GaAs nanowire formation by Au-assisted molecular beam epitaxy*, Nanotechnology **17** (2006), 4025–4030.

[105] M. Tchernycheva, L. Travers, G. Patriarche, F. Glas, J. C. Harmand, G. C. Cirlin, and V. G. Dubrovskii, *Au-assisted molecular beam epitaxy of InAs nanowires: Growth and theoretical analysis*, Journal of Applied Physics **102** (2007), 094313.

[106] C. Thelander, T. Mårtensson, M. T. Björk, B. J. Ohlsson, M. W. Larsson, L. R. Wallenberg, and L. Samuelson, *Single-electron transistors in heterostructure nanowires*, Applied Physics Letters **83** (2003), 2052–2054.

[107] J. Y. Tsao, *Materials fundamentals of melecular beam epitaxy*, Academic Press Inc., 1993.

[108] I. Žutić, J. Fabian, and S. D. Sarma, *Spintronics: Fundamentals and applications*, Review of Modern Physics **76** (2004), 323–410.

[109] L. M. K. Vandersypen, M. Steffen, G. Breyta, C. S. Yannoni, M. H. Sherwood, and I. L. Chuang, *Experimental realization of Shor's quantum factoring algorithm using nuclear magnetic resonance*, Nature **414** (2001), 883–887.

[110] N. A. Viglin, V. V. Osipov, A. A. Samokhvalov, and O. G. Reznitskikh, *Generation in the millimeter band for the semiconductor ferromagnetic semiconductor heterostructure*, Physics of Low Dimensional Structures **1-2** (1997), 89–94.

[111] J. B. Wagner, N. Sköld, L. R. Wallenberg, and L. Samuelson, *Growth and segregation of GaAs-$Al_xIn_{1-x}P$ core-shell nanowires*, Journal of Crystal Growth **312** (2010), 1755–1760.

[112] H. Wang, M. Upmanyu, and C. V. Ciobanu, *Morphology of Epitaxial Core-Shell Nanowires*, Nanoletters **8** (2008), 4305–4311.

[113] K. Y. Wang, K. W. Edmonds, R. P. Campion, B. L. Gallagher, N. R. S. Farley, C. T. Foxon, M. Sawicki, P. Boguslawski, and T. Dietl, *Influence of the Mn interstitial on the magnetic and transport properties of (Ga,Mn)As*, Journal of Applied Physics **95** (2004), 6512–6514.

[114] W. Wegscheider and D. Weiss, *Vorlesungsskript Halbleiterphysik*, 2006.

[115] J. Wenisch, C. Gould, L. Ebel, J. Storz, K. Pappert, M. J. Schmidt, C. Kumpf, G. Schmidt, K. Brunner, and L. W. Molenkamp, *Control of Magnetic Anisotropy in (Ga,Mn)As by Lithography-Induced Strain Relaxation*, Physical Review Letters **99** (2007), 077201.

[116] Wgsimon, *Microprocessor Transistor Counts 1971-2011 and Moore's Law*, website, 2011, http://de.wikipedia.org/wiki/Mooresches_Gesetz.

[117] D. B. Williams and C. B. Carter, *Transmission Electron Microscopy*, Springer Science and Business Media, 2009.

[118] U. Wurstbauer, M. Sperl, D. Schuh, G. Bayreuther, J. Sadowski, and W. Wegscheider, *GaMnAs grown on (001), (311)A and (110) GaAs substrates: Comparison of growth conditions and post-growth annealing behaviour*, Journal of Crystal Growth **301** (2007), 260–263.

[119] U. Wurstbauer, M. Sperl, M. Soda, D. Neumaier, D. Schuh, G. Bayreuther, J. Zweck, and W. Wegscheider, *Ferromagnetic GaMnAs grown on (110) faced GaAs*, Applied Physics Letters **92** (2008), 102506.

[120] C.-Y. Yeh, Z. W. Lu, S. Froyen, and A. Zunger, *Zinc blende-wurtzite polytypism in semiconductors*, Physical Review B **46** (1992), 10086–10097.

[121] A. Zangwill, *Physics at Surfaces*, Cambridge University Press, 1988.

[122] C. A. Zorman and M. Mehregany, *Material Aspects of Micro- and Nanoelectromechanical Systems*, Springer, 2007.